AD-A072 529 PRATT AND WHITNEY AIRCRAFT GROUP WEST PALM BEACH FL G--ETC F/G 11/6
TITANIUM CMBUSTION RESEARCH PROGRAM AND USER'S MANUAL FOR DECK --ETC(U)
MAR 79 M R GLICKSTEIN F33615-76-C-5041
UNCLASSIFIED PWA-FR-10748 AFML -TR-79-4001 NL

1 OF 2
ADA 072529

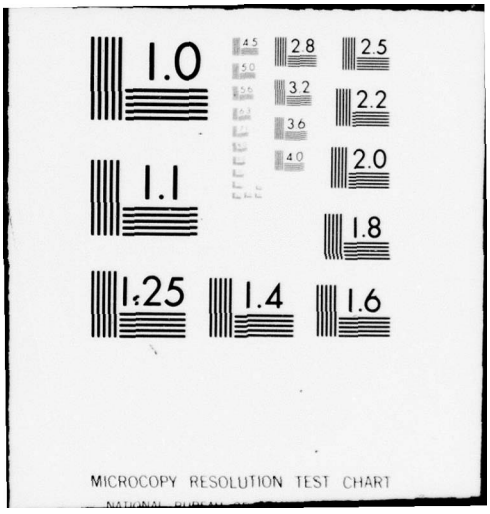
1.0
1.1
1.25
1.4
1.6
1.8
2.0
2.2
2.5
2.8
3.2
3.6
4.0
4.5
5.0
5.6
MICROCOPY RESOLUTION TEST CHART

AD A072529 LEVEL II

AFML TR-79-4001

Final Report Titanium Combustion Research Program and User's Manual for Deck CCD 1152-0.0

Pratt & Whitney Aircraft Group
Government Products Division
P. O. Box 2691
West Palm Beach, Florida 33402

March 1979

DDC AUG 9 1979

TECHNICAL REPORT AND USER'S MANUAL AFML-TR-79-4001

DDC FILE COPY

FINAL REPORT AND USER'S MANUAL FOR PERIOD DEC 1975 TO SEPT 1978

Approved for public release; distribution unlimited.

Air Force Materials Laboratory
Air Force Wright Aeronautical Laboratories
Air Force Systems Command
Wright-Patterson Air Force Base, Ohio 45433

79 08 8 077

NOTICE

When Government drawings, specifications, or other data are used for any purpose other than in connection with a definitely related Government procurement operation, the United States Government thereby incurs no responsibility nor any obligation whatsoever; and the fact that the government may have formulated, furnished, or in any way supplied the said drawings, specifications, or other data, is not to be regarded by implication or otherwise as in any manner licensing the holder or any other person or corporation, or conveying any rights or permission to manufacture, use, or sell any patented invention that may in any way be related thereto.

This technical report has been reviewed and is approved for publication.

Stephen R Lyon

STEPHEN R. LYON
Project Engineer

Gary L Denman

GARY L. DENMAN
Program Manager
Laser Hardened Materials Branch

FOR THE COMMANDER:

R E Brocklehurst

ROBERT E. BROCKLEHURST, Chief
Electromagnetic Materials Division
Air Force Materials Laboratory

"If your address has changed, if you wish to be removed from our mailing list, or if the addressee is no longer employed by your organization please notify AFML/LPJ ,*W-P AFB, OH 45433 to help us maintain a current mailing list".*

Copies of this report should not be returned unless return is required by security considerations, contractual obligations, or notice on a specific document.

AIR FORCE/56780/6 August 1979 — 100

UNCLASSIFIED

SECURITY CLASSIFICATION OF THIS PAGE (When Data Entered)

REPORT DOCUMENTATION PAGE	READ INSTRUCTIONS BEFORE COMPLETING FORM
1. REPORT NUMBER: AFML-TR-79-4001	2. GOVT ACCESSION NO. / 3. RECIPIENT'S CATALOG NUMBER
4. TITLE (and Subtitle): TITANIUM COMBUSTION RESEARCH PROGRAM and User's Manual for Deck CCD 1152-0.0.	5. TYPE OF REPORT & PERIOD COVERED: Final Technical Report December 1975 to September 1978 – 30 Nov 78
	6. PERFORMING ORG. REPORT NUMBER: FR-10748
7. AUTHOR(s): M. R. Glickstein	8. CONTRACT OR GRANT NUMBER(s): F33615-76-C-5041
9. PERFORMING ORGANIZATION NAME AND ADDRESS: United Technologies Corporation, Pratt & Whitney Aircraft Group, Government Products Division, West Palm Beach, FL	10. PROGRAM ELEMENT, PROJECT, TASK AREA & WORK UNIT NUMBERS: 73120223 / 02
11. CONTROLLING OFFICE NAME AND ADDRESS: Air Force Materials Laboratory, Air Force Systems Command, Wright-Patterson Air Force Base, Ohio 45433	12. REPORT DATE: March 1979
	13. NUMBER OF PAGES: 54
14. MONITORING AGENCY NAME & ADDRESS (if different from Controlling Office)	15. SECURITY CLASS. (of this report): Unclassified
	15a. DECLASSIFICATION/DOWNGRADING SCHEDULE: N/A

16. DISTRIBUTION STATEMENT (of this Report)

Approved for public release; distribution unlimited.

17. DISTRIBUTION STATEMENT (of the abstract entered in Block 20, if different from Report)

PWA-FR-10748, PWA-FR-10755

18. SUPPLEMENTARY NOTES

In part, sponsored by NASA-Lewis Research Center, Cleveland, Ohio.

19. KEY WORDS (Continue on reverse side if necessary and identify by block number)

Titanium Combustion
Laser Ignition
Self-Sustained Combustion
Ignition-Combustion Model
Compressor Environment
Titanium Compressor Airfoils
Metal Combustion Model

20. ABSTRACT (Continue on reverse side if necessary and identify by block number)

Titanium and its alloys are known to undergo self-sustained combustion in aerodynamic environments. Energy in several forms, i.e., radiation, frictional heating, or aerodynamic heating can be sufficient to bring the matter to a condition where self-sustained combustion can occur. The phenomenon has been of interest in the laser effects-vulnerability area, and also in aircraft propulsion systems, where titanium alloys are extensively used.

DD FORM 1 JAN 73 1473 EDITION OF 1 NOV 65 IS OBSOLETE

UNCLASSIFIED

SECURITY CLASSIFICATION OF THIS PAGE (When Data Entered)

392 887 79 08 8 077

ABSTRACT (CONTINUED)

Titanium and its alloys are known to undergo self-sustained combustion in aerodynamic environments. Energy in several forms, i.e., radiation, frictional heating, or aerodynamic heating can be sufficient to bring the matter to a condition where self-sustained combustion can occur. The phenomenon has been of interest in the laser effects-vulnerability area, and also in aircraft propulsion systems, where titanium alloys are extensively used.

An extensive program of analytical and experimental investigation has been in progress for the past three years to establish the environmental parameters which govern the ignition and self-sustained combustion of a selected representative titanium alloy (Ti-8Al-1Mo-1V) over a range of aerodynamic environments.

An analytical model has been evolved to predict the ignition and subsequent self-sustained combustion of titanium alloys. Numerical finite-difference techniques are used to produce simultaneous solutions of the equations for heat and mass transfer in the aerodynamic boundary layer, transient thermal conduction in the solid metal, phase change and liquid metal flow from the melting surface, and retention of liquid metal on the solid substrate, with subsequent thermal interaction. Appropriate models describe the oxidation kinetics at the metal surface over the range of conditions from ambient temperature to the metal melting temperature, and allow the prediction of metal ignition due to a variety of ignition modes, i.e., radiation, mechanical friction and exposure to high ambient temperatures.

FOREWORD

The work described in this Final Report was supported by the U. S. Air Force through the Air Force Materials Laboratory, Wright-Patterson AFB, Ohio, under Contract F33615-76-C-5041, 73120223. Dr. S. R. Lyon (AFML/LPJ) is the Project Engineer, and the work covered by this report was performed at Pratt & Whitney Aircraft Government Products Division between 1 December 1975 and 30 November 1978. This work was partly sponsored by NASA-Lewis Research Center, Cleveland, Ohio.

The following GPD personnel contributed to the technical effort and preparation of this report: Dr. M. R. Glickstein (Program Manager and Principal Investigator); R. L. Baricevich — computing analysis and model development; R. P. Holler — engineering analysis; R. J. Lisanke — test and data analysis; B. A. Manty — test direction and development of kinetic models.

Accession For
NTIS GRA&I ☐
DDC TAB ☐
Unannounced ☐
Justification
By
Distribution/
Availability Codes
Dist | Avail and/or special
A

TABLE OF CONTENTS

Section		*Page*
I	INTRODUCTION	1
II	PROGRAM SUMMARY	3
III	EXPERIMENTAL PROGRAM	4
	A. Test Facilities	4
	B. Test Run Procedure	6
	C. Test Specimens	6
	D. Experimental Results	9
IV	BASIC ANALYTICAL MODEL	19
	A. Ignition — Propagation Scenario	19
	B. Physical Model	19
	C. Analytical Approach	20
	D. Aerodynamic Processes	23
	E. Reaction Kinetics	23
	F. Liquid Metal Flow	24
	G. Program Logic	26
	H. Analytical Results	27
V	GENERALIZED ANALYTICAL MODEL	29
	A. Description of the Model	29
	B. Thermophysical Properties	29
	C. Structure of the Melt Flow	32
	D. Integral Transport Equations	33
	E. Local Transport Processes	35
	F. Stagnation Region Analysis	40
	G. Streamline Continuity	42
	H. Melt Leading Edge Flow	42
	I. Stagnation Point Data	43
	J. Airfoil Heat Transfer	46
	K. Computing Procedures	46
VI	SUMMARY OF RESULTS	48
	REFERENCES	54

LIST OF ILLUSTRATIONS

Figure		*Page*
1	Titanium Combustion Test Rig	4
2	Titanium Combustion Rig Test Section	5
3	Test Specimen in Holder	5
4	Arrangement of Laser Ignition and Photographic Recording System	7
5	Titanium Combustion Test Rig Setup	8
6	Titanium Specimen Configuration	10
7	Flat Plate Specimen	11
8	Combustion Propagation Across Specimen Airfoil	13
9	Time Sequence Composite of P&WA Specimen Combustion	14
10	Effect of Angle of Attack on Combustion Propagation	14
11	Leading Edge Burning Rate, Test PW 40	15
12	Leading Edge Burning Rate, Test PW 66	16
13	Leading Edge Burning Rate, Test PW 67	16
14	Leading Edge Burning Rate, Test PW 71	17
15	Relation of Burning Rate to Airstream Velocity	17
16	Threshold of Self-Sustained Combustion	18
17	Physical Model of Airfoil Combustion	20
18	Lumped Mass Thermal Model	21
19	Liquid Flow Model	25
20	Analytical Model Logic Diagram	26
21	Comparison of Analytical Simulation With Actual Test Results	28
22	Generalized Configuration — Burning Blade	30
23	The Ti-0 Phase Diagram up to 35 wt % Oxygen After Schofield and Bacon	31
24	Enthalpy of Titanium-Oxygen System as Function of Temperature	32
25	Local Velocity Profiles and Nomenclature Used in Melt Flow Analysis	33

ILLUSTRATIONS (Concluded)

Figure		*Page*
26	Streamline Indexing System	34
27	Typical Temperature — Concentration Relationship in Melt	39
28	Typical Temperature — Enthalpy Relationship in Melt	40
29	Stagnation Point Region of Burning Airfoil	40
30	Heat Flow and Velocity Relationship at Burning Leading Edge	41
31	Leading Edge of Melt	43
32	Relative Thickness of Liquid Metal Film at Stagnation Point	44
33	Comparison of Oxygen Concentration in Gas and in Metal at Gas-Metal Interface	45
34	Mass Transfer Stanton Number Predicted by Metal Diffusion Model	45
35	Generalized Combustion Program Logic	47

SECTION I

INTRODUCTION

Titanium and titanium alloys are used extensively in aerospace systems because of their high strength-to-density ratio, temperature resistance and excellent corrosion behavior. Titanium alloys have been widely applied to aircraft structural components, and to turbine engine and compressor parts. As titanium alloys have found application in different environments, especially at increasingly higher temperatures and pressures, a renewed interest has developed in their ignition and combustion behavior in air.

Within the last ten years, the incidence of titanium fires in gas turbine engines has markedly increased. Most frequently, catastrophic massive-metal fires have been observed during test cell performance evaluations. A number of factors are involved in this trend; most notably, the increase in thrust-to-weight ratio of current engines. Lower weight demands a more flexible engine and lighter components and these factors, when added to the desire for more thrust, result in increased pressure, temperature and flow, providing an environment conducive to ignition, self-sustained combustion and propagation of a titanium fire.

To date, the primary remedy has involved substitution of steels for selected titanium parts, with a resultant weight penalty, and increase in the rotor/stator clearances with a resulting performance penalty. As these penalties may be unacceptable in certain "performance-driven" military systems, the Air Force has initiated a program to understand the phenomena and develop materials approaches to eliminate catastrophic failure.

The combustion of titanium has been extensively investigated, with the vast majority of studies concerned with powdered metals, wires and single droplets. White and Ward (Reference 1) provide a comprehensive literature review of the ignition of metals in oxygen and mixed-oxygen atmospheres prior to 1966. The most notable of these earlier studies, insofar as this effort is concerned, is the work of Littman, et al., (Reference 2) which is one of the few studies concerned with the spontaneous ignition of massive metal. The dependence of fracture initiated ignition on pressure and atmosphere reported by Littman, et al., has been used to set the limits for titanium usage in gas turbine engines as recently as early 1976. This has been the trend, even though fracture-initiation may be the least important source of ignition in the modern compressor environment.

With the advent of high energy CO_2 lasers, several investigators have noted laser-initiated combustion of titanium and its alloys. Most of these studies have investigated the initial conditions and dependence of laser burnthrough times on such variables as beam size, Mach number, velocity, or specimen geometry. More recently, the Air Force has initiated several studies to consider various types of ignition, such as rubbing or rapid heating, and to investigate and model self-sustained combustion of titanium alloys in the gas turbine engine compressor environment. Wolf (Reference 3), has investigated the isothermal oxidation kinetics of several titanium alloys and the conditions which lead to ignition of thin sheets. With heating rates on the order of 100°C/sec unalloyed titanium sheet has been ignited at approximately 500°C in 200 Torr stagnant oxygen. Clark, et al. (Reference 4 and 5), are investigating the combustion mechanism of a variety of titanium alloys, as part of a continuing program at the Bureau of Standards. This excellent work is providing a first definition of the basic metal combustion process as well as temperature measurements during combustion.

To date, there has been little effort to understand the ignition and propagation of a titanium fire on massive blade-like shapes in flowing gas. Given a rectangular or airfoil shaped titanium alloy in a compressor environment and sufficient energy for ignition at a corner or edge, it is

expected that several factors will determine whether propagation occurs. The combination of gas-temperature, pressure and velocity control the concentration of reactants at a combusting surface, the aerodynamic shear for removal of melted materials, and the convective cooling of the surface. No prior efforts have determined the dependence of ignition or propagation on these factors. The objective of this effort was to develop an understanding of the interrelationships of the important factors governing ignition and combustion propagation over a broad range of environmental conditions.

The efforts described in this report include an experimental evaluation of the geometrical and environmental effects on the combustion of Ti 8-1-1 airfoils, and the development of an analytical model for the prediction of the ignition and subsequent combustion of titanium and its alloys.

SECTION II

PROGRAM SUMMARY

A comprehensive program has been conducted to develop an in-depth understanding of the interrelationship of the factors governing the ignition-propagation sequence of titanium over a broad range of environmental conditions, including those of current and advanced gas turbine engine operations. Included in the program were an experimental investigations of titanium combustion, and an extensive analytical effort to develop a predictive model for evaluating the susceptibility of titanium alloys to ignition and subsequent propagation.

In the experimental phase of the program, 73 combustion tests were performed with titanium 8-1-1 specimen airfoils over a wide range of temperature, pressure, and airstream velocity. Combustion was initiated with a laser ignition source, and the ignition-combustion sequence for each test was recorded with high speed cinematography. Subsequent phenomenological analysis, and frame by frame differential motion analysis provided the basis for development of the analytical models.

In the initial analytical phase, a phenomenological sequence was described, based on the observed test results, and a model was proposed to explain the observed phenomena. The model was subsequently developed, programmed for computer analysis, and compared with test data to evaluate its validity. The model appeared to be qualitatively in agreement with test data, but quantitative disagreement of certain aspects of the model indicated the need for further refinement. In particular, liquid melt spread-rates over the airfoil and spanwise spreading of the burning zone were inconsistent with observed data.

In the advanced development phase of the analytical effort, the model was generalized to include centrifugal force effects, thus allowing analysis of rotating compressor blades. A detailed model was developed for the flow of melt and for the transfer of heat and oxygen within the flowing melt. In addition, physical property models have been modified to incorporate the effect of dissolved oxygen, and an aerodynamic loss model has been incorporated in the liquid flow equations to account for stripping of melt from the burning surface.

SECTION III

EXPERIMENTAL PROGRAM

An experimental program was conducted to provide supporting data for development of the analytical model. A total of 73 tests were conducted, of which 44 resulted in burn damage to the airfoil specimen.

A. TEST FACILITIES

The titanium combustion test rig used for these studies is a small wind tunnel driven from a 241 MPa (350 psi) compressed air supply. Ancillary conditioning equipment permits the simulation of a wide range of environmental combinations of air pressure — up to 0.97 MPa (140 psia), temperature — up to 550°C (1022°F) and velocity — up to 335 m/sec (1100 ft/sec). Test specimens are mounted in a rectangular test chamber. Instrumentation is provided to monitor pressure and temperature at strategic locations in/on the rig. The overall arrangement of the test rig is shown in Figure 1.

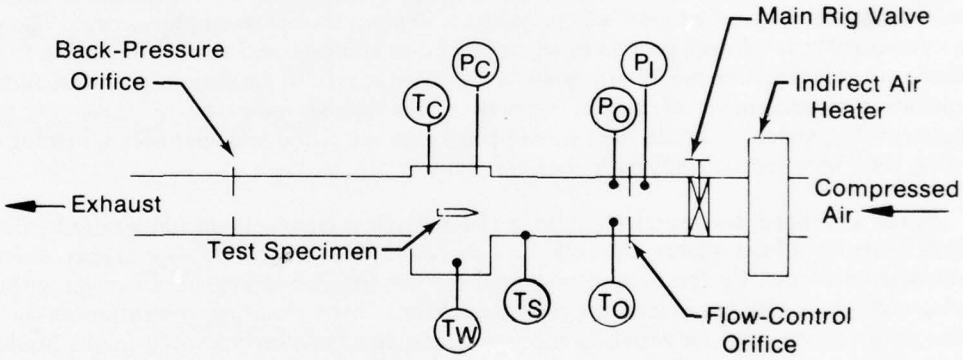

Figure 1. Titanium Combustion Test Rig

Air, supplied from a large compressor, is passed through a gas-fired indirect heater and a flow-measuring orifice prior to entering the test section. The test section, shown schematically in Figure 2 is a 19.1 mm by 50.1 mm (0.75 in. by 2.0 in.) rectangular channel with a bellmouth inlet and 75 mm (3.0 in.) of straight section upstream of the airfoil leading edge. The test specimen mounts in a cylindrical carrier which is inserted into the test section. (See Figure 3.) Orifice plates, upstream and downstream of the test section, provide control of the flowrate and pressure level. Thermocouples are positioned to provide temperatures at the flow-measuring orifice, in the specimen test chamber, on the rig skin, and at the laser and camera windows. Points are provided to measure flow-control orifice upstream and downstream pressure as well as static pressure in the test chamber. (See Figure 1.) Airstream velocity is determined by calculation using the differential pressure across the flow-control orifice.

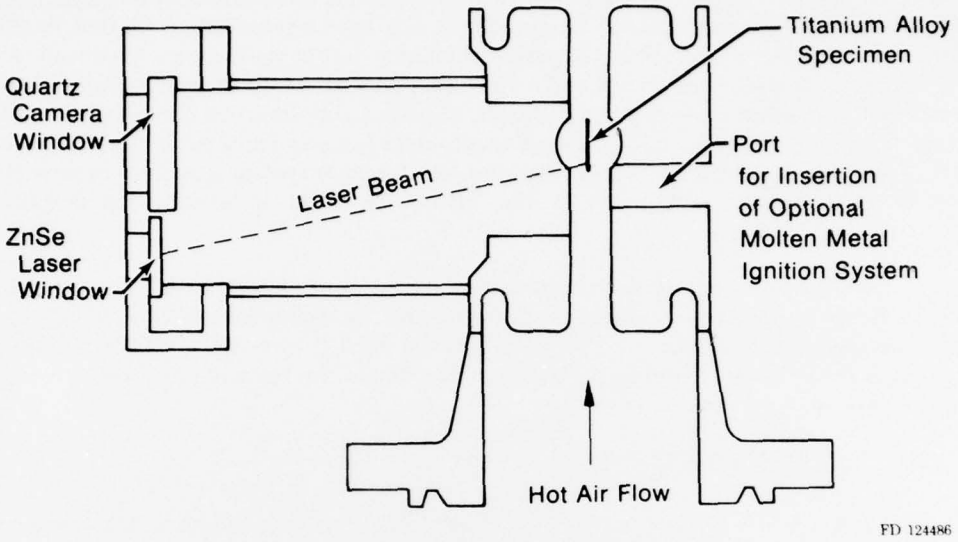

Figure 2. Titanium Combustion Rig Test Section

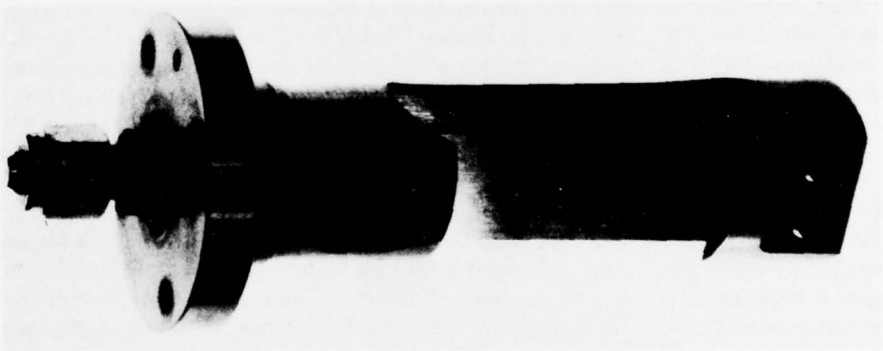

FAE 343164

Figure 3. Test Specimen in Holder

The test section has two windows, one for laser irradiation of the specimen and one for photographic and video viewing of the test specimen. These windows are mounted in a port on the side of the rig approximately 20.3 cm (8 in.) from the test specimen. The window for the camera is optically flat, fused quartz which is 63.5 mm (2.500 in.) in diameter and 12.7 mm (0.500 in.) thick. The laser beam window is 38.1 mm (1.500 in.) in diameter and 6.35 (0.250 in.) thick zinc selenide. This material offers excellent transmissivity for the 10.6-micron wavelength emission of the CO_2 laser beam. The zinc selenide window has an antireflective coating on both faces to minimize reflection and scatter of the beam. The quartz window has excellent optical clarity for visible light but will not transmit the CO_2 laser light, thus protecting the camera lens from scattered reflections of the laser beam. The windows are protected from the high-temperature test environment by a water jacket to absorb conducted heat in the metal housing and an air injection system to film-cool the optical surfaces.

The arrangement of the test section and other supporting test equipment is shown in Figures 4 and 5. Because of environmental requirements, the laser equipment is located in the air-conditioned control room and the beam passed through a port in the concrete blast wall. A high-speed Hycam motion picture camera and a video camera with a tape recording/playback system are arranged, through the use of a beamsplitter, to permit simultaneous photographic recording and real-time video observation. The energy required for specimen ignition is supplied by a CRL Model 41 laser. This electric-discharge, water-cooled CO_2 laser system is capable of providing an output of approximately 250 watts in the TEMoo mode at a transmission frequency of 10.6 microns.

The beam is defocused at the specimen to a diameter of approximately 2 mm to yeild an incident average power density, after transmission losses, of approximately 2.5 Kw/cm^2 absorbed by the specimen. A coincident helium-neon laser is used to provide a visible red beam for alignment of the CO_2 laser beam on the titanium specimen. This red alignment beam is observed using the videotape system.

B. TEST RUN PROCEDURE

Prior to a test run, the test specimen is secured in the specimen holder and mounted in the test chamber. Run values for air velocity and chamber pressure are established by installing a specific combination of flow-control and backpressure orifices in the test rig. After setting the heater to the desired temperature, airflow is introduced into the system and the test chamber allowed to come to thermal equilibrium. Near thermal equilibrium, the laser optics are aligned using the visible helium-neon laser beam and the videotape system. Specimen illumination during laser, video and high-speed camera alignment and focusing is provided by a high intensity light transmitted from its source by fiber optics. During the run, light from the specimen ignition and burning is sufficiently intense to permit photodocumentation of burn propagation and melt transportation. An event marker (light pulse) is recorded on the side of the film on all runs to annotate the start and finish of the laser action during the run. The high-speed films are also marked with light pulses from a 1000-Hz timing generator to provide an absolute time reference for event sequences.

Just prior to the start of a run, final temperature and pressure adjustments are made by judicious throttling of the hot air valve and a cold air bleed input valve. Simultaneously, a final adjustment, if required, is made to the laser alignment. Final run parameters are then recorded and the test is initiated by a time-sequenced switch which, when actuated, starts the high-speed camera. Approximately 2 sec after camera start the sequencer opens the laser shutter to irradiate the specimen, thereby starting the run. The laser remains on for 5 sec before the sequencer closes the shutter. This time can be manually overridden when ignition occurs before the 5 sec has elapsed. The camera is allowed to run out of film (about 16 sec) and is sequenced off at approximately 20 sec. The video system remains on at all times in a CCTV mode. Video tape recording is controlled manually during a run sequence. The instant replay and a slow-motion/stop-frame capability of the color video recording permits immediate review of the test run for its potential impact on the next test run.

C. TEST SPECIMENS

All combustion tests were performed with a single titanium alloy. Because of its extensive use in gas turbine engine applications, Ti-8Al-1Mo-1V was selected to provide a baseline performance upon which to develop the analytical model.

The basic specimen configuration was an uncambered airfoil, aerodynamically representative of current compressor airfoils. The design used, shown in Figure 6, is an uncambered airfoil

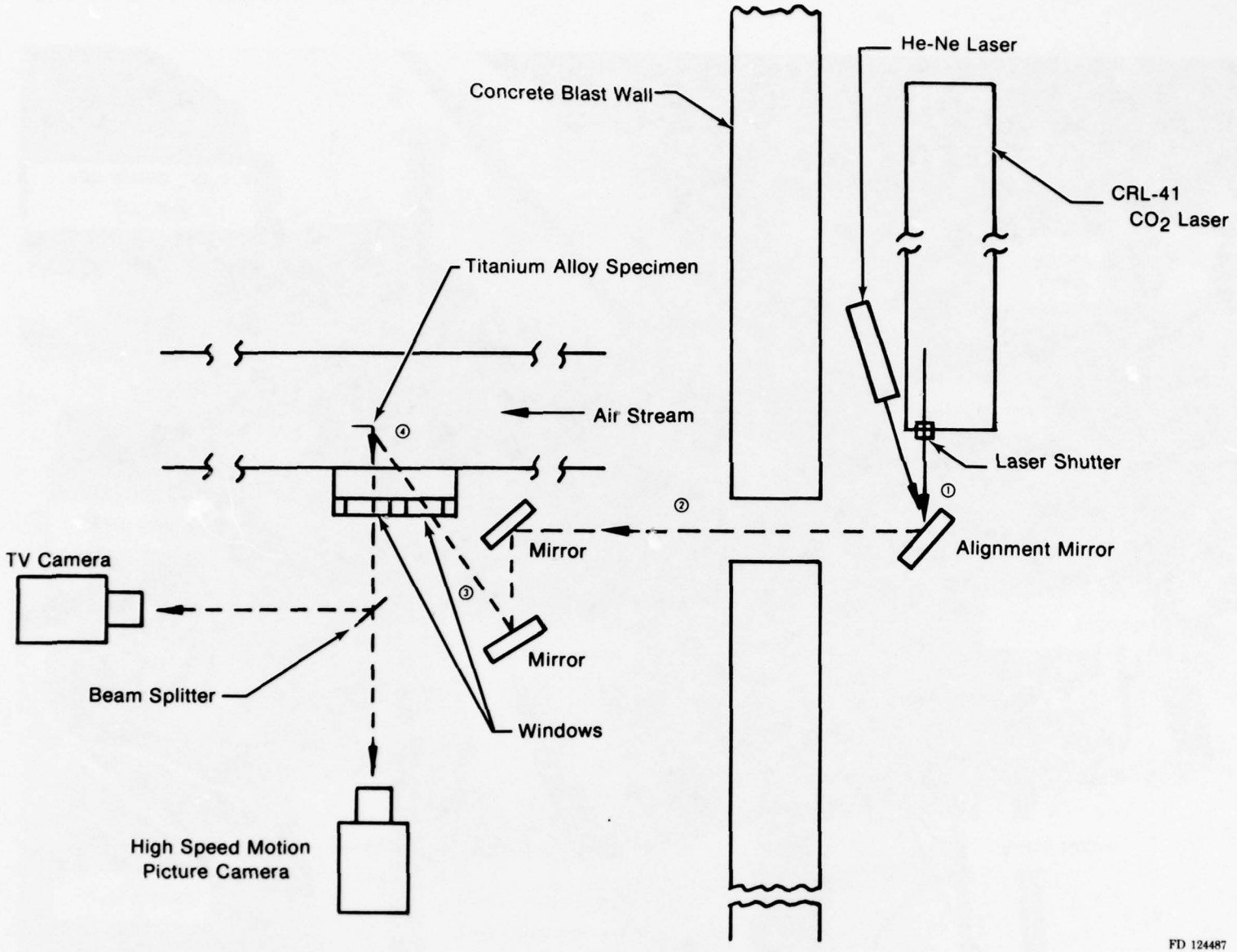

Figure 4. Arrangement of Laser Ignition and Photographic Recording System

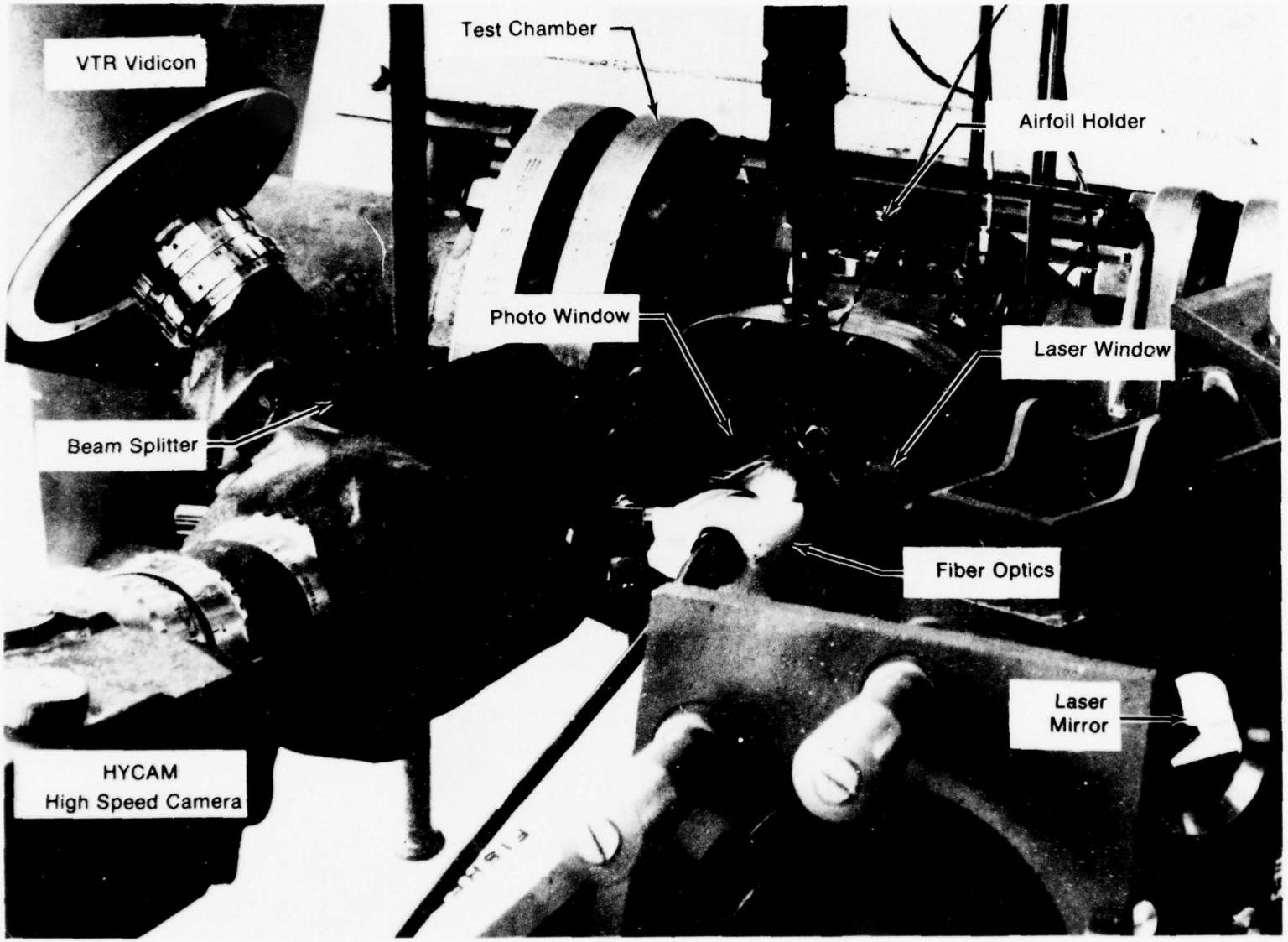

Figure 5. Titanium Combustion Test Rig Setup

with cylindrical surfaces of 115.6 mm (4.55 in.) radius, rounded leading and trailing edges with nominal radius of 0.076 mm (0.003 in.), and chord of 25.4 mm (1.00 in.). The maximum thickness is approximately 1.27 mm (0.050 in.), and the total contoured span is 56.39 mm (2.220 in.). The specimens were machined from sheet by EDM, polished to reduce surface roughness, and vapor-blasted to yield a uniform matte surface. All specimens were then profiled to determine their exact contour, and profiles were recorded for future reference.

Twenty-three tests were performed with specimen airfoils in the vapor-blasted condition. Because of apparent difficulty in attaining ignition, the remaining specimens were coated with a black nickel coating, increasing absorptivity to near 60%, thereby maximizing coupling of laser energy to the specimens. The thin nickel plating was applied only on a small area at the leading edge ignition site, thereby having no effect on subsequent combustion. Four specimens were prepared as flat plates, with a knife-edge on one side to facilitate ignition, as shown in Figure 7.

D. EXPERIMENTAL RESULTS

A total of 73 laser-initiated combustion tests have been conducted in the test program, of which 44 sustained some level of damage, and 27 underwent self-sustained combustion. No attempt was made to study the laser-initiated ignition process in detail, the laser being used only to provide a reproducible and remote ignition source.

Data resulting from the test program are tabulated in Table I. Test conditions of static pressure, total temperature, free-stream air velocity and Mach number are tabulated with results listed as material combusted or lost (% damage). Damage is defined as the percent of exposed specimen lost (burned) during the test, excluding the portion held in the support. As combustion nears the support (holder), the relatively massive metal interferes with the flow, and acts as a heat sink, always resulting in a significantly diminished combustion rate, or in extinction. Consequently, specimen damage above approximately 80% should be considered total self-sustained combustion of the metal. No attempt was made to account for this behavior by normalization of the data.

Figure 8 shows a movie frame sequence during the "steady state" portion of a typical test. This sequence, beginning after 40% of the chord has burned, is a flat plate specimen being tested under a complementary test program (under Contract N62269-77-C-0481). The bright areas represent molten titanium being spread over the airfoil by airstream friction. The flowing melt is seen to spread over the surface much more rapidly than the leading edge burns. Occasional flashes of sparks are seen in the background as melt is stripped from the burning surface by the airstream.

Figure 9 shows a time sequence composite for a typical test, developed from the cinematographic data. The burning leading edge is seen to rapidly progress across the specimen in the chordwise direction, then slowly burn in the spanwise direction.

The effect of aerodynamic angle of attack on the rate and nature of airfoil combustion is shown in Figure 10. Time sequence plots of the burning leading edge for two tests, PW66 and PW67, performed at the same environmental conditions but with different airfoil orientation are shown in Figures 10 (a) and 10 (b), respectively. With parallel flow (zero angle of attack), combustion is primarily in the chordwise direction, typical of most of the test results. The effect of inclining the airfoil 10 deg relative to the air stream direction is shown in Figure 10 (b). The effect of the difference in aerodynamics on combustion propagation is readily seen, and appears to be due to boundary layer separation on one side of the airfoil. Observation of the high speed movies of Test PW67 indicate that nearly all of the liquid metal flow is confined to the airfoil pressure surface. Chordwise propagation appears to be somewhat faster at zero angle of attack, but total propagation and the amount of resulting damage appear significantly greater for the 10 deg angle test.

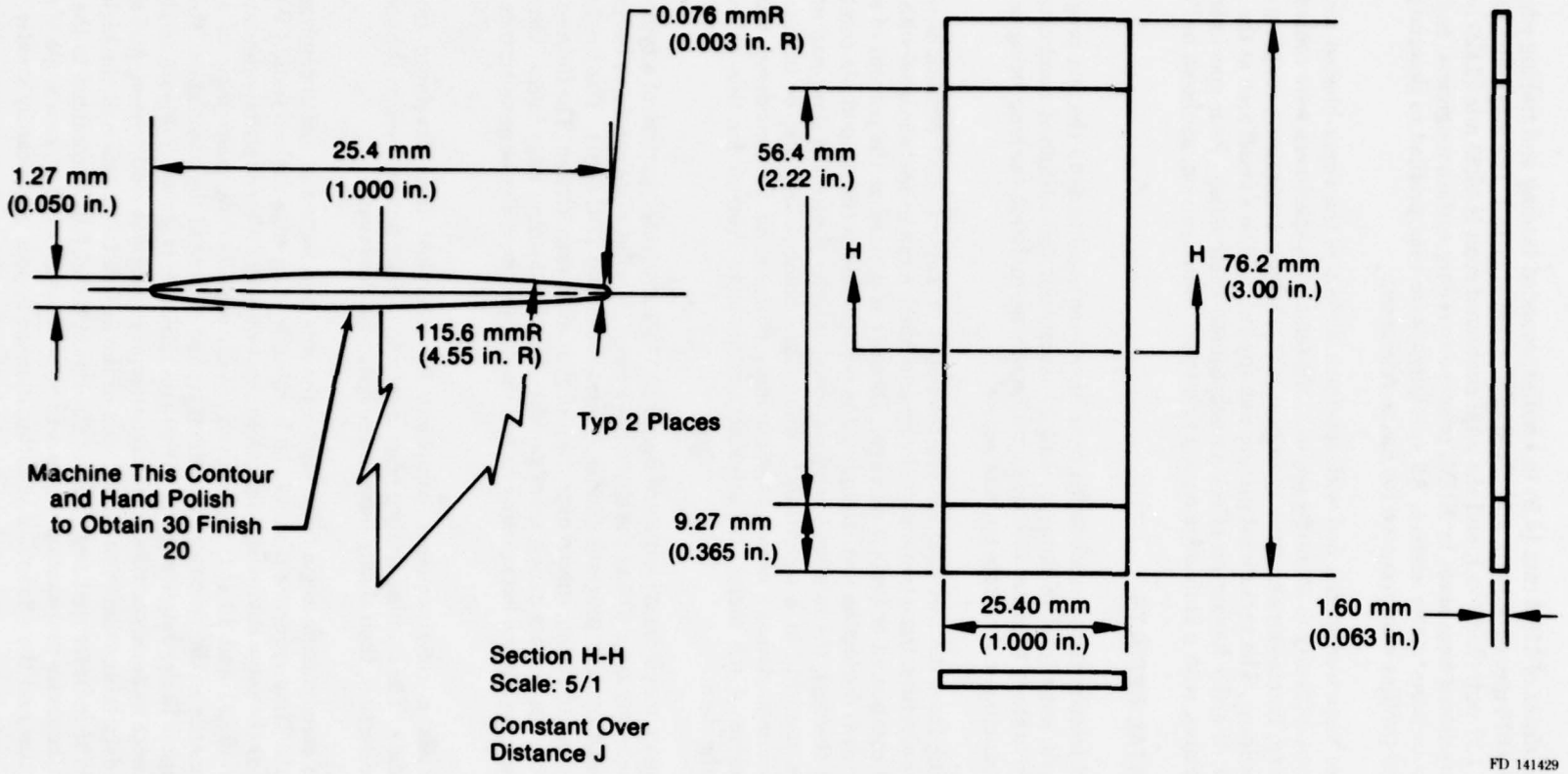

Figure 6. Titanium Specimen Configuration

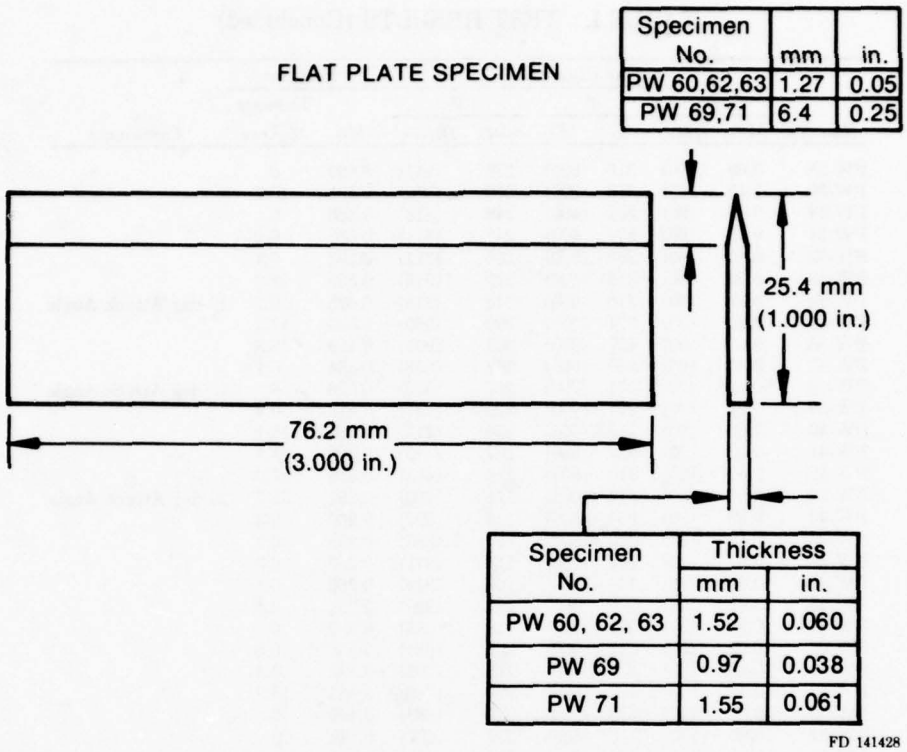

Figure 7. Flat Plate Specimen

TABLE I. TEST RESULTS

	Test Condition						*Results*		
	P_s		T_t		V			*Damage*	
Run No.	*MPa*	*(psia)*	*°C*	*(°F)*	*m/sec*	*(ft/sec)*	*Mn*	*% Loss*	*Comments*
PW-1	0.45	(65)	204	(400)	186	(609)	0.432	0	
PW-2	0.69	(100)	204	(400)	186	(609)	0.432	0	
PW-3	0.97	(140)	204	(400)	186	(611)	0.433	0	
PW-4	0.69	(100)	316	(600)	212	(696)	0.444	0	
PW-5	0.69	(100)	316	(600)	209	(687)	0.438	0	
PW-6	0.69	(100)	204	(400)	188	(616)	0.436	0	
PW-7	0.97	(140)	204	(400)	116	(379)	0.265	0	
PW-8	0.55	(80)	204	(400)	115	(378)	0.265	0	
PW-9	0.21	(30)	316	(600)	103	(338)	0.371	0	
PW-10	0.31	(45)	316	(600)	130	(426)	0.269	0	
PW-11	0.21	(30)	407	(765)	144	(472)	0.277	0	
PW-12	0.21	(30)	316	(600)	128	(419)	0.264	0	
PW-13	0.21	(30)	427	(800)	139	(457)	0.264	0	
PW-14	0.21	(30)	318	(605)	59	(192)	0.120	0	
PW-15	0.21	(30)	316	(600)	41	(136)	0.085	0.2	
PW-16	0.45	(65)	427	(800)	325	(1066)	0.637	19.3	
PW-17	0.45	(65)	316	(600)	305	(1001)	0.653	0	
PW-18	0.45	(65)	371	(700)	305	(1000)	0.649	0	
PW-19	0.45	(65)	427	(800)	324	(1062)	0.634	0	
PW-20	0.52	(75)	482	(900)	317	(1039)	0.595	19.2	
PW-21	0.52	(75)	457	(855)	313	(1027)	0.598	15.6	
PW-22	0.62	(90)	482	(900)	329	(1079)	0.619	0	
PW-23	0.86	(125)	316	(600)	276	(905)	0.586	0	
PW-24	0.62	(90)	427	(800)	304	(998)	0.593	14.4	
PW-25	0.62	(90)	371	(700)	290	(951)	0.589	13.0	
PW-26	0.62	(90)	371	(700)	291	(956)	0.592	13.2	
PW-27	0.61	(89)	371	(700)	285	(935)	0.579	0	

TABLE I. TEST RESULTS (Concluded)

	Test Condition						Results		
	P_s		T_t		V			Damage	
Run No.	MPa	(psia)	°C	(°F)	m/sec	(ft/sec)	Mn	% Loss	Comments
PW-28	0.69	(100)	316	(600)	278	(911)	0.590	0	
PW-29	0.45	(65)	316	(600)	278	(912)	0.591	10.7	
PW-30	0.62	(90)	204	(400)	248	(813)	0.585	0	
PW-31	0.45	(65)	204	(400)	247	(811)	0.583	0.2	
PW-32	0.62	(90)	260	(500)	265	(871)	0.593	0.4	
PW-33	0.62	(90)	316	(600)	279	(915)	0.593	12.2	
PW-34	0.62	(90)	316	(600)	248	(815)	0.525	0.2	10 deg Attack Angle
PW-35	0.45	(65)	371	(700)	290	(950)	0.589	13.4	
PW-36	0.62	(90)	427	(800)	302	(991)	0.589	13.8	
PW-37	0.45	(65)	260	(500)	262	(858)	0.584	0.1	
PW-38	0.62	(90)	371	(700)	261	(856)	0.526	0	10 deg Attack Angle
PW-39	0.21	(30)	371	(700)	290	(951)	0.589	0.4	
PW-40	0.62	(90)	316	(600)	126	(412)	0.260	16.1	
PW-41	0.62	(90)	427	(800)	137	(449)	0.260	21.2	
PW-42	0.45	(65)	316	(600)	123	(405)	0.255	17.0	
PW-43	0.62	(90)	316	(600)	121	(398)	0.251	35.7	10 deg Attack Angle
PW-44	0.62	(90)	260	(500)	119	(392)	0.260	9.3	
PW-45	0.45	(65)	260	(500)	117	(385)	0.255	0.2	
PW-46	0.62	(90)	204	(400)	113	(371)	0.260	6.0	
PW-47	0.62	(90)	149	(300)	106	(349)	0.260	0.1	
PW-48	0.31	(45)	316	(600)	121	(398)	0.251	0.1	
PW-49	0.21	(30)	371	(700)	118	(386)	0.232	0	
PW-50	0.62	(90)	316	(600)	208	(681)	0.435	0.5	
PW-51	0.45	(65)	371	(700)	216	(708)	0.432	0.5	
PW-52	0.48	(70)	427	(800)	226	(740)	0.433	16.3	
PW-53	0.97	(140)	316	(600)	210	(688)	0.439	0	
PW-54	0.69	(100)	316	(600)	209	(687)	0.439	0	
PW-55	0.62	(90)	427	(800)	226	(743)	0.435	45.9	
PW-56	0.69	(100)	316	(600)	206	(677)	0.432	13.7	
PW-57	0.97	(140)	204	(400)	185	(607)	0.430	10.4	
PW-58	0.69	(100)	204	(400)	185	(608)	0.430	0.3	
PW-59	0.45	(65)	427	(800)	225	(738)	0.430	20.8	
PW-60	0.62	(90)	427	(800)	226	(743)	0.435	0	
PW-61	0.62	(90)	427	(800)	226	(743)	0.435	0.7	
PW-62	0.62	(90)	427	(800)	226	(743)	0.435	0	
PW-63	0.62	(90)	427	(800)	226	(743)	0.435	0	
PW-64	0.97	(140)	482	(900)	44	(143)	0.079	56.2	
PW-65	0.97	(140)	316	(600)	38	(126)	0.079	1.0	
PW-66	0.97	(140)	427	(800)	46	(150)	0.086	30.3	
PW-67	0.97	(140)	427	(800)	46	(150)	0.086	82.6	10 deg Attack Angle
PW-68	0.69	(100)	316	(600)	199	(652)	0.415	1.1	10 deg Attack Angle
PW-69	0.69	(100)	316	(600)	206	(677)	0.432	10.4	0.97 mm thickness
PW-70	0.69	(100)	427	(800)	244	(799)	0.469	64.5	
PW-71	0.69	(100)	427	(800)	244	(799)	0.469	82.8	1.55 mm thickness
PW-72	0.62	(90)	427	(800)	271	(889)	0.525	0.1	10 deg Attack Angle
PW-73	0.62	(90)	371	(700)	288	(945)	0.585	1.3	

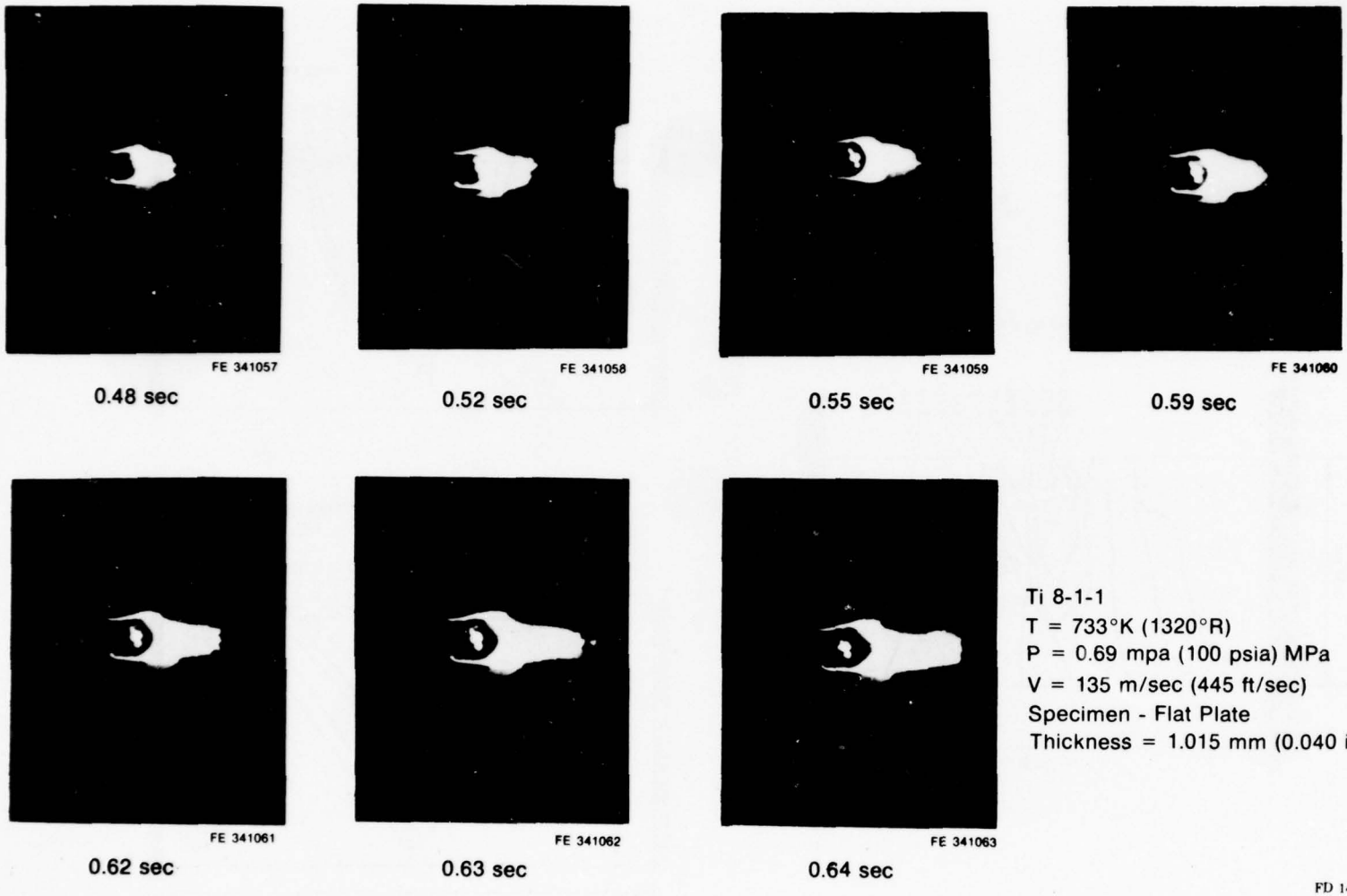

Figure 8. Combustion Propagation Across Specimen Airfoil

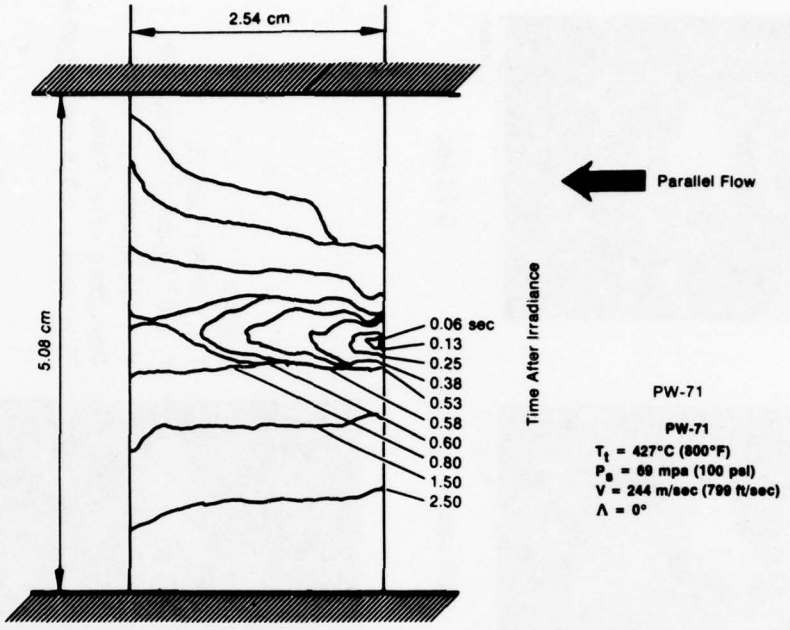

Figure 9. Time Sequence Composite of P&WA Specimen Combustion

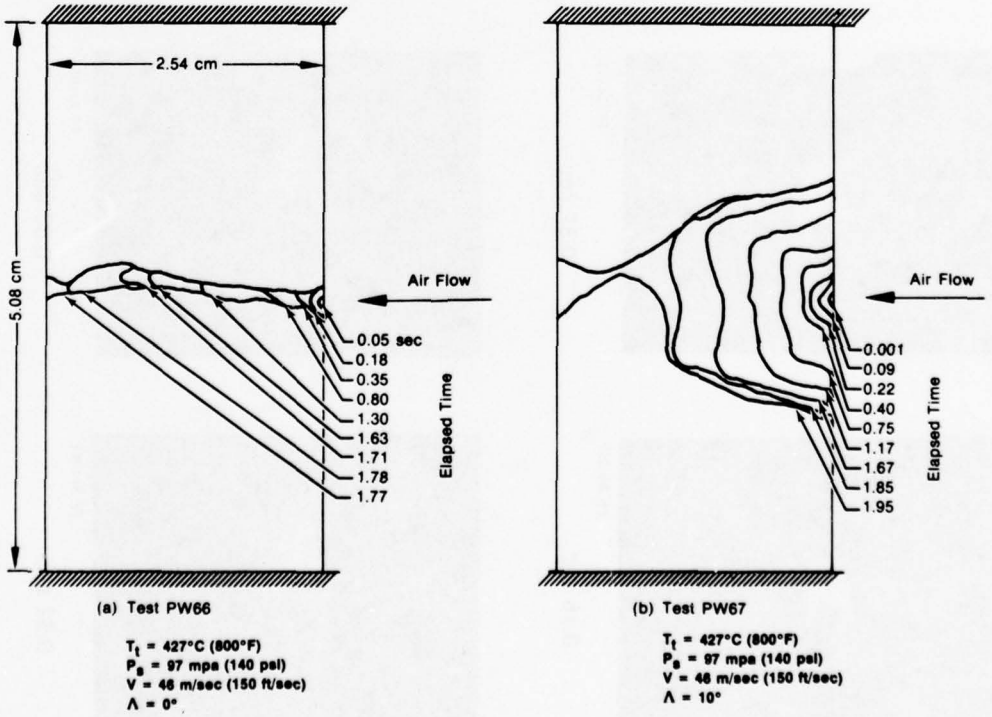

Figure 10. Effect of Angle of Attack on Combustion Propagation

Figures 11 through 14 illustrate the effect of test condition on the chordwise burning rate. Burning rates are observed to vary strongly with time, probably indicating a strong dependence on chordwise location and amount of downstream surface (toward trailing edge) covered with melt. For direct comparison, data should be considered at times corresponding to equal amounts of melt mass, which is equivalent to identical chordwise location. A composite of these data is shown in Figure 15, with burned mass (location) as a parameter. For the limited range of pressure and temperature considered in this figure, burning rate is observed to be strongly dependant on airstream velocity.

The effect of the environmental conditions on the threshold of self-sustained combustion is illustrated in Figure 16. In this figure the effect of pressure, velocity, temperature, and geometry is combined in the dimensionless Reynolds number at the leading edge, based on the leading edge thickness and all properties evaluated at the "melting film" temperature (average of airstream and titanium melting temperatures). Allowing for a moderate amount of data scatter, the curve in Figure 16 reasonably differentiates the combustion threshold. The illustrated curve is based on an earlier one-dimensional analysis of the combustion process, performed at P&WA prior to the current study.

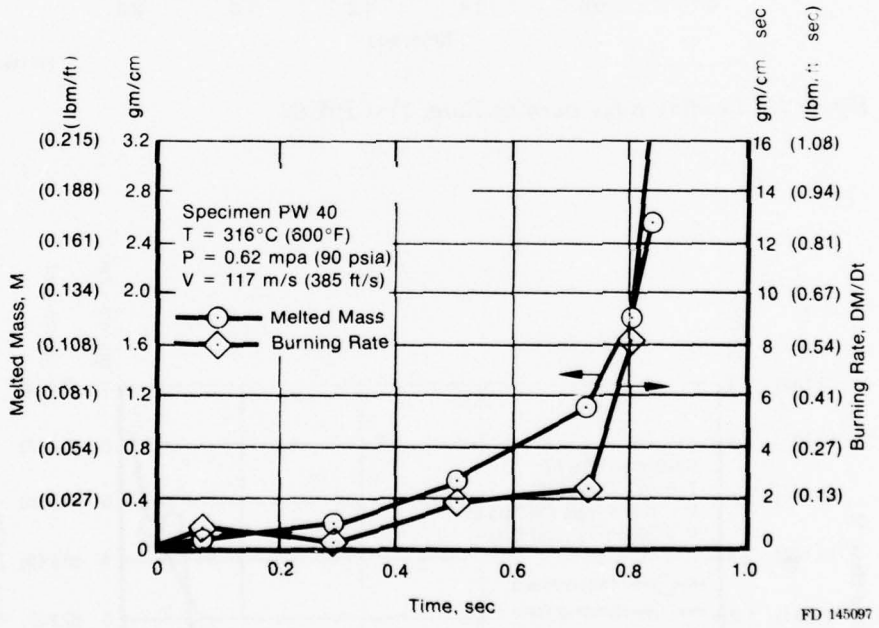

Figure 11. Leading Edge Burning Rate, Test PW 40

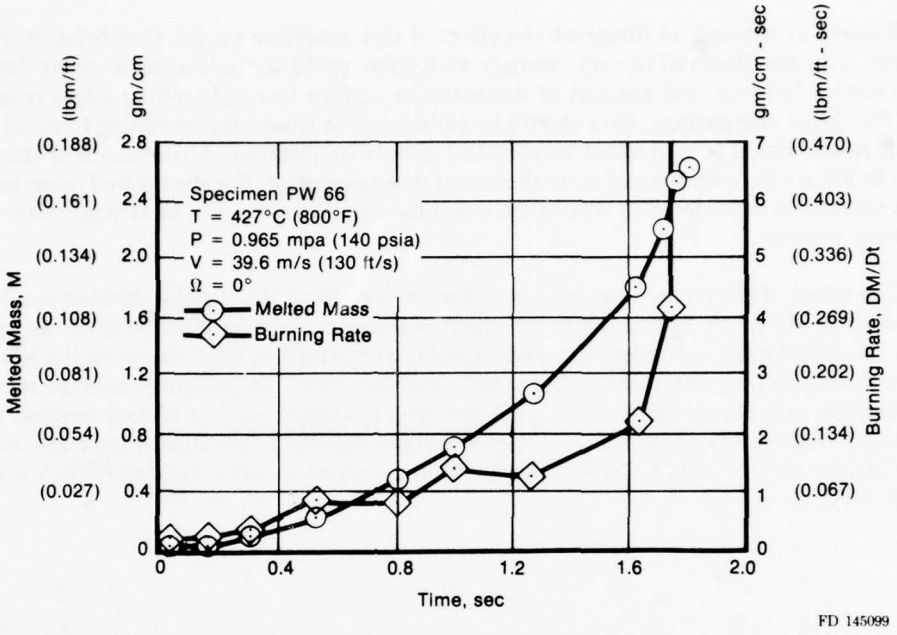

Figure 12. Leading Edge Burning Rate, Test PW 66

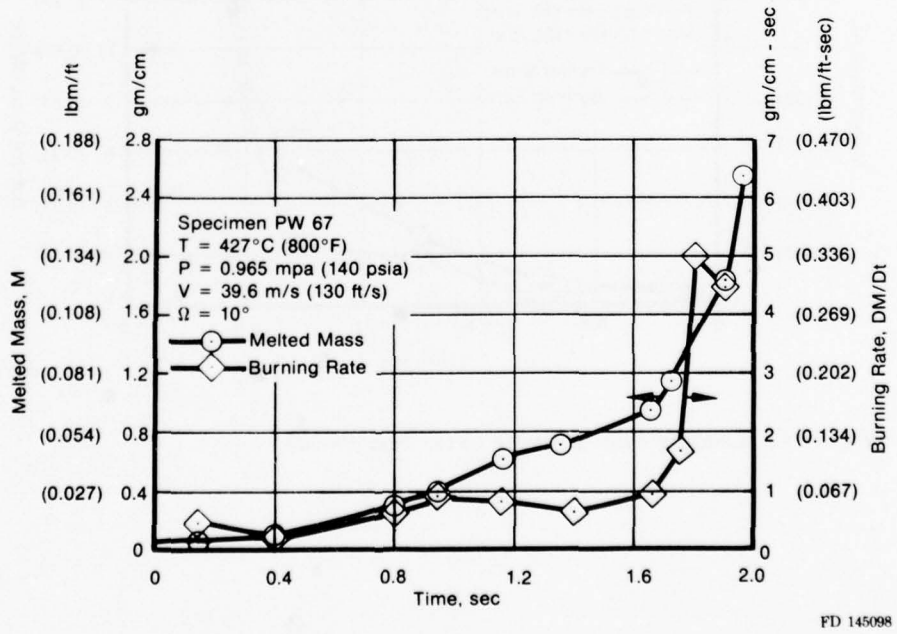

Figure 13. Leading Edge Burning Rate, Test PW 67

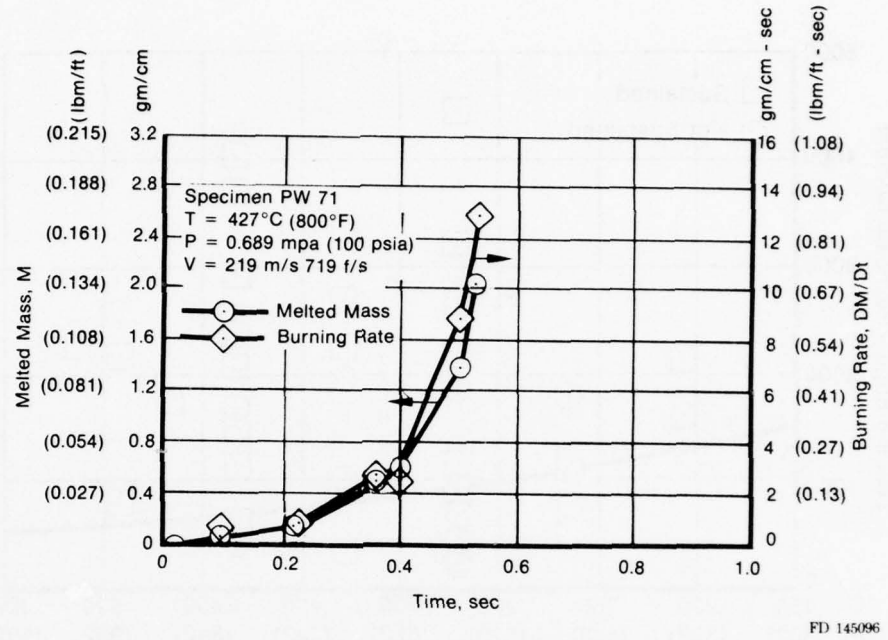

Figure 14. Leading Edge Burning Rate, Test PW 71

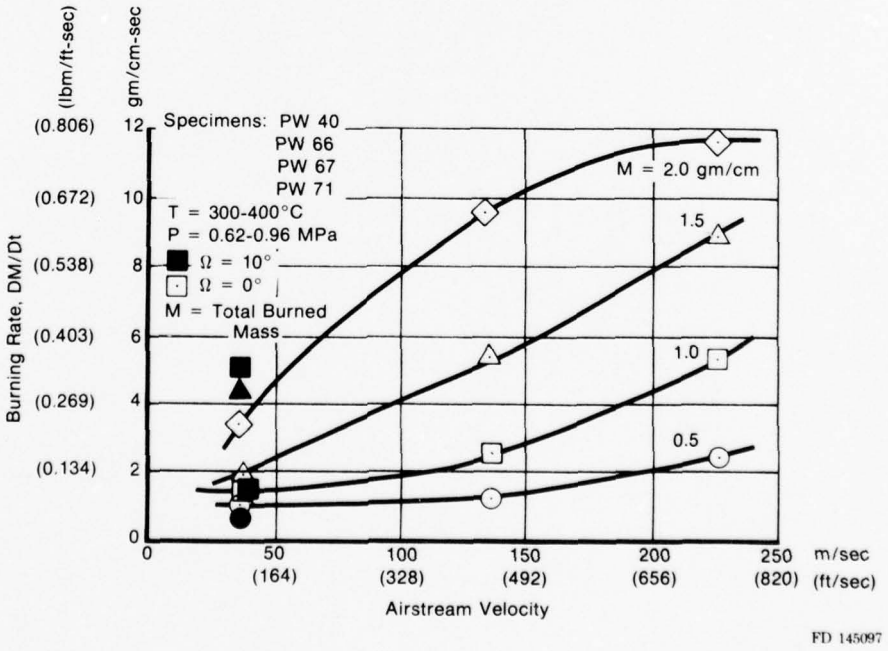

Figure 15. Relation of Burning Rate to Airstream Velocity

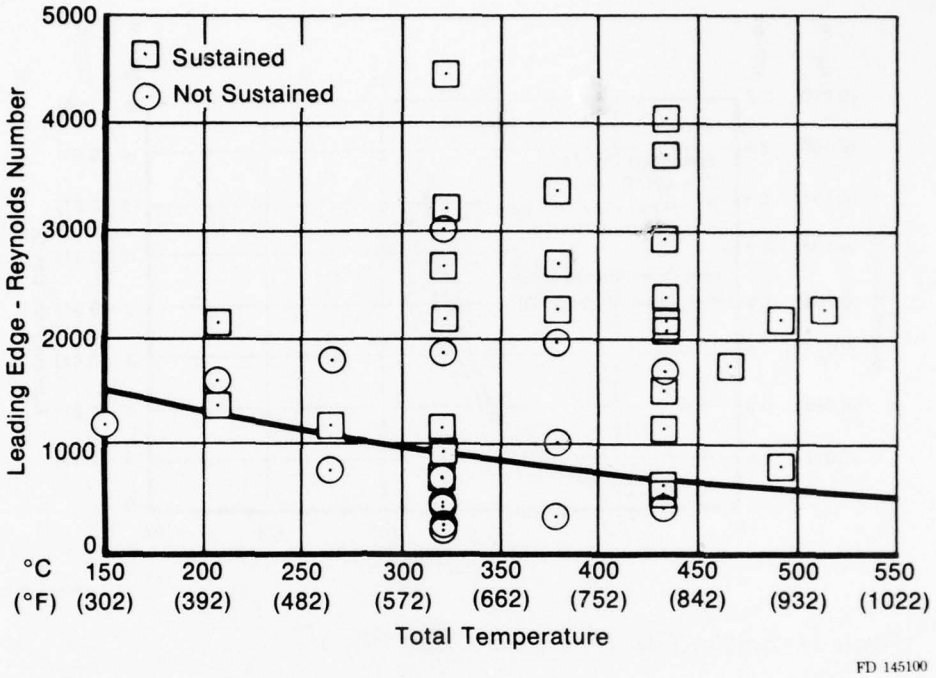

Figure 16. Threshold of Self-Sustained Combustion

SECTION IV

BASIC ANALYTICAL MODEL

To provide a procedure for predicting the fire susceptibility of titanium structures in aerodynamic environments, an analytical model has been developed. Based on experimental observations, a scenario was developed for the ignition-combustion process, a physical model was assumed to represent the scenario, and an analytical model was formulated to characterize the physical model. This initial (basic) model was developed for static systems, with no consideration of rotational motion.

A. IGNITION — PROPAGATION SCENARIO

In order to clarify the relationship of combustion rates, total damage and ignition, it is important to consider the entire ignition-propagation sequence with regard to the local environment. Based on observation of high speed movies and applied to a gas turbine engine environment, the following scenario can be developed to describe the titanium fire phenomena: A titanium specimen is exposed to and is in thermal equilibrium with an aerodynamic environment. Heat generated by normal oxidation is balanced by losses to the surrounding environment. An ignition initiation event creates an imbalance in this equilibrium system. Such an event may take one of several forms, i.e., heat input due to mechanical friction, thermal radiation, aerodynamic heating or fracture which produces an atomically fresh surface. In response to one of these events, metal temperature increases in the region of heat input, resulting in increased heat generation from oxidation. Heat loss to the environment and to the sample increases accordingly to establish a new equilibrium state. If thermal equilibrium is reached with the local metal surface temperature below its melting point, ignition does not occur, and the system returns to its original state when the ignition source is removed. If melting occurs, the material ignites and, with removal of the ignition source, may cease burning if the thermal balance is insufficient to supply the necessary latent heat to continue local melting. If the rate of local heat generation is greater than the rate of losses, self-sustained combustion occurs. In the case of self-sustained combustion and subsequent propagation, test results demonstrate that a significant amount of molten material is generated at the leading edge of the specimen and adheres to and flows over the surface in response to aerodynamic forces. This flowing liquid with considerable dissolved oxygen continues to react as it flows, thereby maintaining its liquid state and providing additional energy to the specimen by conduction. The adherence of this molten metal in certain environments is critical to the maintenance of self-sustained combustion, and is the principal mechanism for propagation of titanium combustion at moderate-to-great airstream velocities. In general, the transport of energy along the surface in the molten flow far exceeds the capability for heat loss by conduction with the solid substrate. A more accurate description of this process must come from analytical modeling.

B. PHYSICAL MODEL

The physical model, shown in Figure 17, describes the essential features of the combustion of a titanium airfoil in an airstream. This model formulated on the basis of photographic evidence from the test program, assumes that molten metal originates at the leading edge and flows on the surface in the direction of the airstream, driven along by aerodynamic shear and drag forces.

Part of the liquid is carried away by the airstream, the remainder being retained on the surface, where it continues to react. Some of the liquid solidifies as it flows over the surface, yielding its latent heat to the airfoil. As the process continues, the solidified "recast" layer subsequently melts and reacts, along with the original airfoil structure. Heat supplied to the

surface from external sources, plus heat flow from the reacting surface to the underlying solid substrate, provides the energy necessary to cause propagation of the process. Simultaneously, heat is lost to the surrounding environment by convection and radiation, retarding the process. Thermal balance of the heat gains and losses established whether the burning process will be self-sustained, and at what rate propagation will occur.

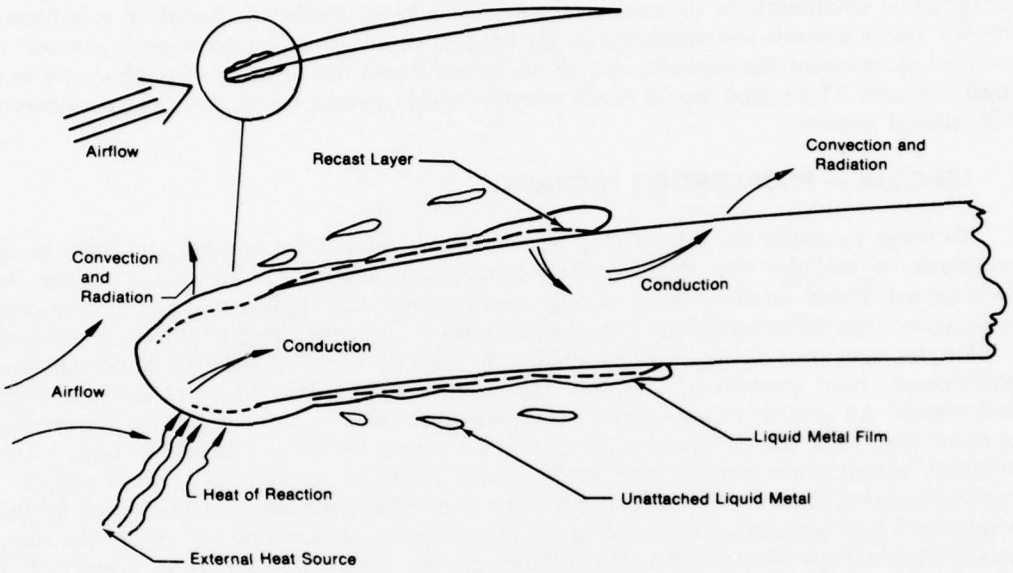

Figure 17. Physical Model of Airfoil Combustion

C. ANALYTICAL APPROACH

The physical model depicted in Figure 17 has been analytically simulated using a combination of lumped mass and differential numerical techniques. A lumped mass representation of a burning airfoil, with the various heat transfer processes indicated is shown in Figure 18. Each lumped mass, or node, represents a finite fraction of the airfoil, and is presumed to be in thermal communication with its surrounding nodes and with the gas flow on the surface. In addition, if liquid metal covers the surface at the node location, the temperature of the liquid is assumed to be independent of the temperature of the nodal mass, but heat can flow between the liquid metal and the nodal mass.

An energy equation can be written for a nodal mass in a generalized form, equating the sum of all sources of heat to the rate of internal energy change. The energy balance takes the form:

$$\frac{dE}{dt} = q_{conduction} + q_{convection} + q_{radiation} - q_{input} - q_{reaction} \quad (1)$$

The rate of internal energy change, dE/dt, refers to the energy of the node, and energy change can be in the form of sensible heating (temperature change) or phase change (melting/solidification). Two different cases are noted: (a) no liquid on the surface, and (b) the surface covered with liquid metal.

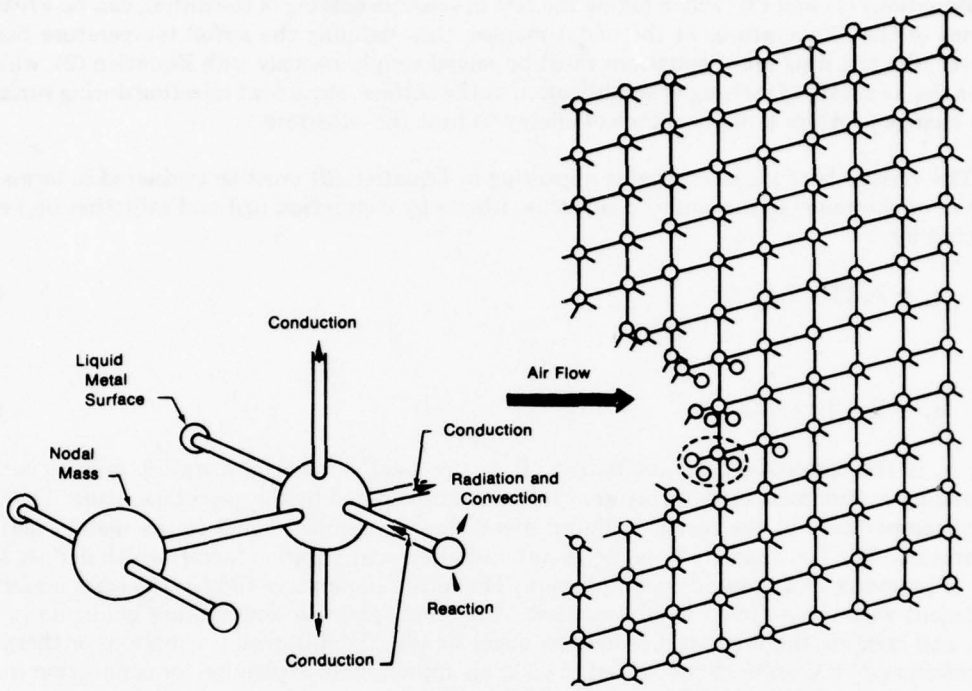

Figure 18. Lumped Mass Thermal Model

For the first case, the nodal mass represents the entire cross-sectional mass of the airfoil. Conduction occurs to neighboring nodes, convection and radiation to the surrounding environment, and heat is supplied to the node by direct external input and by surface reaction. External input may take several forms, such as frictional heat due to rubbing, laser irradiation, or molten metal impingement. External heating is generally considered as an ignition source; although ignition may also be caused by aerodynamic heating, with no other external sources. Surface reaction refers to chemical reactions at any rate, and may range from slow oxidation to very rapid combustion.

For the second case, when liquid covers the surface, Equation (1) is written in two distinct forms, one describing the energy balance at the liquid surface, the other describing the underlying solid substrate. In the liquid layer on the surface, conduction is presumed to only take place between the liquid and the solid substrate. Internal energy change is assumed to be in the form of phase change, and the energy equation takes the form:

$$\rho H_{s\ell} \frac{d\Delta}{dt} = q_{cond,\ surface} + q_{conv} + q_{radiation} - q_{input} - q_{reaction} \tag{2}$$

The thickness, Δ, is considered to define the local airfoil thickness, including addition or losses due to recast solidification or melting of the surface, and $H_{s\ell}$ is the latent heat of fusion of the metal. In the solid substrate, heat flow is limited to thermal conduction between the nodal mass, its surrounding nodes, and the liquid surface. The relevant energy equation takes the form:

$$\frac{dE}{dt} = q_{cond,\ surface} + q_{cond,\ nodes} \tag{3}$$

Equations (1) and (3), which define the rate of sensible heating of the airfoil, can be written in terms of the temperatures of the nodal masses, thus defining the airfoil temperature field. However, the resulting set of equations must be solved simultaneously with Equation (2), which defines the local rate of melting or solidification at the surface, since heat rejection during surface phase change provides a major source of energy to heat the substrate.

The various heat losses and gains appearing in Equation (2) must be evaluated in terms of the local environmental and airfoil conditions. Losses by convection (q_c) and radiation (q_R) are predicted by:

$$q_c = h_c\,(T_l - T_g), \tag{4}$$

and

$$q_r = F_r\sigma(T_l^4 - T_e^4), \tag{5}$$

where h_c is the convective film coefficient, T_l is the local surface temperature and T_e is the surrounding environmental temperature, which is approximated by the gas temperature, T_g. The surface temperature in the region of liquid metal flow is assumed equal to the metal melting temperature, T_m. The quantity F_r is the overall radiation configuration factor, which defines the effect of geometry and properties on radiation. The local temperature field in the solid material is transient with three-dimensional heat flow. Assuming spanwise temperature gradients to be small, and treating the temperature field as quasi-steady, the differential equation for thermal conduction can be simplified and solved to yield an approximate expression for conduction from the surface into the solid (q_k). The resulting heat flow is:

$$q_k = \frac{6k}{\Delta}\,(T_m - T_n), \tag{6}$$

where T_n is the nodal temperature in the underlying solid. combining Equations (2), (4), (5), and (6):

$$\frac{d\Delta}{dt} = \frac{h_c(T_m - T_g) + F_r\sigma\,(T_m^4 - T_g^4) - q_{input} - q_{reaction}}{\rho H_{sf}} + \frac{6k(T_m - T_n)}{\rho H_{sf}\Delta} \tag{7}$$

As molten metal flows over the airfoil surface, heating of the solid material by conduction from the liquid may far exceed the heating rate due to chordwise conduction within the airfoil. The numerical procedure chosen for solution of the airfoil energy equations, Equations (1) and (3), determines the temperature field at discrete times during the process. The surface energy equation, Equation (7), is solved at the end of each time increment. Since the surface phase change process and the substrate temperature field are so strongly interdependent, the alternating (rather than simultaneous) solution of the energy equations results in a substantial error. The problem is alleviated by introducing a subsidiary energy equation for the nodal temperature in the immediate region of the liquid front (downstream edge of the liquid sheet), where the chordwise temperature gradient is most severe, and where the transient temperature rise is most significant. Equating the conduction into the solid to the rate of internal energy change in the node:

$$\rho C_p\Delta\,\frac{dT_n}{dt} = -\frac{6k}{\Delta}\,(T_m - T_n). \tag{8}$$

Equations (7) and (8) are solved simultaneously for Δ and T_n, thus defining surface phase change and the change in nodal temperature in the immediate vicinity of the liquid front; however, since these equations are written with time as the independent variable, an auxiliary equation is required to define the motion of the molten metal and its location on the airfoil. In addition, the convective heat transfer and chemical reaction at the surface must be evaluated prior to solving the energy equations.

D. AERODYNAMIC PROCESSES

Three aerodynamic processes play significant roles in the metal combustion phenomenon, namely convective heat transfer at the surface, fluid shear stresses and drag on the flowing liquid metal, and diffusion of oxygen to the metal surface.

Evaluation of these processes requires an evaluation of the aerodynamic boundary layer on the surface. The approximate methods of Walz and Buri (Reference 6) were chosen to perform this calculation, yielding satisfactorily accurate details of the development of the boundary layer and magnitude of the shear stress acting on the surface. The local convective heat transfer is determined from the calculated shear stress (friction coefficient, C_f) by use of the Karman Boelter-Martinelli analogy. (Reference 7)

$$N_u\theta = \frac{PrRe\theta \sqrt{C_f/2}}{5Pr + 5 \ln (5Pr + 1) + \sqrt{2/C_f} - 14} \tag{9}$$

where $N_u\theta = h\theta/k$, $Re\theta$ is the Reynolds number, Pr is the Prandtl number, and θ is the momentum thickness evaluated in the boundary layer analysis.

Oxygen diffusion through the boundary layer is determined from: (Reference 8)

$$\dot{m}_o = Kxm \left(\frac{\chi_{o.\infty} - \chi_{o.o}}{1 - \chi_{o.o}} \right) \tag{10}$$

where $\dot{m}_o$ is the oxygen mass flux, $\chi_{o.o}$ and $\chi_{o.\infty}$ are the concentrations at the wall and free stream, and Kxm is the mass transfer coefficient for diffusion determined by analogy with the heat transfer from:

$$Kxm = \frac{\rho D_{on}\ Nu\theta}{\theta} \left(\frac{Sc}{Pr} \right)^{1/3} \tag{11}$$

Sc and D_{on} are the Schmidt number and binary diffusion coefficient for oxygen-nitrogen mixtures.

E. REACTION KINETICS

The reaction rate at the metal surface, either as slow oxidation or as rapid combustion, is governed by the rate at which oxygen can flow from the air to the surface and bond with free metal in the substrate. The overall process is governed by the most restrictive step in the foregoing chain of events. The most restrictive step is dependent on the surface temperature, amount of surface oxides, and the nature of the boundary layer mass diffusion process.

The governing process is assumed to be the most restrictive of the following:

1. Oxygen diffusion through the surface oxides at low temperature (parabolic kinetics), dependent on surface temperature and amount of accumulated oxides

2. Linear kinetics at high temperatures, dependent on surface temperature only

3. Oxygen diffusion rate through the aerodynamic boundary layer.

The kinetic models describing these three conditions are:

1. Parabolic (Reference 9)

$$\frac{dM}{dt} = \frac{3.63 \times 10^7 \, e^{-\frac{29540}{T}}}{M} \quad , \; T<1300°K \tag{12}$$

2. Linear (Reference 10)

$$\frac{dM}{dt} = 2.60 \times 10^3 \, e^{-\frac{10065}{T}} \quad , \; T \geq 1300°K \tag{13}$$

3. Oxygen Diffusion in Boundary Layer

$$\frac{dM}{dt} = \dot{m}_o \text{ (Eq 10)}$$

where M = Oxygen bonded on surface, gm/cm²
T = Surface temperature, °K
t = Time, sec.

The corresponding reaction rate at the surface is:

$$q_r = H_{o,o} \frac{dM}{dt} \tag{14}$$

where $H_{o,o}$ is the heat of reaction per mass of oxygen, based on the reaction assumed to occur at a particular condition. Post-test analysis of burned airfoil specimens indicated the primary reaction product resulting from slow oxidation is TiO_2, while rapid combustion results in approximately equal weights of TiO and Ti_3O_5. The corresponding heats of reaction have been incorporated in the model, i.e., TiO_2 is assumed to result from solid surface oxidation, while 50% TiO-Ti_3O_5 is assumed to result when combustion occurs on a molten surface.

F. LIQUID METAL FLOW

Molten metal, driven by aerodynamic forces, is observed to flow over the surface downstream of the airfoil leading edge. A model of this flow was developed, based on the liquid being driven only by aerodynamic shear stress in the boundary layer. Based on the liquid metal viscosity data of Magnitskiy, (Reference 11) several cases were evaluated and compared with the experimental data. Predicted velocities of the liquid front were found to be low by several orders

of magnitude. Re-examination of the high speed movies indicated that the liquid flow is rippled, and fluid motion over the surface is in the form of unsteady waves. The primary driving force for this type of motion is aerodynamic profile drag; much greater than the corresponding shear stress.

A new model is formulated in which liquid moves as waves over the wetted surface, as shown in Figure 19, accumulating at the downstream edge as a liquid front. Motion of this front is controlled by a balance of aerodynamic drag due to the airstream and surface tension forces at the interface between liquid and the solid surface. As the front moves downstream over the nonwetted surface, solidification of part of the liquid film occurs, depending on the relative heat losses by conduction and convection, and the heat gain from reaction. Motion of the liquid front is intermittent, liquid accumulating until aerodynamic forces are sufficient to exceed surface forces, at which time the liquid front moves over the surface. When sufficient mass is solidified to reduce the size of the liquid wave below the critical size, motion of the front ceases. On a time-averaged basis, the motion can be treated as steady, being controlled by the rate of liquid flow rate reaching the front. If the rate of liquid melting at the airfoil leading edge is $\dot{m}_1$, the fraction lost from the leading edge ξ, and the local airfoil thickness is Δ, then the local rate of molten metal flow in the x-direction along the surface is:

$$\dot{m}(x) = (1 - \xi)\,\dot{m}_1 - \int_0^x \rho\,\frac{d\Delta}{dt}\,dx \qquad (15)$$

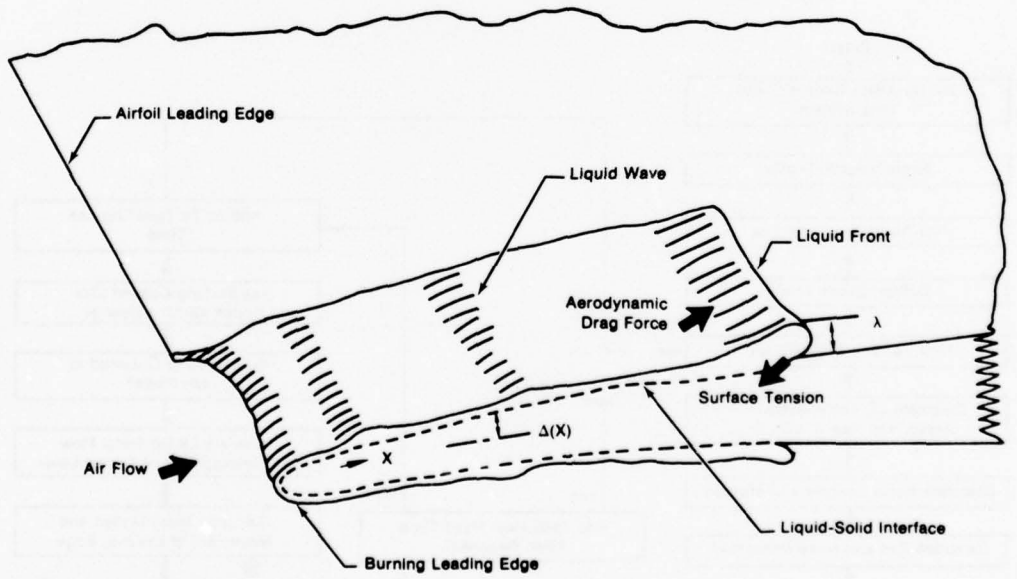

Figure 19. Liquid Flow Model

Equation (15) is an expression of continuity of mass along the surface. At the edge of the liquid front $x = xe$, and the liquid metal flow rate on the surface is $\dot{m}_e$.

Assuming that the liquid front is configured as an elongated droplet, as shown in Figure 19, the aerodynamic force necessary to overcome surface tension force and produce fluid motion is:

$$F_a = \frac{C_D\,\rho_a\,U_\infty^2\,\lambda}{2} = \zeta \qquad (16)$$

where λ is the droplet height, ζ is the component of fluid surface tension, parallel to the solid surface, C_D is the aerodynamic drag coefficient, and ρ_a and U_∞ are the air density and velocity. The motion of the liquid front is related to its thickness and flow rate by:

$$\dot{m}_e = \rho \lambda V \tag{17}$$

Solving Eqs. (15), (16), and (17) for the liquid velocity:

$$V = \frac{(1 - \xi)\,\dot{m}_1 - \int_0^{xe} \rho \frac{d\Delta}{dt}\, dx}{\frac{2\zeta \rho \cos\gamma}{C_D \rho_a U_\infty^2}}, \tag{18}$$

which defines the velocity of liquid advance over the surface.

G. PROGRAM LOGIC

The various analytical models described herein have been incorporated in a computer program, providing an integrated procedure for the prediction of ignition and self-sustained combustion of titanium. The operational logic, outlined in Figure 20, allows prediction of the ignition-combustion sequence for a wide range of ignition sources and environmental conditions.

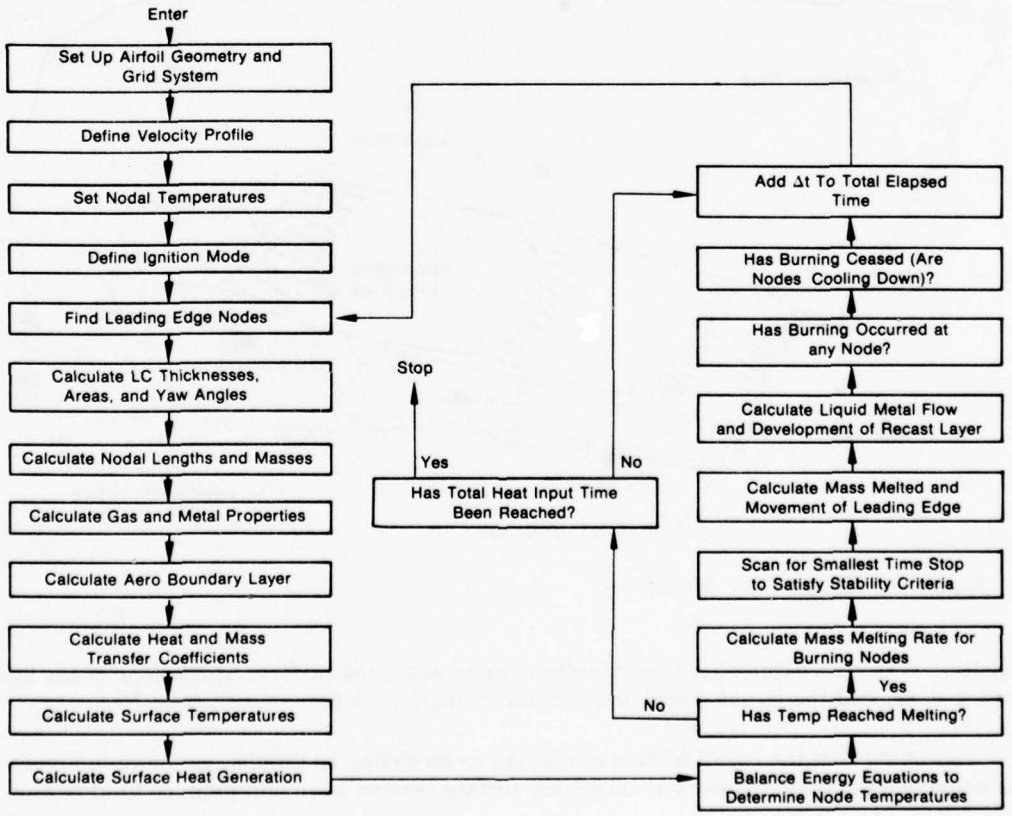

Figure 20. Analytical Model Logic Diagram

For each defined set of environmental and ignition conditions, airfoil geometry and material properties, the program predicts the transient temperature field during the duration of the ignition source. Ignition is presumed to have occurred if the transient response to the ignition source results in a temperature rise to the melting point at some location on the airfoil. Self-sustained combustion is presumed if reaction heat generation is sufficient to sustain melting after the ignition event has terminated. If ignition and self-sustained combustion is found to occur, the program predicts the propagation rate as combustion spreads across the airfoil, until the specimen being analyzed is totally consumed, or extinction of burning occurs.

H. ANALYTICAL RESULTS

Figure 21 shows a comparison of the basic analytical model with the results of a combustion test performed in a complementary program (Contract N62269-76-C-0429). The test specimen was Ti-6Al-4V, and was of the contoured design shown in Figure 6. Although chordwise burning rates are in reasonable agreement, the predicted spanwise propagation rate is much too large. The basic analytical model predicts the rate of surface melting as a function of the relative heat gains and losses at the surface, but does not consider the direction of heat flow at the surface and within the airfoil. Hence, the basic model lacks the capability to predict the direction of leading edge melting, resulting in excessively large predicted rates of spanwise propagation along the thin leading edge. This discrepancy indicates the need for refinement of the model, particularly in the areas of melt flow and leading edge combustion.

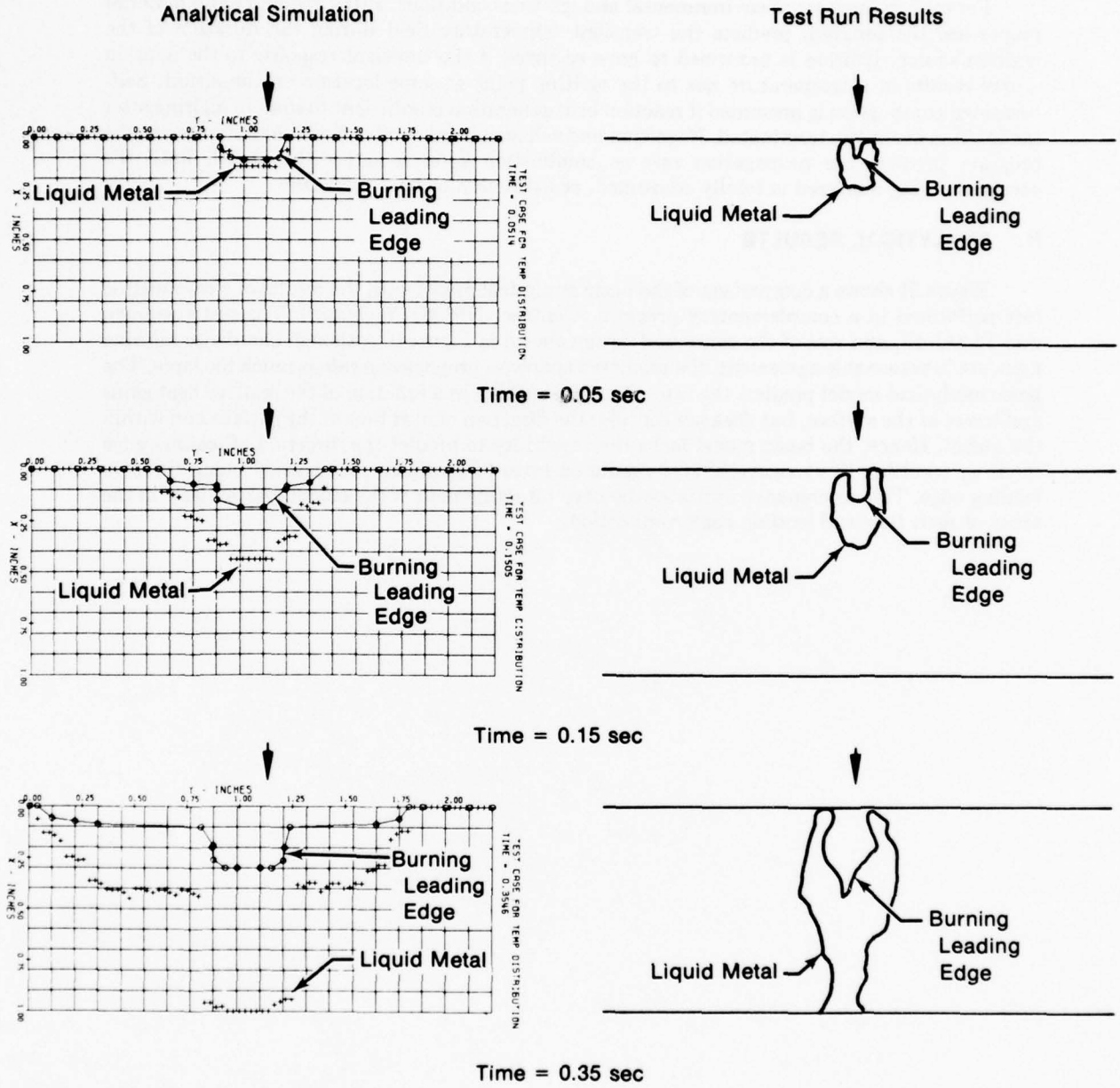

Figure 21. Comparison of Analytical Simulation With Actual Test Results

SECTION V

GENERALIZED ANALYTICAL MODEL

To achieve the needed refinements in the model, the analytical study was extended in duration and scope. To provide a more useful predictive model, several additional goals were added to the program. These goals were: refinement of the liquid flow model, addition of alloy effects, addition of accountability for aerodynamic melt loss from the surface, and expansion of the model to account for centrifugal body forces due to rotation. These goals were achieved in two steps; development of the model refinements for a static airfoil, then the addition to account for rotation. However, since addition of rotational effects required generalization of many different areas of the model, only the final resulting model will be described in this report.

A. DESCRIPTION OF THE MODEL

Comparison of melt flow velocities, evaluated from photographic data, with thermal diffusion rates in the solid airfoil substrate indicated that liquid metal flow is the primary mode of thermal propagation in a burning airfoil. For purposes of comparison, a simplified one-dimensional thermal analysis was conducted, and evaluated over the range of observed test data. In the development of the basic analytical model, rippled melt flow was assumed to occur over the surface, driven by aerodynamic shear, with no consideration of the detailed structure of such flow.

In the generalized model, the detailed structure of the melt flow is examined, and a model developed for simultaneous transport of momentum, heat, and oxygen species from the liquid surface to the liquid-solid interface. The effects of oxides on the relevant physical properties are incorporated in the model, within the limitations of available data. Continuity relations are developed in integral form to allow evaluation of the melt flow processes over the surface of the airfoil, Aerodynamic melt loss considerations are included in the continuity equations, and a suggested loss model is proposed. Finally, the model geometry is expanded to incorporate the effects of centrifugal forces generated by rotation, as in the case of compressor rotors.

All description of the model development will be based on the inclusion of rotation effect. Figure 22 illustrates a typical situation, with burning initiated at the leading edge, and melt flowing in a compound direction toward the trailing edge tip. This figure shows the salient features of the process, with melt streaming from the leading edge of the burning zone to the downstream edge of the melt region, henceforth called the melt leading edge. The leading edge of the burning blade will be called the stagnation region.

B. THERMOPHYSICAL PROPERTIES

The physical properties of titanium relevant to the overall combustion model include the thermodynamic properties, defining the state and internal energy, and the transport properties, defining the rate of the various transport processes. These properties in general are dependent on the metal temperature, alloying elements and amount of oxygen present, and the crystalline structure. Because of insufficient data, the present analysis has not included alloying effects, but has as far as possible included the effect of temperature, phase, and oxygen content. The effect of temperature and oxygen content are considered in evaluating the melt viscosity and thermodynamic state, and the effect of temperature is considered on the thermal conductivity and oxygen diffusivity.

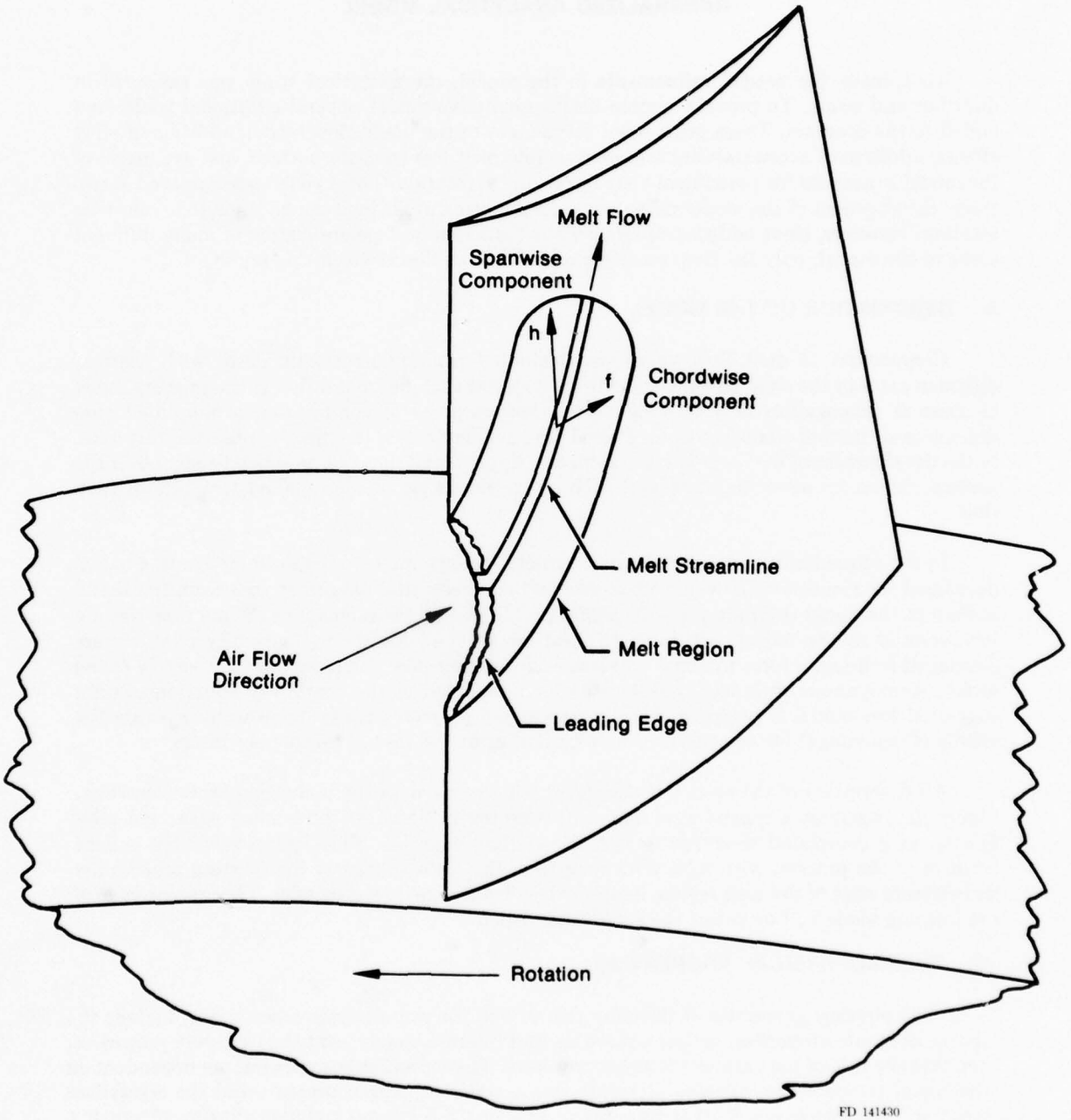

Figure 22. Generalized Configuration — Burning Blade

Figure 23 shows a phase diagram for the titanium-oxygen system, developed by Schofield and Bacon (Reference 12). Oxygen in titanium is seen to act as a phase stabilizer resulting in the occurrence of α-Ti at temperatures above the normal α-β transition, and increasing the liquidus temperature significantly. It is further noted that the presence of dissolved oxygen causes the occurrence of a solidus-liquidus temperature range, or two-phase region, at low concentrations.

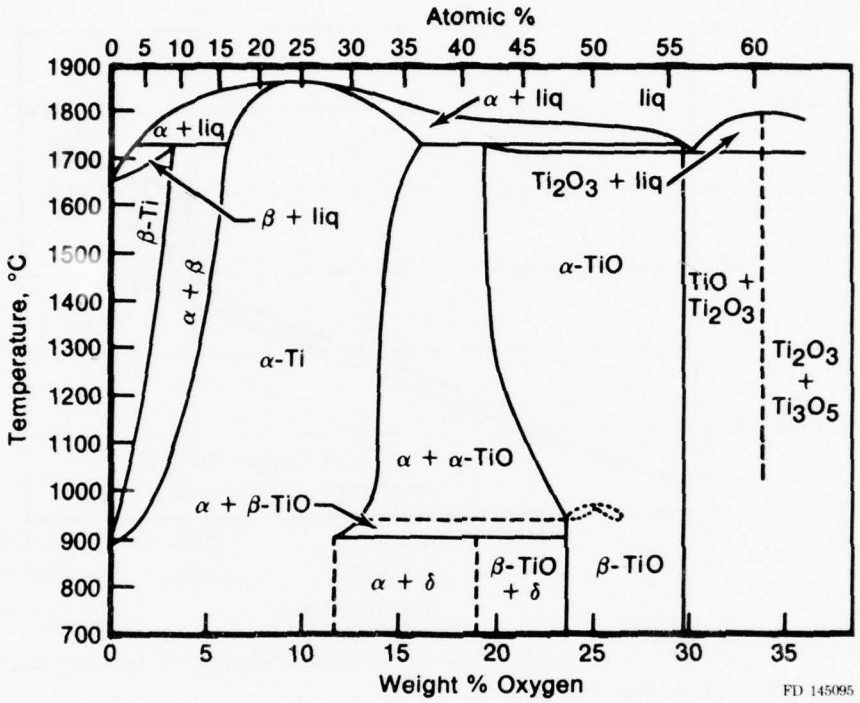

Figure 23. The Ti-O Phase Diagram up to 35 wt % Oxygen After Schofield and Bacon

A corresponding thermodynamic phase diagram was constructed, based on thermodynamic data for pure titanium (Reference 13).

The presence of oxygen was assumed to act only as a phase-stabilizer causing the effect of the energy of α-β transition to be shifted to the melting temperature range. While the resulting enthalpy diagram, shown in figure 24, may not be entirely correct, it provides a workable basis for modeling the heat transfer through the melt flow.

The nature of the two-phase melting region, shown in Figure 23, was assumed to affect the viscosity of the melting metal, particularly near the solid-liquid interface. The data of Magnitskiy (Reference 11) for liquid titanium showed the viscosity to vary inversely with temperature. To extend this data into the two-phase region, a hyperbolic variation of viscosity was assumed of the form

$$\nu\,(T, \phi) = \nu_m \left[\frac{T_l - T_s}{T - T_s} \right], \; T_s < T < T_l \tag{19}$$

where T_s and T_l are the solidus and liquidus temperatures at the local oxygen concentration (ϕ), and ν_m is the kinematic viscosity at T_l. For temperatures at or above the liquidus, the data of Reference 11 is considered valid.

Data was not available on the effect of oxygen on the other transport properties in the liquid state, nor for that matter for pure titanium in the liquid state. The data of Roe, Palmer, and Opie (Reference 14) for oxygen diffusivity in titanium was extrapolated to the melting temperature, and treated as temperature dependent only. The data of Touloukian (Reference 15) for thermal conductivity was treated in the same manner.

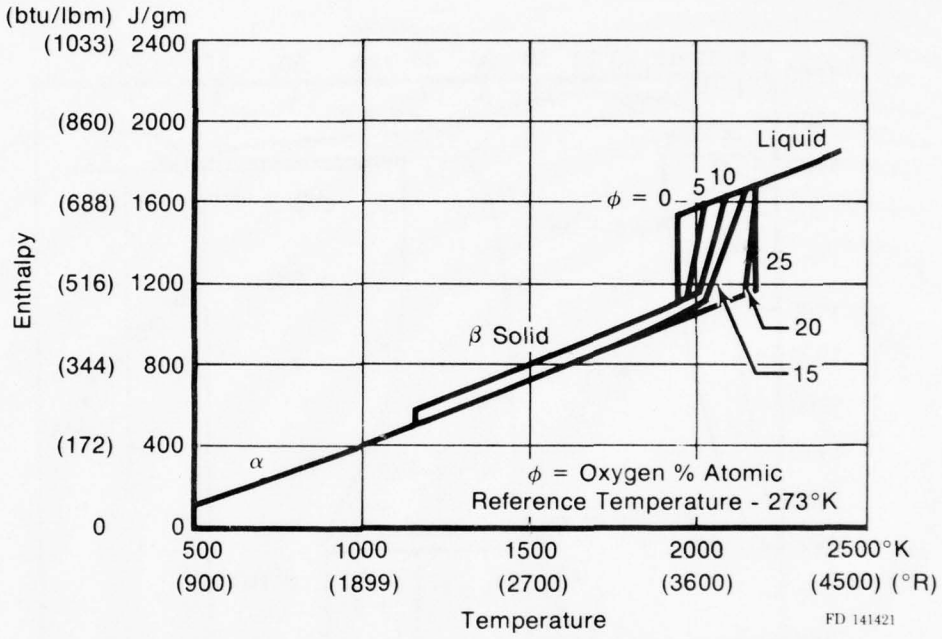

Figure 24. Enthalpy of Titanium-Oxygen System as Function of Temperature

C. STRUCTURE OF THE MELT FLOW

In the flowing melt region a liquid layer of thickness δ is assumed to flow on the surface, driven by aerodynamic forces in the direction of air flow, and by centrifugal forces in the radial outward direction. Oxygen flows in the aerodynamic boundary layer to the liquid surface, reacts with the melt, and the resulting heat and oxides diffuse into the melt layer. Shear stress across the melt is assumed constant, and momentum transport is considered small by comparison. Figure 25 illustrates the features of the flowing liquid layer. The coordinates (x, y, z) are in the chordwise, normal, and spanwise directions, respectively. The velocity components (u, v) represent the local liquid velocity in the two surface directions and are seen to vary with distance from the surface. The temperature and oxygen concentration at the outer surface are Ti and ϕ_1, and at the inner surface are T_0 and ϕ_0. If the outer temperature exceeds the liquidus (superheated liquid), the saturated liquid state is assumed to occur at a distance δ_1, from the solid interface, with corresponding temperature and concentration. Oxygen flows into the melt layer at a rate $\dot{m}_o$, and the liquid-solid interface recedes or advances (melting or solidification) at a velocity U. If melting occurs at a single temperature, as in the case of pure oxygen-free titanium, it is assumed to occur at the liquid-solid interface with a corresponding discontinuity in the local enthalpy (latent heat of fusion). However, if a two-phase melting zone exists (solidus and liquidus not equal), the enthalpy is assumed to increase linearly from the solid to the liquid state over the depth of the melting zone.

The nature of the melt surface is still assumed to be ripply, the amplitude and wavelength of the surface waves dependent on the aerodynamic shear and the melt thickness. For very high shear loading, waves will crest and be stripped from the surface, creating spark showers as observed in the tests.

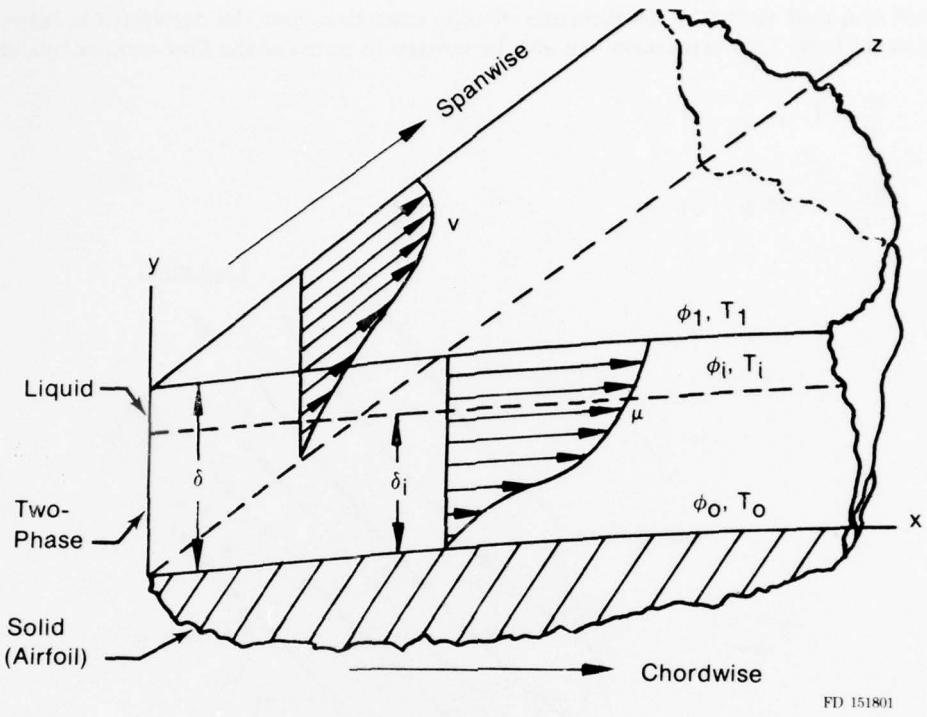

Figure 25. Local Velocity Profiles and Nomenclature Used in Melt Flow Analysis

D. INTEGRAL TRANSPORT EQUATIONS

In Figure 22 the melt region is illustrated with a single streamline. The melt flow field can be considered as composed of a set of streamlines originating in the stagnation region and ending at the downstream edge of the melt region, as shown in Figure 26. If a coordinate system is described by (S, J), where S is the distance along the streamline and J is the streamline number, analysis of the melt flow can be performed along each streamline. Let the liquid flow rate in a streamline at a point (S, J) be $p\bar{F}$, then $\bar{F}$ is a vector quantity aligned in the direction of the streamline. The flow vector $\bar{F}$ can be described as composed of components (f) in the chordwise and (h) in the spanwise directions. Thus,

$$\bar{F} = \bar{i}f + \bar{j}h \tag{20}$$

where $\hat{i}$ and $\hat{j}$ are unit vectors in the component directions. The direction of the streamline can be described by the angle (ψ) with the chord, where

$$\tan \psi = f/h \tag{21}$$

The melting airfoil adds to the streamline flow in the amount ρU per unit length of streamline. If the fraction of flow rate lost to the airstream is ξ per unit length, then the rate of change of flow in the streamline is

$$\frac{d\bar{F}}{ds} = \bar{s}U - \xi\bar{F} \tag{22}$$

where $\bar{s}$ is a unit vector in the direction of the streamline, and the derivative is taken in the direction of flow. This expression can also be written in terms of the flow components as:

$$\frac{df}{ds} = U \cos \psi - \xi f \tag{23a}$$

$$\frac{dh}{ds} = U \sin \psi - \xi h \tag{23b}$$

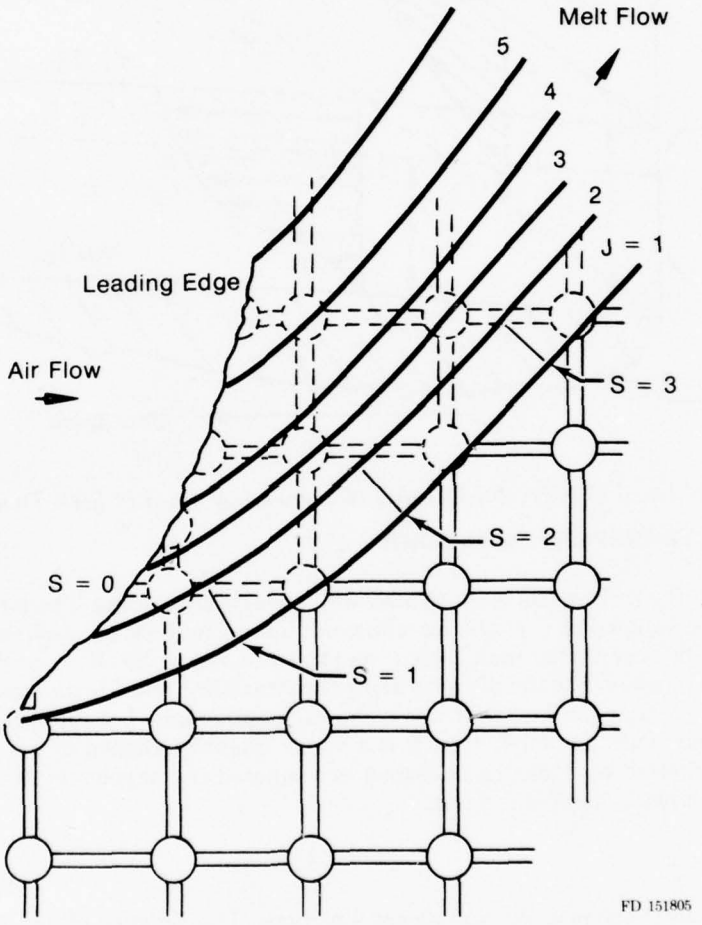

Figure 26. Streamline Indexing System

In a similiar fashion, the flow rate of oxygen carried along the surface by the melt is (g), and is related to the melt flow by

$$g = \rho F \bar{\phi} \tag{24}$$

where

$$F = \sqrt{f^2 + h^2} \ ,$$

and $\bar{\phi}$ is the local bulk concentration of oxygen in the melt.

The rate of change of g along the surface is given by:

$$\frac{dg}{ds} = \dot{m}_o - \xi\phi_1 \rho F \tag{25}$$

The concentration at the liquid surface (ϕ_1) is presumed to describe the average concentration of the melt loss at the surface.

The set of equations (23a, b) and (25), describe the change in liquid mass flow and oxygen content of the streamlines as they flow over the surface.

E. LOCAL TRANSPORT PROCESSES

Integration of the integral transport equations requires evaluation of the initial conditions, i.e., values of (f, h, g) at the stagnation point. In addition, these transport functions must be related to the local transport processes to allow evaluation of the physical variables, such as local velocity, temperature, and concentration.

1. Axial (Chordwise) Velocity Profile

The melt flow was assumed to be laminar, with constant shear stress, and with no slip at the liquid-solid interface. Assuming the velocity profile to be represented by a second degree equation:

$$u = a + b\eta + c\eta^2 \tag{26}$$

where

$$\eta = y/\delta.$$

The shear stress τ, must be equal to the aerodynamic shear, determined from boundary layer analysis, and is related to the velocity profile by:

$$\tau = \frac{\rho\nu_1}{\delta}\frac{du}{dy}\Bigg|_{y=\delta} = \frac{\rho\nu_o}{\delta}\frac{du}{dy}\Bigg|_{y=o} \tag{27}$$

where subscripts '1' and 'o' refer to evaluation at conditions at the liquid and solid surfaces. With the no-slip conditions (u = o, y = o) and Equation (27), the constants in Equation (26) can be determined, yielding the velocity equation:

$$u(\eta) = \frac{\tau\delta\eta^2}{2\mu_1} \tag{28}$$

The axial component of flow in the streamline (per unit width) is:

$$\rho f = \int_o^\delta \rho u dy = \delta \int_o^1 \frac{\rho\tau\delta\eta^2}{2\mu_1}\, d\eta \tag{29}$$

Hence,

$$f = \frac{\tau\delta^2}{6\mu_1} \tag{30}$$

2. Radial Velocity Component

Fluid motion in the radial direction is driven by centrifugal body force (β), and resisted by aerodynamic shear stress (τ_o) due to the motion of the liquid relative to the air stream. A simple analysis, balancing radial forces, shows that the shear stress generated by body forces varies linearly from the liquid surface to a maximum at the solid surface. The aerodynamic shear stress is found to be constant across the melt. The total stress is:

$$\tau = \beta\delta\ (1-\eta) - \tau_o \tag{31}$$

where

$$\beta = \rho\bar{R}\omega^2 \qquad \text{and} \qquad \tau_o = C_f\ \frac{\rho_a v_1^2}{2} \tag{32}$$

The centrifugal force depends on the radius to the blade mid-span ($\bar{R}$) and the rotational speed (ω) of the compressor stage. The aerodynamic shear stress, is a function of the local friction coefficient (C_f) and the relative liquid velocity at the air-liquid interface (v_1). Approximating the variation of viscosity in the melt by

$$\mu = \frac{\mu_1}{\eta}, \tag{33}$$

the laminar relation between shear stress and velocity gradient is combined with Equation (31) and integrated to yield the velocity profile:

$$v(\eta) = \frac{\beta\delta^2}{\mu_1}\left(\frac{\eta^2}{2} - \frac{\eta^3}{3}\right) - \frac{\tau_o\ \delta\eta^2}{2\mu_1} \tag{34}$$

the surface velocity (v_1) is determined by combining Equations (32) and (34), for $\eta = 1$, yielding:

$$v_1 = \frac{-1 + \sqrt{1 + \frac{\rho\beta C_f\delta^3}{6\mu_1^2}}}{\left(\frac{\rho C_f\delta}{2\mu_1}\right)} \tag{35}$$

The radial flow component is now calculated in the same manner as the axial component, resulting in the relation:

$$h = \frac{\beta\delta^3}{12\mu_1} - \frac{\tau_o\ \delta^2}{6\mu_1} \tag{36}$$

3. Oxygen Concentration Profile

The distribution of oxygen mass fraction (ϕ) is assumed of the same form as the velocity profile, i.e., second order power function of the distance from the solid surface:

$$\phi(\eta) = a + b\ \eta + c\ \eta^2$$

The coefficients are evaluated by satisfying the following conditions at the solid and liquid surfaces:

a. Flow rate of oxygen into the liquid surface is equal to the diffusion rate into the melt.

b. Diffusion rates in the liquid and solid phases are equal at the solid-liquid interface.

c. The concentrations in the liquid and solid are equal at the interface.

The oxygen diffusion rate into the solid is evaluated by solving the transient diffusion (Laplace) equations for the case of a moving boundary. Two dimensionless groups appear in the solution, the mass transfer Peclet number (Λ), relating the mass transport by convection and diffusion, and the transport ratio (Γ), a form of mass transfer Reynolds number. These quantities are defined by:

$$\Lambda = \frac{\delta\, U}{D_0} \quad \text{and} \quad \Gamma = \frac{\delta\, \dot{m}_0}{\rho D_1} \tag{37}$$

where D_0 and D_1 are the oxygen diffusivities in titanium at the temperatures T_0 and T_1.

The resulting concentration profile must be related to a reference value. Relating to the liquid surface:

$$\phi(\eta) = \left(\frac{\phi_1 - \frac{\Gamma}{2}}{1 + \frac{\Lambda}{2}} \right) \left(1 + \Lambda\eta - \frac{\Lambda}{2}\,\eta^2 \right) + \frac{\Gamma}{2}\eta^2$$

The bulk concentration, ($\bar{\phi}$), is obtained by integration of the product of the velocity and concentration profiles:

$$\bar{\phi} = \frac{\int_0^1 \phi \nabla d\eta}{\int_0^1 \nabla d\eta} \tag{39}$$

where ∇ is the liquid velocity vector. Combining Equations (28), (34), and (38), and performing the integration indicated in (39) yields a relationship between the bulk and liquid surface concentrations ($\bar{\phi}$, ϕ_1). The surface concentration is the positive root of the following quadratic equation:

$$F_1\phi_1^2 + [(2+\Lambda)\,F_2 - \Gamma\,F_1]\,\phi_1 + \left[\left(1 + \frac{\Lambda}{2} \right)^2 (F_2 - \bar{\phi}^2) + \frac{\Gamma^2}{4}\,F_1 - \left(1 + \frac{\Lambda}{2} \right) \Gamma\,F_2 \right] = 0 \tag{40}$$

Where:

$$F_1 = \left(1 + \frac{9\Lambda}{20}\right)^2 + \frac{\left[B\left(\frac{1}{2} + \frac{13\Lambda}{60}\right) - \Pi\left(1 + \frac{9\Lambda}{20}\right)\right]^2}{\left(\frac{B}{2} - \Pi\right)^2}$$

$$F_2 = \frac{3\Gamma}{10}\left(1 + \frac{9\Lambda}{20}\right) + \frac{\left[B\left(\frac{1}{2} + \frac{13\Lambda}{60}\right) - \Pi\left(1 + \frac{9\Lambda}{20}\right)\right]\left(\frac{2B}{15} - \frac{3\Pi}{10}\right)\Gamma}{\left(\frac{B}{2} - \Pi\right)^2}$$

$$F_3 = \frac{9\Gamma^2}{100} + \frac{\left(\frac{2B}{15} - \frac{3\Pi}{10}\right)^2\Gamma^2}{\left(\frac{B}{2} - \Pi\right)^2}$$

$$B \equiv \frac{\rho\delta\bar{R}\omega^2}{\tau}, \quad \Pi \equiv \frac{v_i^2}{U_\infty^2}$$

The concentration at the solid interface (η=0) is readily determined from Equation (38) as:

$$\phi_o = \left(\frac{\phi_1 - \frac{\Gamma}{2}}{1 + \frac{\Lambda}{2}}\right) \tag{41}$$

4. Local Heat Transfer

Heat transfer into the flowing melt consists of the sum of several components, heat generation due to chemical reaction at the surface, discrete surface heat input (i.e., laser radiation), and convective and radiant exchange with the surrounding environment. The components for reaction, convection, and radiation are described by Equations (14), (4), and (5). Figure 27 shows a typical line of state points (dashed curve) across a layer of melt. Points "0" and "1" correspond to the solid interface and outer surface, and point "i" is the location of the saturated liquid state. The corresponding distribution of thermodynamic states is shown in Figure 28. The physical correspondence of these state points is shown in Figure 25. In the region $0 < y < \delta_i$, melting is occurring and enthalpy is assumed to vary linearly with distance from the solid-liquid interface. Thus,

$$\frac{H - Ho}{H_i - Ho} = \frac{y}{\delta_i} \tag{42}$$

In the region between points "i" and "1," melt is superheated liquid. Heat flow is assumed to be constant in this region, thus the net heat input at the outer surface is equal to the heat flow across the surface "i." The heat flow in the melting region is related to the temperature field by

$$k\frac{d^2T}{dy^2} = \rho U\frac{dH}{dy}, \tag{43}$$

which describes one-dimensional conduction with a moving boundary. This assumes that conduction normal to the solid surface is the only significant heat flow in the melt. A relationship

was described in Equation (7) between melting rate and net heat flow rate in the melt. This relationship can be written in a generalized vector form as:

$$\rho \, H_{sl} \, \vec{U} = \vec{q}_s - \vec{q}_k, \tag{44}$$

where:

$\vec{q}_s$ = net surface heat flux normal to surface
$\vec{q}_k$ = conduction heat flux into solid substrate.

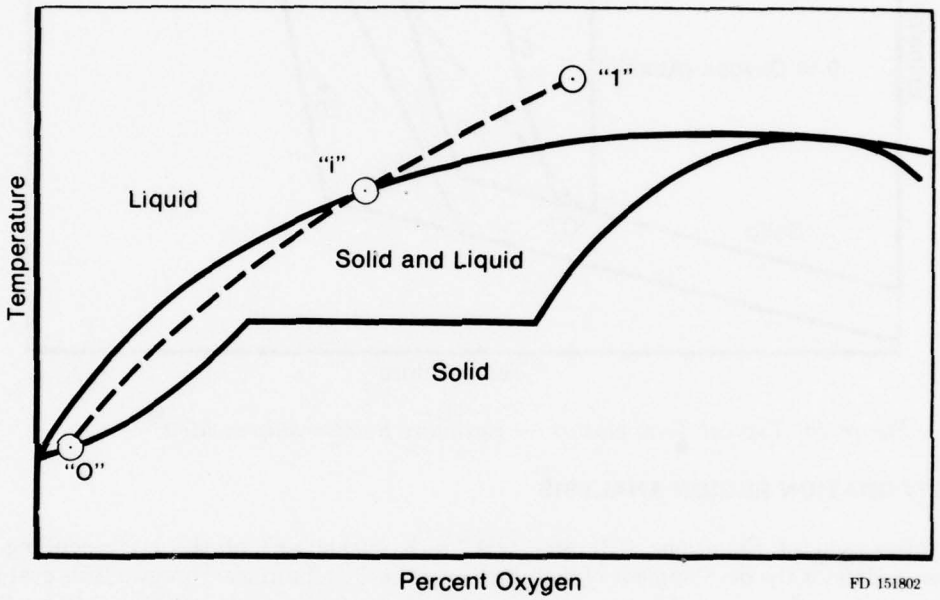

Figure 27. Typical Temperature — Concentration Relationship in Melt

For melting with an imposed concentration profile, the latent heat of fusion becomes

$$H_{sl} = Hi - Ho \tag{45}$$

Integration of Equation (43), in combination with Equations (42), (44), and (45) yields a relationship between the temperatures T_1 and T_o. For the case with superheat:

$$T_1 = T_o + \frac{q_s}{k}\left(\delta - \frac{\delta_1}{2}\right) - \frac{q_k \, \delta_1}{2k} \tag{46}$$

For melting without superheat, Equation (46) still applies with $\delta_1 = \delta$. The solid interfacial temperature T_o correspond to the solidus temperature at the oxygen content of the interface. Because the surface heat flux (q_s) is a function of the surface temperature, evaluation of Equation (46) is an iterative procedure. Details of the solution are shown in the User's Manual.

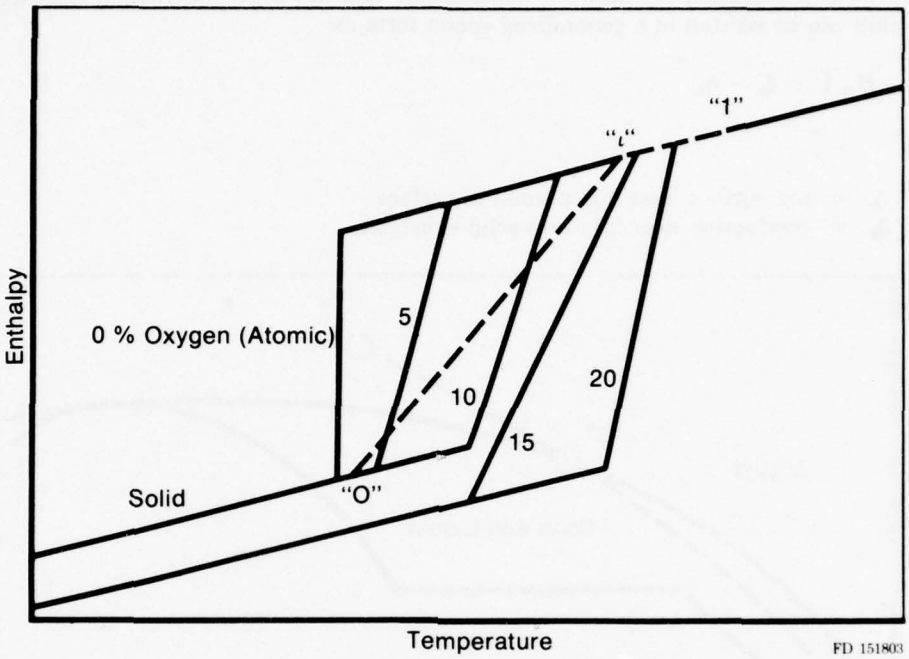

Figure 28. Typical Temperature — Enthalpy Relationship in Melt

F. STAGNATION REGION ANALYSIS

Integration of Equations (23) and (25), with evaluations of the corresponding local processes, defines the development of melt flow over the airfoil surface. However, this evaluation requires that conditions at the stagnation point be known to provide initial conditions for the integration. Specifically, three quantities are required to start the calculation, the melt thickness (δ), the bulk concentration ($\bar{\phi}$), and the melting velocity at the leading edge (U). Figure 29 shows a cross-sectional view of the leading edge with the relevant features.

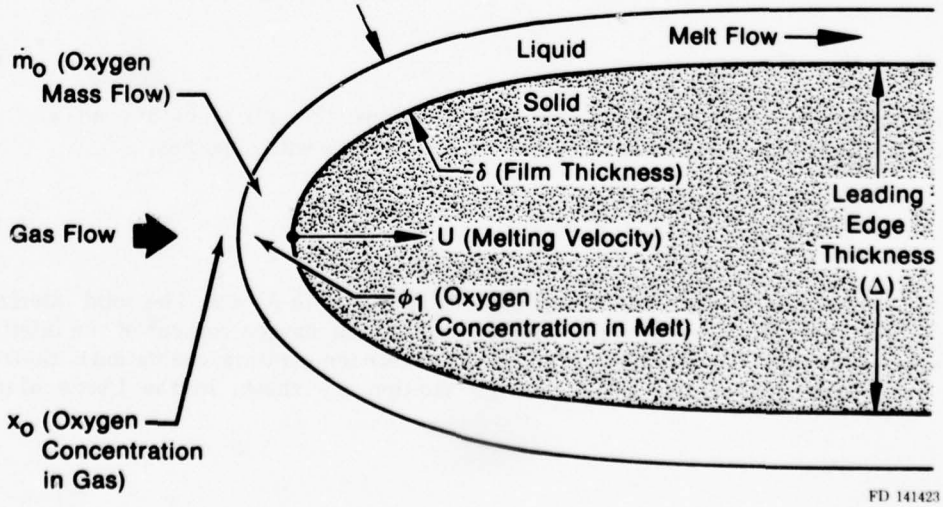

Figure 29. Stagnation Point Region of Burning Airfoil

Based on post-test examination of burned specimens, the cross-sectional shape of a melting leading edge will be considered an elliptic cylinder with an aspect ratio (R = width/length).

The initial concentration is determined by expanding Equation (25), taking the limit as s→o, and noting that the aerodynamic shear stress vanishes at the stagnation point. This results in an expression for the bulk stagnation concentration:

$$\bar{\phi} = \frac{\dot{m}_o}{\rho U} \tag{47}$$

Consider the starting point for streamline (J=1) in Figure 26, noting that the leading edge is yawed to the direction of airflow. Figure 30 shows a larger planform view of the leading edge and the relative directions of the various heat fluxes and the melting velocity.

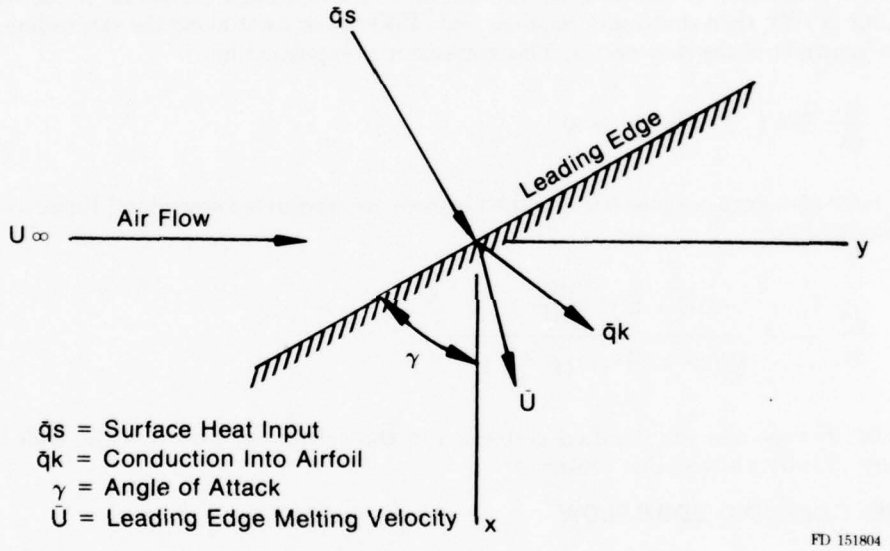

Figure 30. Heat Flow and Velocity Relationship at Burning Leading Edge

The leading edge is at a yaw angle (γ) to the airstream. The surface heat flux ($\bar{q}s$) is normal to the leading edge, and the internal conduction flux ($\bar{q}_k$) points in the direction of maximum temperature gradient in the solid. The magnitude and direction of the melting velocity is determined by the vector addition defined in Equation (44). It is worthy of note that the melting velocity at the leading edge lies in the plane of the airfoil leading edge at an angle defined by the heat transfer. Over the remainder of the airfoil surface the melting velocity vector is oriented normal to the airfoil surface, since the surface and internal fluxes are aligned everywhere except at the leading edge. It is the effect of the internal conduction term in Equation (44) that controls the relative burning rates in the chordwise and spanwise directions, observed in the combustion tests.

The initial melt thickness is found by taking Equations (23a, b) to the limit at the stagnation point. Writing these equations in terms of components normal to the leading edge, and considering the variation of aerodynamic shear stress and centrifugal force as the stagnation point

is approached, an expression is derived relating initial melt thickness to the other parameters at the leading edge. The resulting equation in (δ) is:

$$\frac{\delta^3 \beta \sin \gamma}{R\Delta} + \delta^2 \rho_a U^2_\infty \frac{d C_{fn}}{dn} \cos^2 \gamma = 12 \mu_l U \tag{48}$$

where β is defined by Equation (32), R and Δ are the leading edge aspect ratio and thickness. The derivative of the friction coefficient is evaluated at the stagnation point and is found to be a function of R, Δ, and the leading edge Reynolds number.

G. STREAMLINE CONTINUITY

Independent analysis of flow in adjacent streamlines does not implicitly avoid continuity conflicts, such as intersection of streamlines. To ensure that continuity is satisfied, a condition of streamwise continuity is imposed on the solutions for streamline thickness. If the width of a streamline is (W), then continuity requires that (FW) be constant along the streamline, where F is the magnitude of the flow vector. This statement is expressed by:

$$\frac{d}{ds} W^2 \left(f^2 + h^2 \right) = 0 \tag{49}$$

If local rates of change of shear stress and body force are considered secondary, Equation (49) can be expanded into:

$$\frac{d\delta}{ds} = - \frac{\delta(f^2 + h^2) \frac{dW}{ds}}{W(2f^2 + 3h^2 + hf \frac{\tau_o}{\tau})} \tag{50}$$

This relation expresses the required correction in the calculated growth of the melt thickness necessary to satisfy streamline continuity.

H. MELT LEADING EDGE FLOW

Figure 19 illustrated the main features of the liquid flow model developed as part of the basic analytical model. Modeling of the melt leading edge flow was based on a balance of aerodynamic drag forces and surface tension between the melt and the solid wall.

In generalizing the model, the flow becomes two-dimensional and the model must consider both aerodynamic and body forces. Figure 31 shows the melt leading edge region isolated as a free-body. The sum of forces acting on the fluid must be zero for steady motion. These forces include the aerodynamic drag force (F_D), the component of surface tension parallel to the solid surface (ζ), and the internal forces due to momentum change in the liquid as its velocity is reduced within the leading edge region (F_{int}). If the liquid velocity is V_l as it approaches the leading edge zone, and the edge moves at an average velocity V_e, the internal force is equal to the liquid momentum change, or:

$$F_{int} = \dot{m} (V_l - V_e) = \rho \delta V_l (V_l - V_e). \tag{51}$$

Considering continuity of flow

$$\rho \delta V_l = \rho \lambda V_e = \rho F \tag{52}$$

where F is the magnitude of the flow vector defined in Equation (20). Combining these expressions,

$$F_{int} = \frac{\rho F^2}{\lambda}\left(\frac{\lambda}{\delta} - 1\right) \tag{53}$$

The aerodynamic drag is

$$F_D = C_D \frac{\rho_a U^2_\infty}{2} \lambda \cos^2 \psi \tag{54}$$

Summation of forces yields the relation

$$\frac{C_D \rho_a U^2_\infty}{2} \lambda \cos^2 \psi + \frac{\rho F^2}{\lambda}\left(\frac{\lambda}{\delta} - 1\right) - \zeta = 0 \tag{55}$$

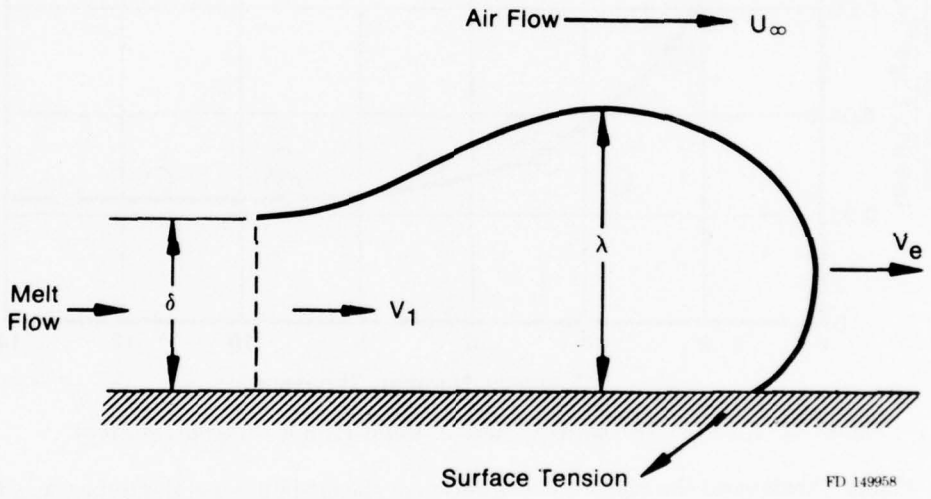

Figure 31. Leading Edge of Melt

This is solved for the leading edge thickness, λ, which is then combined with Equation (52) to yield V_e, the velocity at which melted titanium spreads over the airfoil in the direction of the streamlines. In Equation (55), the flow vector is evaluated at the end of the streamline. Because the end of the streamline is advancing with time, F is changing slightly during the evaluation of the melt motion. The analysis nas been refined to account for this effect, and the procedure is outlined in detail in the User's Manual.

I. STAGNATION POINT DATA

The stagnation region analysis of the generalized model has been used to evaluate selected leading edge melting rate data measured in the test program. In the test data the environmental conditions, the initial geometry, and the leading edge melting velocity were known or measured directly. The instantaneous leading edge geometry was estimated from the photographic data and specimen geometry. The leading edge aspect ratio (R) was assumed to be 0.5 for this analysis, which appeared to result in reasonable data consistency. The analysis yielded the melt thickness at the leading edge, the melt surface oxygen concentration (ϕ_1), and the oxygen diffusion rate into the melt. For comparison, the oxygen diffusion model for the aerodynamic boundary layer,

Equations (10) and (11), where used to predict the oxygen concentration (mol-fraction) in the air at the melt surface.

Figure 32 shows the predicted melt thickness, dimensionalized with leading edge thickness and correlated with leading edge aerodynamic Reynolds number. Reynolds number is a measure of surface shear stress, which governs the thickness of melt accumulation. As airstream Reynolds number increases, the "scrubbing" of the surface reduces melt thickness, apparently reaching an asymptotic limit.

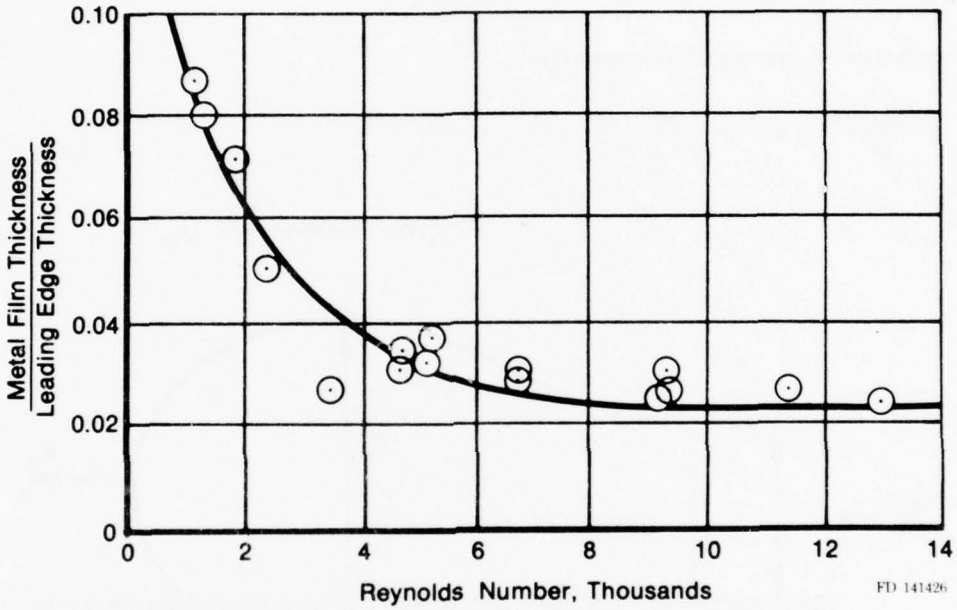

Figure 32. Relative Thickness of Liquid Metal Film at Stagnation Point

Figure 33 compares the oxygen concentration at the air-liquid metal interface as a function of Peclet number (Λ), a measure of the relative magnitudes of melting rate and diffusion rate. The oxygen concentration in the metal is seen to be relatively independent of melting rate, whereas the concentration in the air boundary layer is strongly affected, being strongly depressed with increased flow rate into the melt. The data indicates that the surface oxidation rate is controlled by diffusion in the melt at low melting rates ($\Lambda < 15$), and by diffusion in the aerodynamic boundary layer at higher melting rates. This requires that the analytical model consider both mechanisms, and select the controlling model for evaluation of oxygen flow into the reaction.

Figure 34 shows a correlation of the predicted oxygen flow in the melt as a function of the system dynamics. Oxygen flow is correlated by the Stanton number (St), defined by:

$$St = \frac{\dot{m}_o}{\rho U (\phi_1 - \bar{\phi})} , \tag{56}$$

where oxygen flow, melting velocity, and the oxygen concentrations are all evaluated at the stagnation point. The data shown in the figure is well represented by the empirical correlation:

$$St = 7.17 \Lambda^{-0.8} + 0.00673\Lambda \tag{57}$$

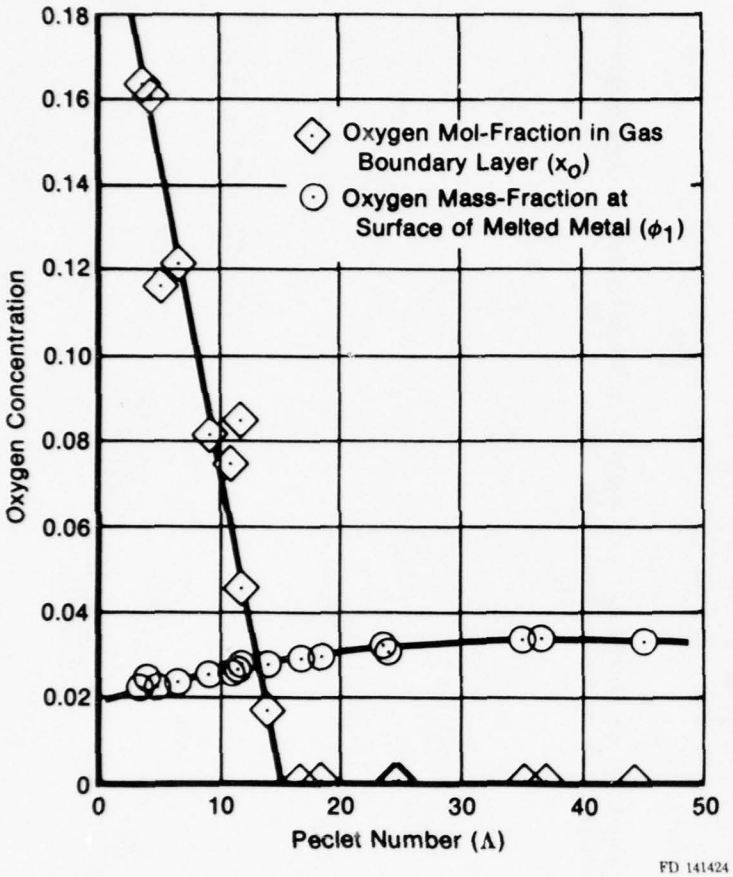

Figure 33. Comparison of Oxygen Concentration in Gas and in Metal at Gas-Metal Interface

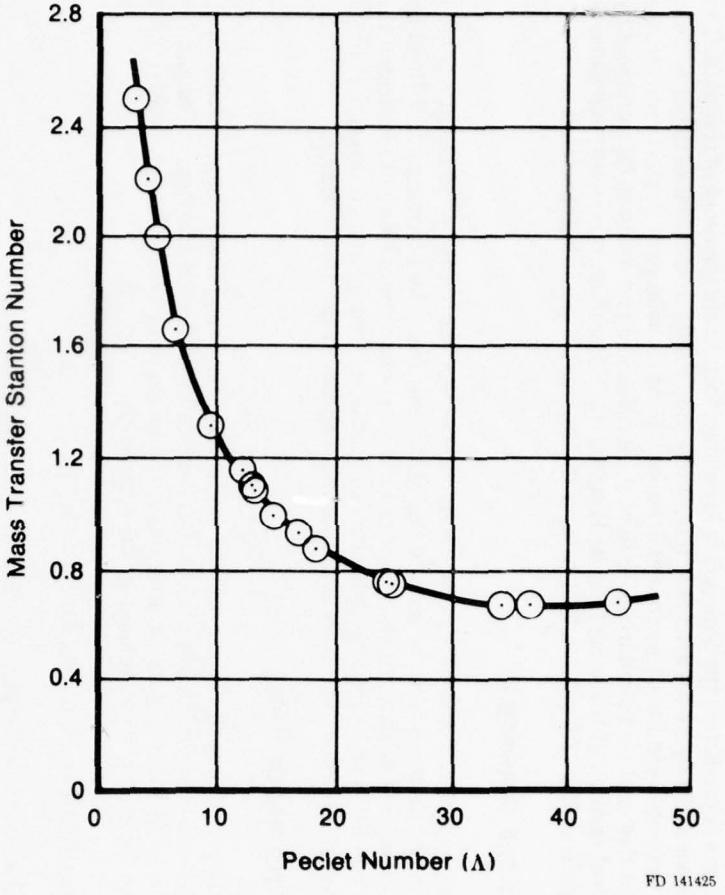

Figure 34. Mass Transfer Stanton Number Predicted by Metal Diffusion Model

Although the curve is predicted, the data points are shown to indicate the range of test data. The relationship shown in the figure between Stanton number and Peclet number takes the same form as the data in the published literature for heat transfer. Heat transfer data in the literature, for stagnation point flow and for boundary layer flow, were examined and found to be correlated by a single empirical relation of the same form as Equation (57). Based on this result, extension of the range of applicability of Equation (57) beyond the stagnation point is considered justified.

J. AIRFOIL HEAT TRANSFER

The energy equation, Equation (1), for conduction of heat within the solid airfoil has been re-written in finite difference form to include the heat input from the flowing melt, defined by Equation (6). A stability analysis to determine criteria for computational stability indicated the most stringent condition to be imposed when the surface is covered by molten metal. Details of the finite difference equations and stability criteria are shown in the User's Manual.

K. COMPUTING PROCEDURES

Computing procedures in the generalized model have been modified somewhat from those outlined in the basic model. Procedural details are shown in the User's Manual, but an outline of the logic flow is shown in Figure 35. In general, the program proceeds through several main functional areas for each time increment in the simulation.

These function areas are as follows:

1. *Evaluation of temperature field in solid airfoil,*
2. test for occurrence of ignition,
3. analysis of flowing melt processes,
4. evaluation of spread of melt-covered region,
5. evaluation of change in airfoil geometry due to melting, and
6. return to (1).

Figure 35 shows the operational flow and required conditional transfers. Logic diagrams for the various operational blocks are expanded in Ref. 16.

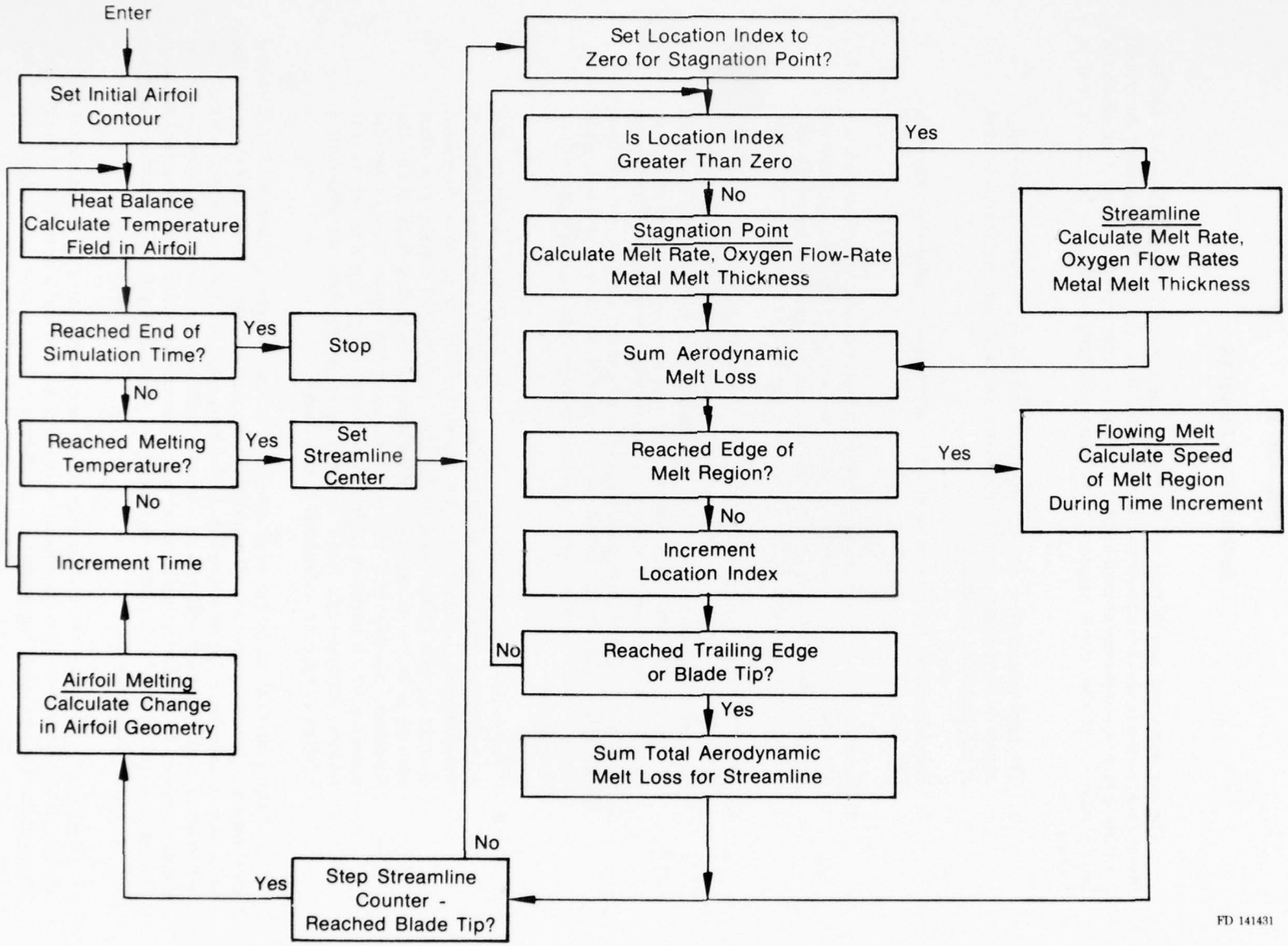

Figure 35. Generalized Combustion Program Logic

SECTION VI

SUMMARY OF RESULTS

The self-sustained combustion of a selected titanium alloy (Ti-8Al-1Mo-1V), has been investigated over a range of temperatures, pressures and flow-velocities encompassing the typical gas turbine engine compressor environment. Based on this experimental and analytical effort, the interrelationship of the several important environmental parameters may be summarized as follows:

1. The total temperature and the Reynolds number at the airfoil leading edge appear to be satisfactory correlation parameters for defining the lower limit of self-sustained combustion.

2. Burning rate in the chordwise direction is strongly dependant on Reynolds number.

3. Total damage is a function of spanwise burning rate, which in turn is a complex function of pressure, velocity, and temperature. Damage does not appear to be correlated by Reynolds number, but generally increases with temperature, an effect of the reduced heat sink cooling capacity of the airfoil.

4. Examination of high-speed film indicates the importance of melt removal by aerodynamic forces. At low velocities and reduced combustion rates, considerably quantities of liquid are retained and flow over the specimen promoting continued combustion, and are removed in relatively large globules. With increasing velocity, greater aerodynamic forces promote more rapid removal of burning droplets, which appear to be of progressively finer size. This behavior has considerable impact on the extent of downstream damage (fresh ignition sites) in a closed environment such as a gas turbine compressor.

5. Comparative tests performed at the same environmental conditions, but with different orientation of the specimens, show very significant effects of the aerodynamic angle-of-attack on the nature of the propagation. Specimen damage appears greater with angled than with parallel airflow. This effect appears to be due to changes in the nature of the airflow field around the specimen, possibly with separation or secondary flows in the spanwise direction, which results in rapid spanwise spreading of liquid metal over the surface. Although the result on combustion is apparent, the cause-effect relation is not fully understood at this time.

A basic analytical model has been developed to simulate the ignition and self-sustained combustion of stationary titanium alloy airfoils in gas turbine environments, and the model has been programmed for computer evaluation. Preliminary results with the model indicate that it is generally in good agreement with the test data in predicting the lower limits of self-sustained combustion and in simulating liquid metal flow; however, some details of the model required further development to provide a predictive technique generally applicable to a wide range of gas turbine engine environments.

The analytical model was further generalized and programmed for computer solution to include the effects of centrifugal body forces on liquid metal flow and propagation, thus extending its application to analysis of compressor stators and rotors. Also, to provide better agreement with

observed experimental behavior, liquid flow models were expanded to include aerodynamic coupling mechanisms controlling loss of melt from the surface, and physical property models were developed to include the effect of absorbed oxygen on thermodynamic and transport properties.

LIST OF SYMBOLS

Notation

C_D = aerodynamic drag coefficient

C_F = coefficient of friction

C_p = specific heat

D = oxygen diffusivity in metal

D_{on} = binary oxygen-nitrogen diffusion coefficient

E = internal energy

$\bar{F}$ = melt flow vector

F = melt flow scalar

F_r = radiation configuration factor

f = chordwise component of melt flow

g = oxygen convective flow in melt

h = radial component of melt flow

h_c = convective heat transfer coefficient

H = enthalpy of metal

$H_{o,o}$ = heat of reaction per unit mass of oxygen

H_{sl} = latent heat of fusion

$\bar{i},\bar{j}$ = unit vectors in chordwise and radial directions

k = thermal conductivity

K_{xm} = mass transfer coefficient

M = mass of oxygen bonded on surface

$\dot{m}$ = mass flow rate

$\dot{m}_e$ = mass flow rate at liquid edge

$\dot{m}_l$ = mass flow rate at blade leading edge

$\dot{m}_o$ = oxygen mass flux

n = direction normal to surface

LIST OF SYMBOLS

Notation

$\bar{q}_s$, q_s	=	surface heat flux vector, scalar
$\bar{q}_k$, q_k	=	internal conduction vector, scalar
R	=	leading edge aspect ratio
$\bar{R}$	=	radius to mid-span of blade
S,J	=	streamline position and location indices
s	=	distance along streamline
t	=	time
T	=	temperature in melted metal
T_g	=	gas temperature
T_m	=	melting temperature
T_n	=	node temperature
U	=	melting velocity of surface
U_∞	=	free-stream air velocity
u, v	=	chordwise and radial velocity components (melt)
$\bar{V}$,V	=	liquid metal velocity vector, scalar
W	=	width of streamline
X,Y,Z	=	chordwise, normal, radial coordinate system
X_e	=	end of liquid metal region
β	=	centrifugal body force per volume
γ	=	leading edge yaw angle
Γ	=	mass transport ratio (Eq. 37)
δ	=	liquid metal film thickness
δ_t	=	thickness of two-phase region
Δ	=	local thickness of airfoil

LIST OF SYMBOLS

Notation

ζ	=	component of surface tension parallel to surface
η	=	dimensionless distance from solid surface
θ	=	boundary layer momentum thickness
λ	=	thickness of liquid metal leading edge
Λ	=	mass transfer Peclet number
μ	=	dynamic viscosity of liquid metal
ν	=	kinematic viscosity of liquid metal
ν_m	=	kinematic viscosity at liquidus temperature
ξ	=	fraction of melt flow loss from surface
ρ	=	metal density
ρ_a	=	air density
σ	=	Stefan-Boltzmann constant
τ	=	aerodynamic shear stress in chordwise direction
τ_o	=	aerodynamic shear stress in radial direction
ϕ	=	local oxygen mass-fraction in liquid metal
$\bar{\phi}$	=	bulk (mean) oxygen mass-fraction in liquid metal
$x_{o,\,o}$	=	oxygen mol-fraction in air at surface
$x_{o,\,oo}$	=	oxygen mol-fraction in air free-stream
ψ	=	streamline angle relative to chord
ω	=	rotational speed of blade
Ω	=	angle of attack of test specimen
Mn	=	Mach number
N_{uo}	=	Nusselt number for heat transfer
P_r	=	Prandtl number
Re_θ	=	Reynolds number based on momentum thickness
Sc	=	Schmidt number
St	=	Stanton number for mass transport

LIST OF SYMBOLS (Concluded)

Notation

Subscripts

$_i$	=	interface of liquid and two-phase regions
$_s$	=	solid
$_l$	=	liquid
$_o$	=	liquid-solid interface
$_l$	=	liquid metal-air interface

REFERENCES

1. White, E. L, and J. J. Ward, "Ignition of Metals in Oxygen," DMIC Rpt. 224, 1966.

2. Littman, F. E., F. M. Church, E. M. Kinderman, "A Study of Metal Ignitions J. Less-Common Metals," 3.367.378, 1961.

3. Wolf, J. S., "Oxidation Behavior of Titanium Alloys Under High Heating Rates," AFML-TR-74-265, 1975.

4. Clark, A. F., J. C. Moulder, and C. C. Runyan, "Combustion of Bulk Titanium in Oxygen, Fifteenth Symposium on Combustion," Tokyo, 25-31 August 1974.

5. Moulder, J. C. and A. F. Clark, "Time Resolved Spectroscopy of Laser-Initiated Metal Combustion, Unconventional Spectroscopy," 82, 66-74, 1976.

6. *Boundary Layer Theory,* Fourth Edition, Hermann Schlicting, McGraw-Hill Book Company 1960, pp. 250-251, p. 414.

7. *Convective Heat and Mass Transfer,* W. M. Kays, McGraw-Hill Book Company, 1966, p. 162.

8. *Transport Phenomena,* R. B. Bird, W. E. Stewart, and E. N. Lightfoot, John Wiley & Sons, Inc., 1960 p. 510.

9. "Exploratory Development on Oxidation Behavior of Titanium Alloys Under High Heating Rates," James S. Wolf, Report No. AFML-TR-74-265, April 1975.

10. Wolf, J. S., Unpublished Data, Clemson University, 1977.

11. "Casting Properties of Titanium Alloys," O. N. Magnitskiy, 1968, Translation by Foreign Technology Division, WPAFB, 1970.

12. Schofield, T. H. and A. E. Bacon, *Journal of the Institute* of Metals, Vol. 84 (1955-56) p. 47.

13. *C.R.C. Handbook of Chemistry and Physics*, Chemical Rubber Co., 46th Edition, 1965.

14. Roe, W. P., H. R. Palmer, and W. R. Opie, "Diffusion of Oxygen in Alpha and Beta Titanium," Transactions of the ASM, Vol. 52 (1960) pp 191-200.

15. Touloukian, Y. S., *Metallic Elements and Their Alloys*, TPRC Databook, Vol. 1, Purdue Research Foundation, Lafayette, Indiana, 1964.

FR-10755
30 NOVEMBER 1978

TITANIUM AIRFOIL COMBUSTION PROGRAM USER'S MANUAL FOR DECK CCD 1152-0.0

Prepared Under Contract F33615-76-C-5041
for
Air Force Materials Laboratory
Air Force Systems Command
United States Air Force
Wright Patterson Air Force Base, Ohio 45433

PRATT & WHITNEY AIRCRAFT GROUP
Government Products Division
UNITED TECHNOLOGIES®
P. O. Box 2691
West Palm Beach, Florida 33402

Printed in the United States of America

TITANIUM AIRFOIL COMBUSTION PROGRAM USER'S MANUAL FOR DECK CCD 1152-0.0

TABLE OF CONTENTS

Section		*Page*
I	INTRODUCTION	I-1
II	DESCRIPTION OF THE PHYSICAL SYSTEM	II-1
III	THE ANALYTICAL MODEL	III-1
IV	DESCRIPTION OF THE COMPUTER PROGRAM	IV-1
	A. Purpose	IV-1
	B. General Description	IV-1
	C. Functions Performed	IV-1
V	GEOMETRIC NOMENCLATURE	V-1
VI	INPUT/OUTPUT	VI-1
	A. Input Description	VI-1
	B. Metal Thermal Conductivity Curve	VI-2
	C. Metal Specific Heat Curve	VI-2
	D. Titanium Liquid and Solidus Temperature Curve	VI-3
	E. Root Thickness Variations	VI-3
	F. Tip Thickness Variations	VI-4
	G. Root Velocity Profile	VI-4
	H. Tip Velocity Profile	VI-5
	I. Output Description	VI-6
VII	TEST CASE	VII-1
VIII	PROGRAM IDENTIFICATION AND REVISION PROCEDURE	VIII-1
	A. CCD Number	VIII-1
	APPENDIX A — Description of Program Functions	A-1
	APPENDIX B — Equation List	B-1
	APPENDIX C — Nomenclature	C-1
	APPENDIX D — References	D-1

LIST OF ILLUSTRATIONS

Figure		*Page*
II-1	Features of Burning Blade	II-2
IV-1	Program Logic Diagram	IV-2
IV-2	Streamline Indexing System	IV-3
V-1	Nomenclature of Airfoil Geometry	V-1
VII-1	Test Case Input Data	VII-2
VII-2	Test Case Input Data (Continued)	VII-3
VII-3	Test Case Input Data (Concluded)	VII-4
VII-4	Nodal Temperature Field	VII-5
VII-5	Combustion Propagation Data	VII-6
VII-6	Approximate Graphic Display	VII-7
VII-7	Calcomp Data Display	VII-8
VIII-1	Computer Simulation Change Notice	VIII-2
A-1	Boundary Layer Routine	A-2
A-2	Heat Balance Routine	A-3
A-3	Finite Difference Nodal Arrangement for Heat Transfer Analysis	A-4
A-4	Stagnation Point Routine	A-5
A-5	Stagnation Point Region of Burning Airfoil	A-6
A-6	Heat Flow and Velocity Relationship at Burning Leading Edge	A-6
A-7	TEMP Routine	A-7
A-8	Local Velocity Profiles and Nomenclature Used in Melt Flow Analysis	A-8
A-9	Streamline Routine	A-9
A-10	Leading Edge of Melt	A-10

SECTION I

INTRODUCTION

Pratt & Whitney Aircraft Group Customer Computer Deck (CCD1152-0.0) is an analytical model for the simulation of ignition and self-sustained combustion of titanium and its alloys in gas turbine engine compressor environments.

The object of the model is to predict the susceptibility of titanium to be ignited and undergo self-sustained combustion. In addition, if combustion occurs, the model predicts the characteristics and rate of propagation across the burning surfaces.

The program provides the capability of analyzing either compressor rotors or stators, with considerable flexibility in varying the geometry, material, and environmental conditions. Several different ignition modes can be considered, including external heat input, aerodynamic heating, mechanical rubbing, fracture, or melt impingement. Location of ignition can be specified or, in the case of aerodynamic heating, the model determines the location.

The User's Manual describes the Titanium Airfoil Combustion Program, its functional characteristics and operation, and the diagnostics necessary to assist in installation and checkout of the program in the user's facility.

SECTION II

DESCRIPTION OF THE PHYSICAL SYSTEM

Titanium is observed to burn in self-sustained combustion when ignited under certain environmental conditions. In particular, the conditions occurring in current axial-flow gas turbine engine compressors have been found to be favorable for the propagation of titanium fires. Figure II-1 illustrates the features of a burning compressor blade, ignited at the midspan leading edge. In this schematic, the leading edge of the blade is melting, and the liquid metal is driven by aerodynamic and centrifugal forces over the surface of the blade. Burning takes place at the liquid surface, generating heat which causes melting of the airfoil. The primary process for fire propagation is the flow of burning liquid metal. The rate and direction of spreading is defined by the combined thermal and mass transfer processes. The thermal process is controlled by the balance of heat gains (heat input and reaction) and heat losses (conduction, convection, and radiation), which together define the rate of melting. Two mass transfer processes occur, the transport of oxygen from the air into the liquid metal, controlling the reaction rate, and the flow of liquid metal over the airfoil surface, controlling the rate of propagation.

Melting occurs at the liquid-solid interface, and the resulting liquid spreads across the airfoil along the "melt edge," as shown in Figure II-1. In the case of nonrotating stators, liquid flow is in the chordwise direction only, driven by aerodynamic friction. Liquid metal, stripped from the surface by the airstream, or streaming from the trailing edge of the burning airfoil, provides the energy source to cause ignition of subsequent downstream compressor stages.

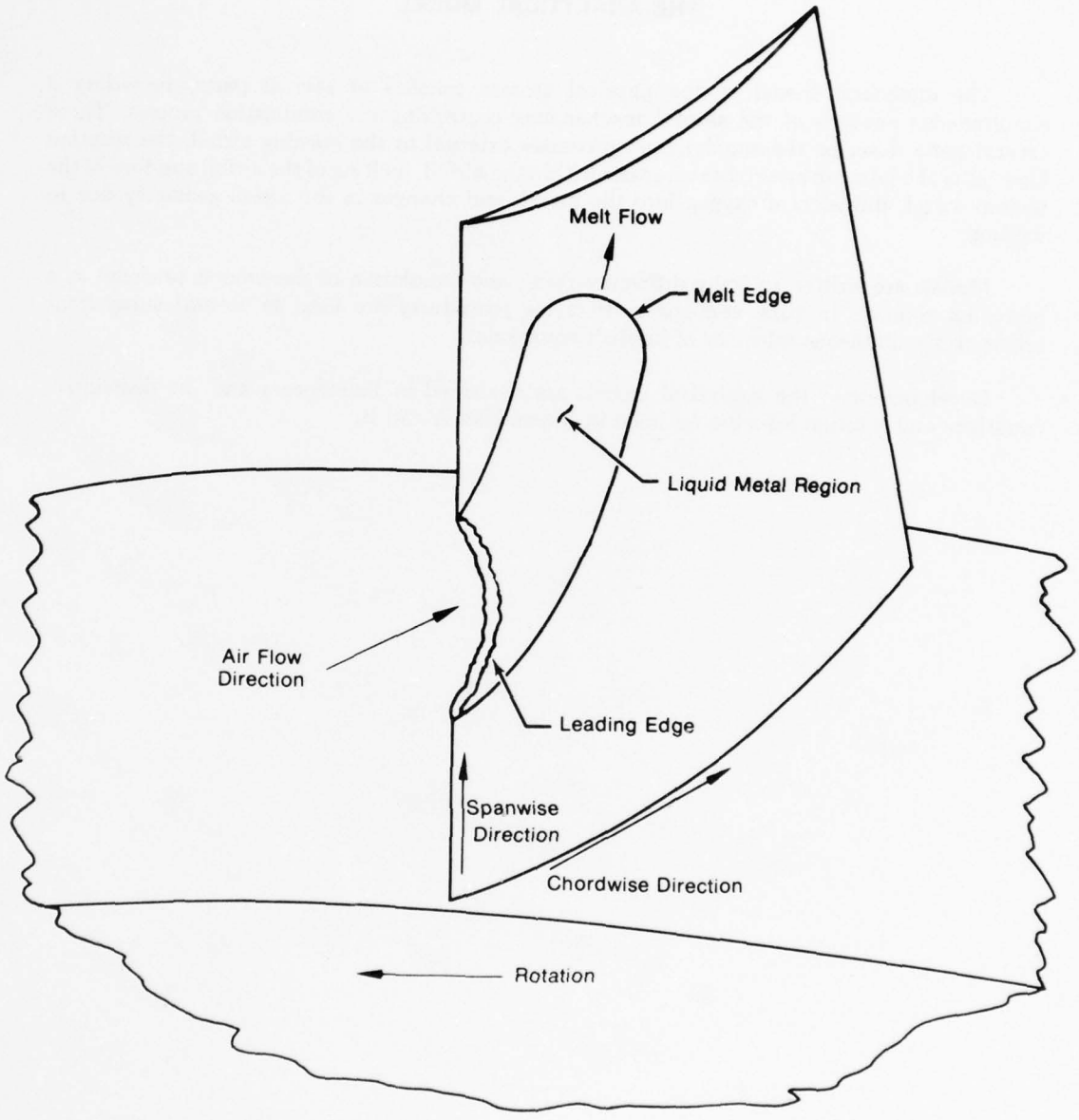

FD 141430

Figure II-1. Features of Burning Blade

SECTION III

THE ANALYTICAL MODEL

The analytical model of the physical system consists of several parts, providing a simultaneous analysis of the several mechanisms controlling the combustion process. These several parts describe the aerodynamic processes external to the burning airfoil, the reaction kinetics of the burning metal, heat transfer within the airfoil, melting of the airfoil and flow of the molten metal, diffusion of oxygen into the metal, and changes in the airfoil geometry due to melting.

Models are written in finite difference form, and simulation of the process procedes as a marching solution in time and space. Iterative procedures are used in several subsystems requiring simultaneous solutions of implicit equations.

Development of the analytical models are described in Reference 1 and the descriptive equations and solution logic are outlined in Appendices A and B.

SECTION IV

DESCRIPTION OF THE COMPUTER PROGRAM

A. PURPOSE

The purpose of the computer program is to provide an analytical technique for evaluating the susceptibility of titanium alloys to ignite and burn when used in gas turbine engine components. Specifically, the program is designed for analysis of axial flow compressor blades and vanes in the aerodynamic environment of high performance GTE compressors.

B. GENERAL DESCRIPTION

The overall system logic is shown in the flow diagram of Figure IV-1. Detailed flow diagrams of the major subsystems are shown in Appendix A. The program operates in two major sections, (a) evaluation of the temperature distribution in the solid metal and (b), evaluation of the melting and associated liquid metal processes. The first section operates in a time stepping mode, whether or not burning is occurring. If burning occurs, the liquid metal section operates for each time step to evaluate the melting process and spread of molten metal, and provides input for evaluation of the temperature field at the next time increment.

C. FUNCTIONS PERFORMED

Referring to Figure IV-1, the sequence of functional operation is in the following order:

1. Input geometry, environmental conditions, material properties, ignition mode and energy level,
2. Initialize systems: set nodal temperatures, velocity profile,
3. Calculate geometric quantities (nodal masses, areas, conduction path lengths),
4. Calculate aerodynamic boundary layer, shear stresses, heat and mass transfer coefficients,
5. Calculate surface heat generation,
6. Evaluate temperature field in airfoil,
7. Test for melting (if none, return to (3)),
8. If melting (and burning) occurs, perform leading edge (stagnation point) analysis-calculate liquid metal film thickness, oxygen absorption rates and diffusion profiles, melting rate, temperature profile,
9. Calculate same quantities along liquid flow streamlines,
10. Calculate spread of burning liquid over airfoil surface,
11. Some liquid metal removed from surface by air stream,
12. Evaluate change in airfoil geometry due to melting, and
13. Increment time and return to (3).

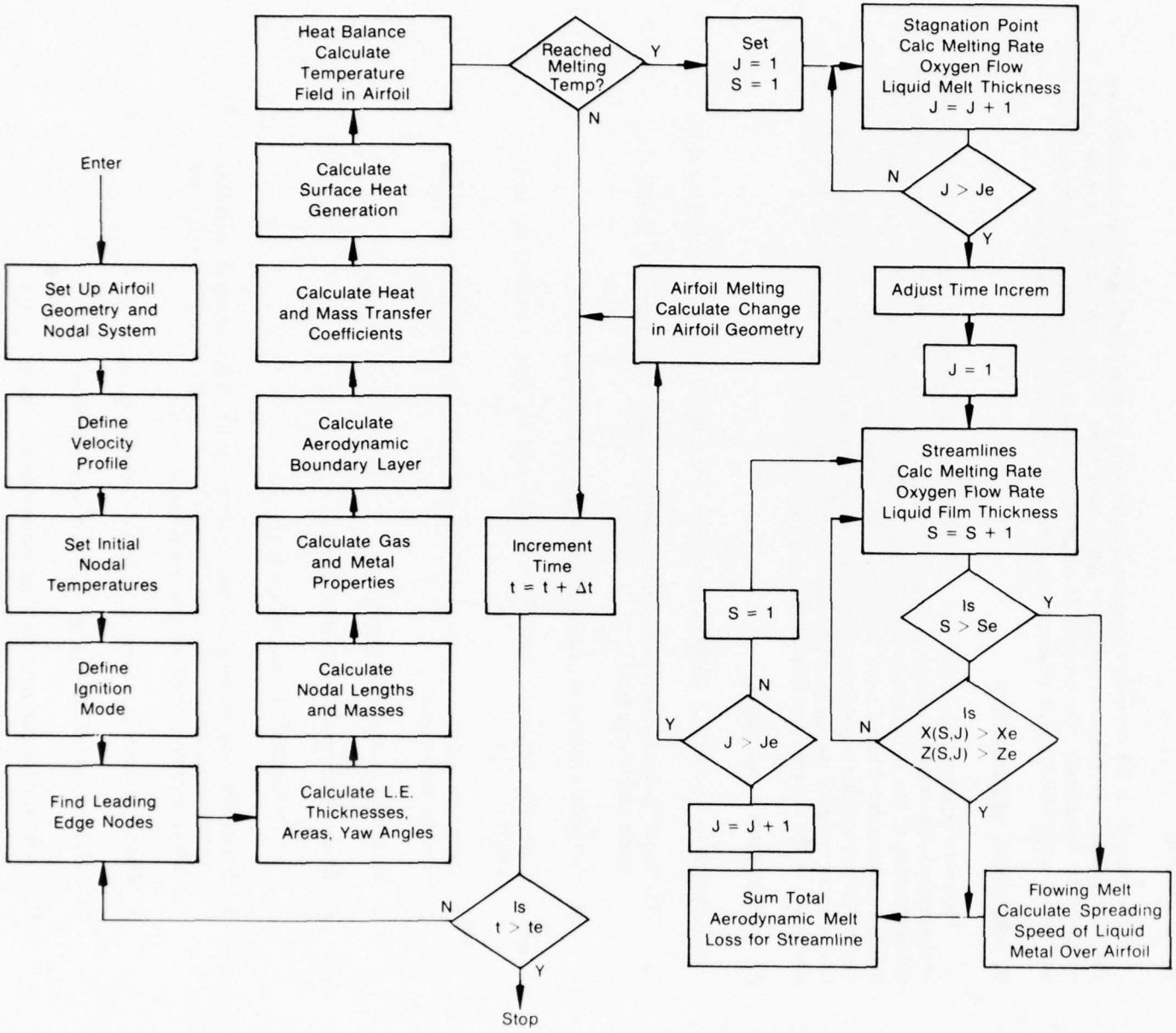

Figure IV-1. Program Logic Diagram

The procedure continues until a defined total simulation time is reached. In the flow diagram (X,Z) are coordinates in the chordwise and radial (spanwise) directions. Indices (J, S) refer to streamline index and incremental distance along streamline from airfoil leading edge, as shown in Figure IV-2. The subscripted indices (Je, Se), (Xe, Ze) refer to quantities at the "melt edge."

Detailed description of the functions and functional operation are presented in Appendix A.

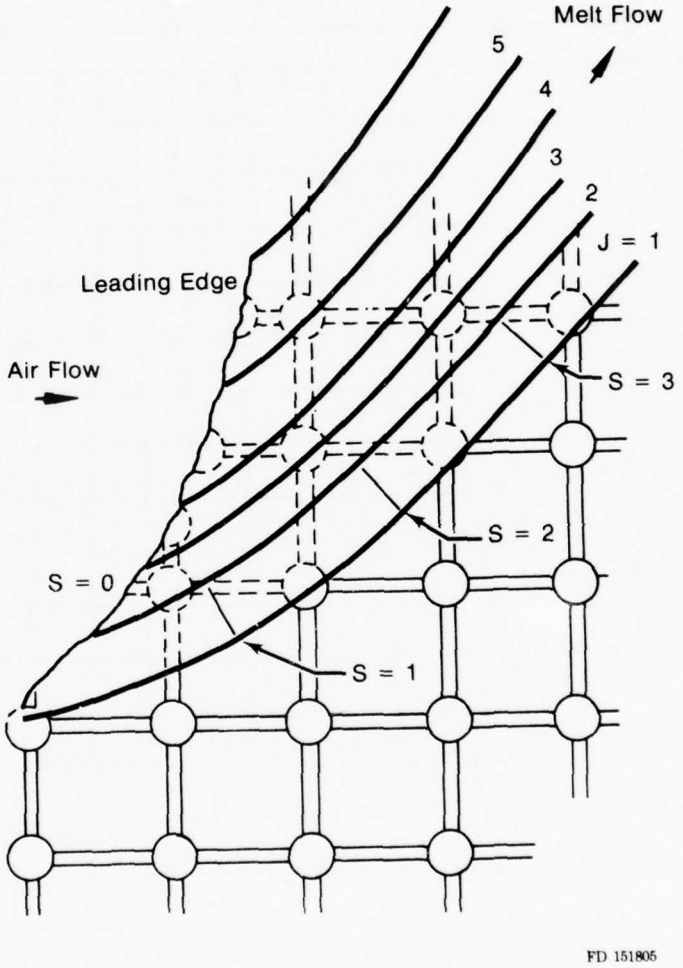

Figure IV-2. Streamline Indexing System

SECTION V

GEOMETRIC NOMENCLATURE

Figure V-1 illustrates the nodal breakup of an airfoil, and the significant geometric parameters. The number of spatial increments is currently fixed in the program, as shown in Figure V-1.

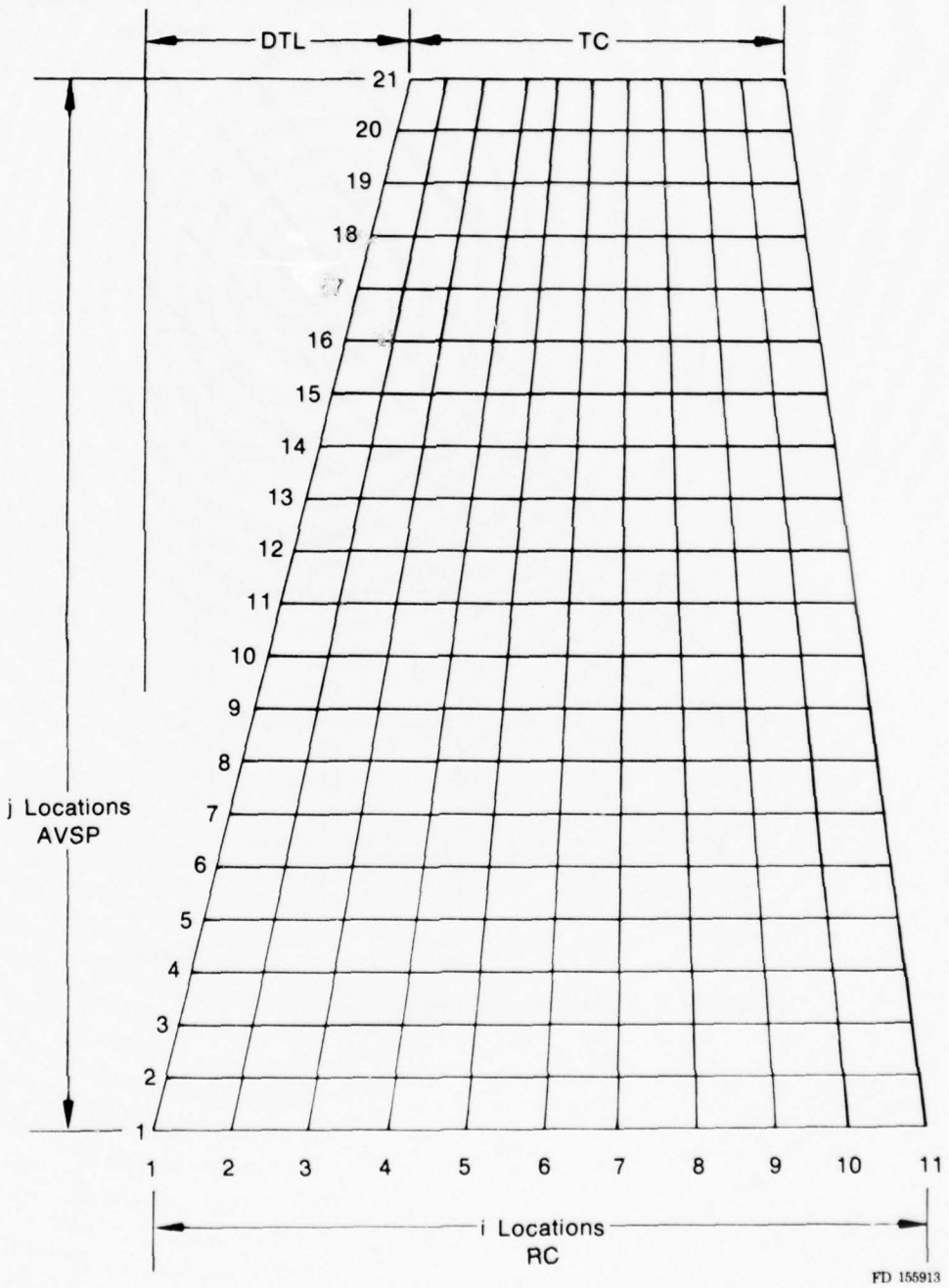

Figure V-1. Nomenclature of Airfoil Geometry

SECTION VI

INPUT/OUTPUT

The program requires as input the specification of airfoil geometry, material properties, environmental conditions, and mode of ignition energy input. The following input description illustrates the required format for card input of the specifying parameters.

Program output provides graphic and tabulated data on ignition occurrence, subsequent rates of airfoil damage and fire propagation, and resulting radial and axial carry-over of combustion products throughout the engine. Approximate graphic display is plotted on the printed output, and accurate graphic data is optionally available through the use of a Calcomp plotter.

A. INPUT DESCRIPTION

Card	*Columns*	*Variable*	*Definition*
1	1-80	TITLE	Any descriptive information to identify this case.
2	1-10	STPTIM	Total simulation time in seconds.
	11-20	TINC	Time increment for graphic output in seconds.
3	1-10	DTL	X-direction distance from the leading edge of the root to the leading edge of the tip in inches (sweep length). See Figure V-1.
	11-20	AVSP	Average airfoil span in inches.
	21-30	TC	Tip chord in inches.
	31-40	RC	Root chord in inches.
	41-50	ARAT	Aspect ratio of blade.
	51-60	RDISC	Distance from center of rotation to blade root in inches.
	61-70	VTAN	Tangential velocity of blade in ft/sec.
	71-80	TSTRT	Melting temperature of the metal in °R.
4	1-10	TCOOL	Free stream gas temperature in °R.
	11-20	PRES	Free stream gas pressure in psia.
	21-30	THOXID	Initial oxide thickness in inches.
	31-40	RHOM	Density of solid titanium in (lbm/in^3).
	41-50	RHOL	Density of liquid titanium in (lbm/in^3).
	51-60	KLIQ	Thermal conductivity of liquid titanium in (BTU/hr-ft-°R).
	61-70	TSINK	Temperature to which blade is radiating in °R. If input equal to zero, the gas temperature will be used.
	71-80	FEFA	Product of view factor and emissivity to be used for radiation heat transfer between blade and gas environment (Fr).
5	1-10	STEN	Surface tension in (lbf/ft).
	11-20	FLOS	Fraction of melt flow lost from surface (% loss/ft).
	21-30	CD	Coefficient of drag.

B. METAL THERMAL CONDUCTIVITY CURVE

Card	*Columns*	*Variable*	*Definition*
6	1-2	IK	Number of points in metal conductivity curve (maximum of 20 points, right-adjusted).
	3-10	VALKPT(1)	First temperature point in curve in °R.
	11-20	VALK(1)	Conductivity corresponding to first temperature in (Btu/hr-ft-°R).
	21-30	VALKPT(2)	Second temperature point in curve.
	31-40	VALK(2)	Conductivity corresponding to second temperature.
	41-50	VALKPT(3)	Same as VALKPT(2).
	51-60	VALK(3)	Same as VALK(2).
	61-70	VALKPT(4)	Same as VALKPT(2).
	71-80	VALK(4)	Same as VALK(2).

If IK >4, continue on another card in fields of 10. Omit input of *IK* on successive cards.

C. METAL SPECIFIC HEAT CURVE

Card	*Columns*	*Variable*	*Definition*
7	1-2	ICP	Number of points in metal specific heat curve (maximum of 20 points, right-adjusted).
	3-10	CPTVAL(1)	First temperature point in curve in °R.
	11-20	CPVAL(1)	Specific heat corresponding to first temperature in (Btu/lbm-°R).
	21-30	CPTVAL(2)	Second temperature point in curve.
	31-40	CPVAL(2)	Specific heat corresponding to second temperature.
	41-50	CPTVAL(3)	Same as CPTVAL(2).
	51-60	CPVAL(3)	Same as CPVAL(2).
	61-70	CPTVAL(4)	Same as CPTVAL(2).
	71-80	CPVAL(4)	Same as CPVAL(2).

If ICP >4, continue on another card in fields of 10. Omit input of ICP on successive cards.

D. TITANIUM LIQUID AND SOLIDUS TEMPERATURE CURVE

Card	*Columns*	*Variable*	*Definition*
8	1-2	NTS	Number of points in solid and liquid temperatures as a function of oxygen concentration (maximum of 20 points, right-adjusted).
	3-10	PHIV(1)	First oxygen mass fraction point in curve.
	11-20	TLIQ(1)	Temperature of liquid corresponding to first oxygen mass fraction in °R.
	21-30	TSOL(1)	Temperature of solid corresponding to first oxygen mass fraction in °R.
	31-40	PHIV(2)	Second oxygen mass fraction point in curve.
	41-50	TLIQ(2)	Temperature of liquid corresponding to second point in curve.
	51-60	TSOL(2)	Temperature of solid corresponding to second point in curve.

If NTS >2, continue on another card in fields of 10. Omit input of NTS on successive cards. Two sets of input per card.

E. ROOT THICKNESS VARIATIONS

Card	*Columns*	*Variable*	*Definition*
9	1-10	TCORD(1,1)	Root thickness at nodal location 1 in inches.
	11-20	TCORD(2,1)	Root thickness at nodal location 2.
	21-30	TCORD(3,1)	
	31-40	TCORD(4,1)	
	41-50	TCORD(5,1)	
	51-60	TCORD(6,1)	
	61-70	TCORD(7,1)	
	71-80	TCORD(8,1)	Root thickness at nodal location 8.
10	1-10	TCORD(9,1)	Root thickness at nodal location 9.
	11-20	TCORD(10,1)	
	21-30	TCORD(11,1)	Root thickness at nodal location 11.

F. TIP THICKNESS VARIATIONS

Card	*Columns*	*Variable*	*Definition*
11	1-10	TCORD(1,2)	Tip thickness at nodal location 1 in inches.
	11-20	TCORD(2,2)	Tip thickness at nodal location 2.
	21-30	TCORD(3,2)	
	31-40	TCORD(4,2)	
	41-50	TCORD(5,2)	
	51-60	TCORD(6,2)	
	61-70	TCORD(7,2)	
	71-80	TCORD(8,2)	
12	1-10	TCORD(9,2)	Tip thickness at nodal location 9.
	11-20	TCORD(10,2)	
	21-30	TCORD(11,2)	Tip thickness at nodal location 11.

G. ROOT VELOCITY PROFILE

Card	*Columns*	*Variable*	*Definition*
13	1-10	U(1,1)	Root velocity at nodal location 1 in (ft/sec).
	11-20	U(2,1)	Root velocity at nodal location 2.
	21-30	U(3,1)	
	31-40	U(4,1)	
	41-50	U(5,1)	
	51-60	U(6,1)	
	61-70	U(7,1)	
	71-80	U(8,1)	Root velocity at nodal location 8.
14	1-10	U(9,1)	Root velocity at nodal location 9.
	11-20	U(10,1)	
	21-30	U(11,1)	Root velocity at nodal location 11.

H. TIP VELOCITY PROFILE

Card	*Columns*	*Variable*	*Definition*
15	1-10	U(1,2)	Tip velocity at nodal location 1 in (ft/sec).
	11-20	U(2,2)	Tip velocity at nodal location 2.
	21-30	U(3,2)	
	31-40	U(4,2)	
	41-50	U(5,2)	
	51-60	U(6,2)	
	61-70	U(7,2)	
	71-80	U(8,2)	
16	1-10	U(9,2)	Tip velocity at nodal location 9.
	11-20	U(10,2)	
	21-30	U(11,2)	Tip velocity at nodal location 11.
16	1-5	IHEAT	Type of heat input. IHEAT=1, laser input. IHEAT=2, aerodynamic input. IHEAT=3, rub. IHEAT=4, metal impingement. IHEAT=5, fracture. Value must be a right-adjusted integer.
	6-10	NODES	Number of nodes which are effected by heat input. Not required if IHEAT=2. Value must be a right-adjusted integer.
	11-20	DTGAS	Input if IHEAT=2. Increase in gas temperature °R.
	21-30	QHIN	Input if IHEAT=1 or 3. Heat input in (Btu/sec-ft^2).
	31-40	XMINP	Input if IHEAT=4. Mass flow rate of liquid impinging on blade (lbm/sec-ft^2).
	41-50	HIMP	Input of IHEAT=4. Enthalpy of liquid impinging on blade (Btu/lbm).
	51-60	DTIME	Duration of ignition energy input in seconds.

Input card 17 if IHEAT=2 on Card 16 input Nodes (Card 16) values.

Card	*Columns*	*Variable*	*Definition*
17	1-2	INPI(1)	"I" location of first node effected by heat input.
	3-4	INPJ(1)	"J" location of first node effected by heat input.
	5-6	INPI(2)	
	7-8	INPJ(2)	
	77-78	INPI(20)	
	79-80	INPJ(20)	

If more than 20 points continue on another card. All values are right-adjusted integers.

I. OUTPUT DESCRIPTION

1. Initial external aerodynamics at midspan

Node	ith nodal location
X-Loc	Chordwise distance from leading edge, in.
Velocity	Local air stream velocity, ft/sec
Gas	Air temperature, °R
Press	Air static pressure, PSIA
Film Coefficient	Local heat transfer coefficient, Btu/hr-ft²—°R

2. Graphic display of airfoil at each output time. Plot shows the airfoil geometry and a map of the liquid metal region. Also included are the leading edge Reynolds number and the total aerodynamic melt losses in the axial and radial directions.

3. Tabulation of melting velocity at each burning leading edge node for each output time.

X-Loc	X-location of node, in.
Y-Loc	Y-location of node, in.
UX	X-component of melting velocity, ft/sec
UY	Y-component of melting velocity, ft/sec

4. Tabulation of spreading velocity at points along the edge of the liquid metal region of each output time.

X-Loc	X-location of point, in.
Y-Loc	Y-location of point, in.
UX	X-component of melting velocity, ft/sec
UY	Y-component of melting velocity, ft/sec

5. Table of temperatures (°R) at each nodal location (i, j) at each output time.

SECTION VII

TEST CASE

A representative test case is enclosed as Figures VII-1 through VII-7. This case is a simulation of a Ti 8-1-1 airfoil (1.0 in. chord, 2.0 in. span, constant thickness of 0.040 in.) ignited at the midspan leading edge. The aerodynamic environmental conditions (temperature, pressure, velocity) are 1320°R, 100 psia, and 445 ft/sec. Figures VII-1, -2, and -3 are the input data, describing the geometry, material properties, and environmental conditions. Simulated output data are shown in Figures VII-4 through VII-7, illustrating the output format.

Figure VII-4 shows the nodal temperature map in the airfoil 0.4 sec after ignition. Burned-out regions of the airfoil are shown in this figure as being at the melting temperature. Figure VII-5 shows the location of the burning leading edge, the extent of melt spread over the airfoil, leading edge regression rate, and the melt spreading velocity. Figure VII-6 is an unscaled graphic display printed on the computer output page. Figure VII-7 is a Calcomp plot of the same data in a scaled format.

```
CUSTOMER COMPUTER DECK 1152-0.0    4/12/79     PRATT AND WHITNEY AIRCRAFT GROUP

T I T A N I U M   A I R F U E L   C O M B U S T I O N   P R O G R A M

TEST CASE FOR TEMP DISTRIBUTION

STPTIM          TINC
  0.150        0.00600

DTC             AVSP            TC              RC              ARAT            RDISC           VTAN            TSTRT
  0.0            2.2200          1.0000          1.0000          0.5000         12.0000          0.0          3497.0000

TCOOL           PRES          THUXID          RHUM            RHOL            RLIQ            TSINK           FEFA
1320.0000      100.0000        0.0010          0.1600          0.1600          6.2400          0.0             1.0000

STEN            FLOS            CD
  0.0500    0.0         1.0000
```

METAL CONDUCTIVITY CURVE NO. OF POINTS = 6

TEMP	CONDUCTIVITY
1000.000	5.3410
1500.000	7.3190
2000.000	9.1534
2500.000	10.8800
3000.000	12.5440
3500.000	14.1400

METAL SPECIFIC HEAT CURVE NO. OF POINTS = 6

TEMP	SPECIFIC HEAT
1000.000	0.1470
1500.000	0.1620
2000.000	0.1770
2500.000	0.1920
3000.000	0.2070
3500.000	0.2220

SOLID AND LIQ TEMPS CURVE NO. OF POINTS =11

PHI	TEMP	TEMP
0.0	3497.000	3497.000
0.01500	3641.000	3515.000
0.03000	3713.000	3605.000
0.06000	3803.000	3605.000
0.07500	3821.000	3785.000
0.09000	3839.000	3839.000
0.12000	3821.000	3803.000
0.15000	3749.000	3659.000
0.16500	3731.000	3587.000
0.20000	3677.000	3587.000
0.25000	3659.000	3587.000

Figure VII-1. Test Case Input Data

THICKNESS VARIATION

ROOT	TIP
0.0	0.0
0.01300	0.01300
0.02600	0.02600
0.04000	0.04000
0.04000	0.04000
0.04000	0.04000
0.04000	0.04000
0.04000	0.04000
0.04000	0.04000
0.04000	0.04000
0.04000	0.04000

VELOCITY PROFILES

ROOT VELOCITY	TIP VELOCITY
0.44500E+03	0.44500E+03
0.44500E+03	0.44500E+03
0.44500E+03	0.44500E+03
0.44500E+03	0.44500E+03
0.44500E+03	0.44500E+03
0.44500E+03	0.44500E+03
0.44500E+03	0.44500E+03
0.44500E+03	0.44500E+03
0.44500E+03	0.44500E+03
0.44500E+03	0.44500E+03
0.44500E+03	0.44500E+03

HEAT INPUT

IHEAT	NODES	DTGAS	QHIN	XMINP	HIMP	DTIME
1	3	0.0	0.3280E+05	0.0	0.0	0.05000

NODES EFFECTED

I	J	I	J	I	J	I	J	I	J	I	J
1	10	1	11	1	12						

EXTERNAL AERODYNAMICS AT MIDSPAN

NODE	X-LOC (IN.)	VELOCITY (FT/SEC)	TGAS (DEG R)	PRESS (PSI)	FILM COEFF (BTU/HR-FT**2-R)
1	0.0	445.000	1332.654	100.000	2097.795
2	0.00833	445.000	1332.654	100.000	184.475
3	0.01667	445.000	1332.654	100.000	127.226
4	0.02500	445.000	1332.654	100.000	102.585
5	0.03333	445.000	1332.654	100.000	88.132
6	0.04167	445.000	1332.654	100.000	323.219
7	0.05000	445.000	1332.654	100.000	303.844
8	0.05833	445.000	1332.654	100.000	289.850
9	0.06667	445.000	1332.654	100.000	279.279
10	0.07500	445.000	1332.654	100.000	270.385
11	0.08333	445.000	1332.654	100.000	265.039

Figure VII-3. Test Case Input Data (Concluded)

TEMPERATURE MAP

TIME = 0.4000 TIME STEP = 0.00890

J	I=1	I=2	I=3	I=4	I=5	I=6	I=7	I=8	I=9	I=10	I=11
1	1332.7	1332.7	1332.7	1332.7	1332.7	1332.7	1332.7	1332.7	1332.7	1332.7	1332.7
2	1332.7	1332.7	1332.7	1332.7	1332.7	1332.7	1332.7	1332.7	1332.7	1332.7	1332.7
3	1332.7	1332.7	1332.7	1332.7	1332.7	1332.7	1332.7	1332.7	1332.7	1332.7	1332.7
4	1332.7	1332.7	1332.7	1332.7	1332.7	1332.7	1332.7	1332.7	1332.7	1332.7	1332.7
5	1332.7	1332.7	1332.7	1332.7	1332.7	1332.7	1332.7	1332.7	1332.7	1332.7	1332.7
6	1332.7	1332.7	1332.7	1332.7	1332.7	1332.7	1332.7	1332.7	1332.7	1332.7	1332.7
7	1332.7	1332.7	1332.7	1332.7	1332.7	1332.7	1332.7	1332.7	1332.7	1332.7	1332.7
8	1332.7	1332.7	1332.7	1332.7	1332.7	1332.7	1332.7	1332.7	1332.7	1332.7	1332.7
9	3300.0	3200.0	3060.0	1332.7	1332.7	1332.7	1332.7	1332.7	1332.7	1332.7	1332.7
10	3497.0	3497.0	3480.0	3365.0	3415.0	3390.0	3150.0	1332.7	1332.7	1332.7	1332.7
11	3497.0	3497.0	3497.0	3482.0	3460.0	3410.0	3390.0	3140.0	1332.7	1332.7	1332.7
12	3497.0	3497.0	3480.0	3365.0	3415.0	3390.0	3150.0	1332.7	1332.7	1332.7	1332.7
13	3300.0	3200.0	3060.0	1332.7	1332.7	1332.7	1332.7	1332.7	1332.7	1332.7	1332.7
14	1332.7	1332.7	1332.7	1332.7	1332.7	1332.7	1332.7	1332.7	1332.7	1332.7	1332.7
15	1332.7	1332.7	1332.7	1332.7	1332.7	1332.7	1332.7	1332.7	1332.7	1332.7	1332.7
16	1332.7	1332.7	1332.7	1332.7	1332.7	1332.7	1332.7	1332.7	1332.7	1332.7	1332.7
17	1332.7	1332.7	1332.7	1332.7	1332.7	1332.7	1332.7	1332.7	1332.7	1332.7	1332.7
18	1332.7	1332.7	1332.7	1332.7	1332.7	1332.7	1332.7	1332.7	1332.7	1332.7	1332.7
19	1332.7	1332.7	1332.7	1332.7	1332.7	1332.7	1332.7	1332.7	1332.7	1332.7	1332.7
20	1332.7	1332.7	1332.7	1332.7	1332.7	1332.7	1332.7	1332.7	1332.7	1332.7	1332.7
21	1332.7	1332.7	1332.7	1332.7	1332.7	1332.7	1332.7	1332.7	1332.7	1332.7	1332.7

Figure VII-4. Nodal Temperature Field

TIME = 0.40000

MELTING VELOCITY AT EACH BURNING LEADING EDGE NODE

X-LOC (IN)	Y-LOC (IN)	UX (FT/SEC)	UY (FT/SEC)
0.0	0.9310	0.0	0.03100
0.09996	0.9410	0.05200	0.02300
0.18720	0.9990	0.10700	0.03500
0.25992	1.1100	0.14200	0.0
0.18720	1.2210	0.10700	0.03500
0.09996	1.2790	0.05200	0.02300
0.0	1.2890	0.0	0.03100

SPREADING VELOCITY AT POINTS ALONG THE EDGE OF THE LIQUID METAL REGION

X-LOC (IN)	Y-LOC (IN)	UX (FT/SEC)	UY (FT/SEC)
0.10800	0.9310	0.04000	0.0
0.30000	0.9410	0.07400	0.0
0.48960	0.9990	0.14800	0.0
0.66000	1.1100	0.21000	0.0
0.48960	1.2210	0.14800	0.0
0.30000	1.2790	0.07400	0.0
0.10800	1.2890	0.04000	0.0

Figure VII-5. Combustion Propagation Data

TOTAL TIME FROM IGNITION (SECONDS) = 0.40000 TIME STEP USED(SECONDS) = 0.008900
TOTAL AERODYNAMIC LOSS (AXIAL) = 0.0 TOTAL AERODYNAMIC MELT LOSS (RADIAL) = 0.0
REYNOLDS NO. AT LEADING EDGE = 12920.000

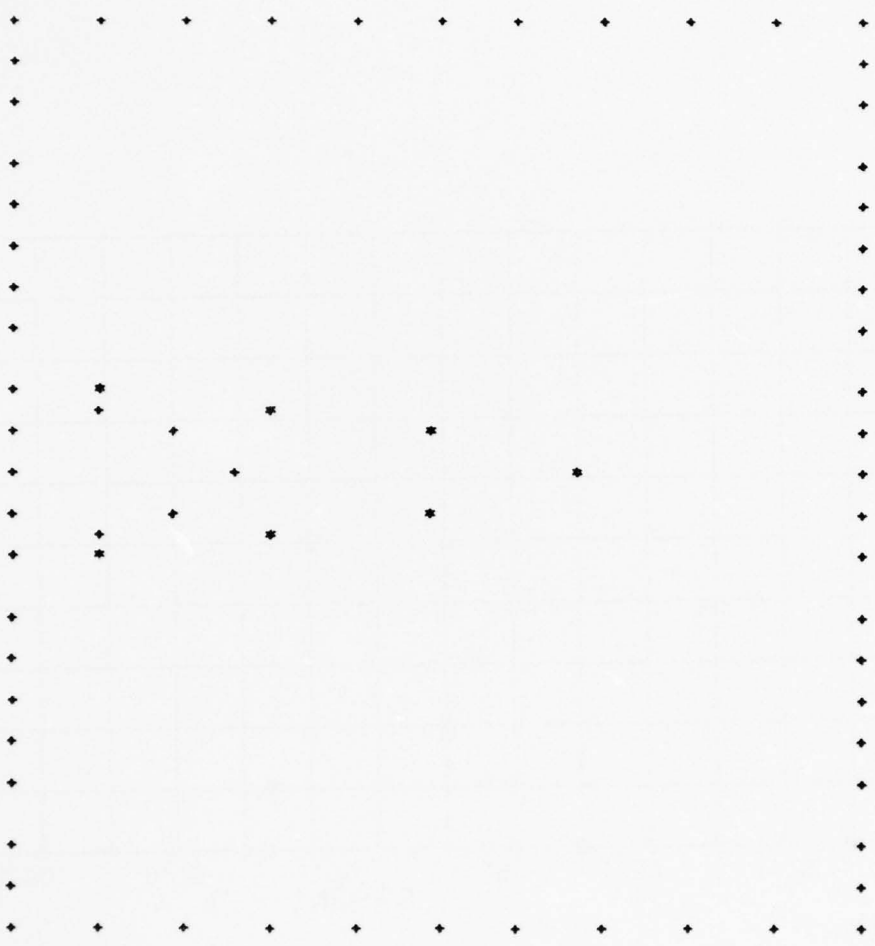

Figure VII-6. Approximate Graphic Display

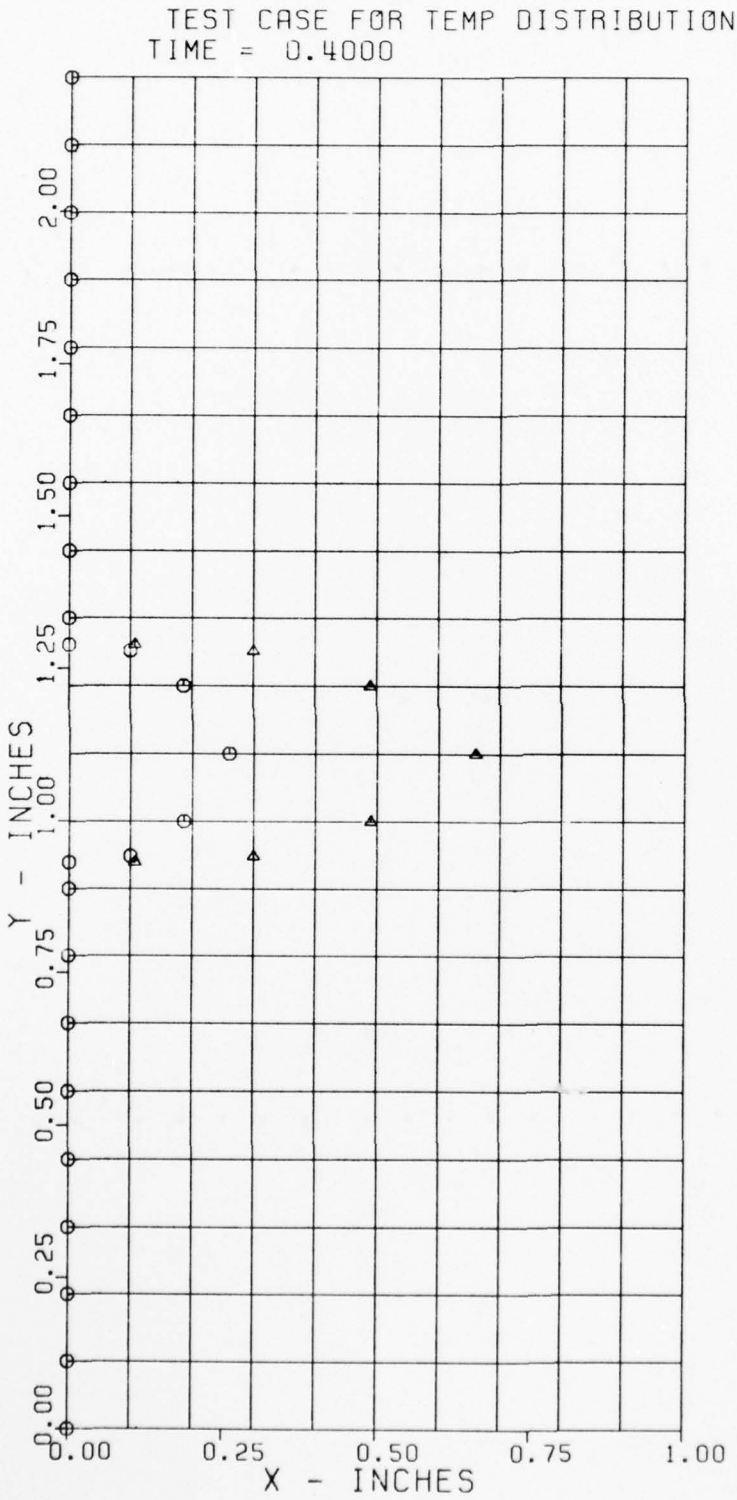

Figure VII-7. Calcomp Data Display

SECTION VIII

PROGRAM IDENTIFICATION AND REVISION PROCEDURE

A. CCD NUMBER

Customer Computer Decks (CCD's) are identified by a CCD number and date. An example is CCD 1001-0.0, 15 November 1969.

The CCD number consists of:

1. Basic number (first four digits)
2. Dash (or change) number
3. Decimal (or addition/correction) number.

1. Basic Number

This four-digit number generally corresponds to a given program. If another method is developed or studied which does not replace or supersede the original, a new four-digit number is issued.

2. Dash Number

Major changes in the program are reflected in different dash numbers. A change in techniques or mathematical methods would produce a new dash number provided the new techniques replace or change the old techniques. For more than nine changes, the dash number shifts to letters. The dash number of the original program is zero.

3. Decimal Number

The decimal is used for all other program changes such as:

1. Adding new optional routines
2. A change to the FORTRAN source language due to computer differences
3. Correcting a mistake in the program
4. Input and output changes
5. Adding unique customer oriented curves or initialization data.

In most cases a decimal number change is made and documented by writing an addendum to the user's manual without reprinting the user's manual. An errata or addendum to the user's manual is used in conjunction with a Computer Simulation Change Notice (Section V of CCD Approval Form — Figure VIII-1). This notice briefly describes the changes affecting the deck and manual.

Accompanying the notice is a new manual title page reflecting the new date and/or dash or decimal changes. The SCN also includes the change pages with black bars in the right-hand margin opposite data changed and a new date in the upper right-hand corner.

Programs revised by the user without written consent of the supplier are the responsibility of the user.

PRATT & WHITNEY AIRCRAFT GROUP
Government Products Division

IV COMPUTER SIMULATION CHANGE NOTICE NO. _____ (16)

(17) Date_____

Program Title_____

Changes Apply To:
(18) Computer Deck No._____ Dated_____ User's Manual No._____ Dated_____

New Designations:
(19) Computer Deck No._____ Dated_____ User's Manual No._____ Dated_____

Type of Change: ☐ Errata ☐ Addendum Changes Effect: ☐ Deck ☐ Manual

Change: Reason:

Detailed Reasons for Changes Are Shown in Enclosure. ☐

Approval:

Program Office, Engineering Section Manager_____

Engineering Computer Applications_____ (If no change in Engineering Department committment, only Engineering Computer Applications sign-off needed)

Instructions for Use of Forms (Continued)

(10) Action Taken to Satisfy Restrictions - Describe what you have done e.g. "Attach security labels to tape, binder, and User's Manual"

(11) Approved - For U.S. Government contracts, the Program Manager and the appropriate Manager, Engineering Branch, will sign in all cases. For non-contract decks with restrictions, the Manager, Engineering Branch. For all other decks, the Manager, Engineering Branch, may designate his Section Manager to approve transmittal

III User's Manual -Documentation Signoff - Used for all User's Manuals or other documentation supplied with the deck

(12) Program Manager (required for FR or PDS reports going outside GPD)

(13) Cognizant Engineering Personnel, as many as appropriate to insure adequate review - 1 required

(14) Cognizant Engineering Computer Applications Personnel, as many as appropriate to insure adequate review - 1 required

(15) Marketing Representative Coordinating with customer, if appropriate

IV Computer Simulation Change Notice This form must accompany errata or addenda to an existing manual and/or deck

(16) Change Notice No. (See ECA for this)

(17) Date of this notice

(18) Present CCD No. or GPD No. as Appropriate

(19) New Deck and Manual designations

PWA Form 10830A-D Rev 5/78 (Back)

Figure VIII-1. Computer Simulation Change Notice

APPENDIX A

DESCRIPTION OF PROGRAM FUNCTIONS

Figure IV-1 is a logic diagram outlining the functional operation of the program. Examination of this diagram shows three major sections of the program: (a) the input-initialization section, (b) the aerodynamic-heat transfer section, and (c) the combustion-liquid metal section. In Section IV the functional steps in the program operation were outlined. In this appendix the more complex functions will be described in terms of the equations and logic incorporated in their operation. The functions are described in the accompanying logic diagrams. In this appendix, the required equations are listed in Appendix B, and the nomenclature is defined in Appendix C.

The logic diagrams are prepared in symbolic equation form. Thus ①→θ means "Equation (1) from the Equation List is used to calculate θ, the boundary layer momentum thickness." Where a routine name, i.e., TEMP, appears in the logic flow, it refers to the use of subroutine TEMP to yield defined information.

The aerodynamic boundary layer calculation will be the first functional description. Prior to this function are the input and initialization functions describing the environmental condition, initial temperatures, properties, and initial geometry of the airfoil.

A. BOUNDARY LAYER ROUTINE

Figure A-1 shows the logic flow. Entry is made with the free stream velocity profile over the airfoil. Velocity may vary with distance, but is considered symmetrical on both airfoil surfaces. The function calculates the boundary layer growth, decides whether flow is laminar or turbulent, calculates the aerodynamic shear stress (Cf), the convective heat transfer coefficient, and the mass transfer coefficient (Kxm).

B. HEAT BALANCE ROUTINE

As shown in Figure A-2, entry is made with the metal node temperatures, with the surface-bonded oxide weight (either initial or from prior calculations), and with the mass transfer and heat transfer coefficients from BOUNDARY LAYER. The surface oxidation rate is determined from the selected kinetic reaction model, based on surface temperature. The reaction heat input is then balanced with other modes of heat transfer to determine the nodal temperatures throughout the airfoil. The energy equation (15) is written in finite difference form based on the nodal arrangement illustrated in Figure A-3. The central temperatures Tn, Tn' are defined as those at the beginning and end of a time increment. Equation (16) defines the time increment parameter and Eq. (17) is the stability criterion, defining the maximum allowable time increment for stable calculation.

After calculating the nodal temperatures, they are tested to determine whether melting has occurred at any point in the airfoil. If melting occurs, the program branches to the liquid metal section to evaluate reaction, flow and other associated processes. If no melting occurs, time is advanced by one increment, and the program returns to perform another heat transfer analysis.

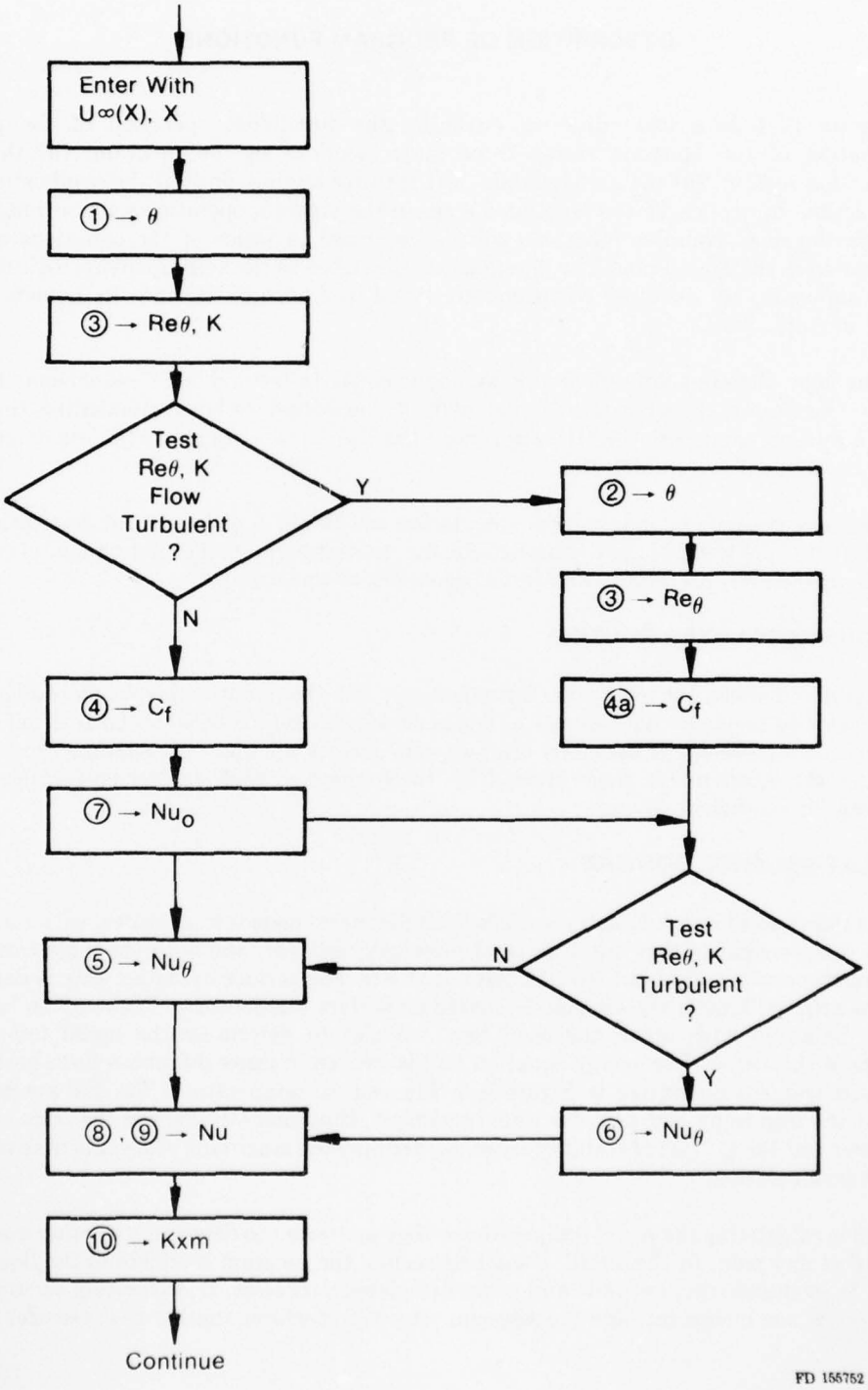

Figure A-1. Boundary Layer Routine

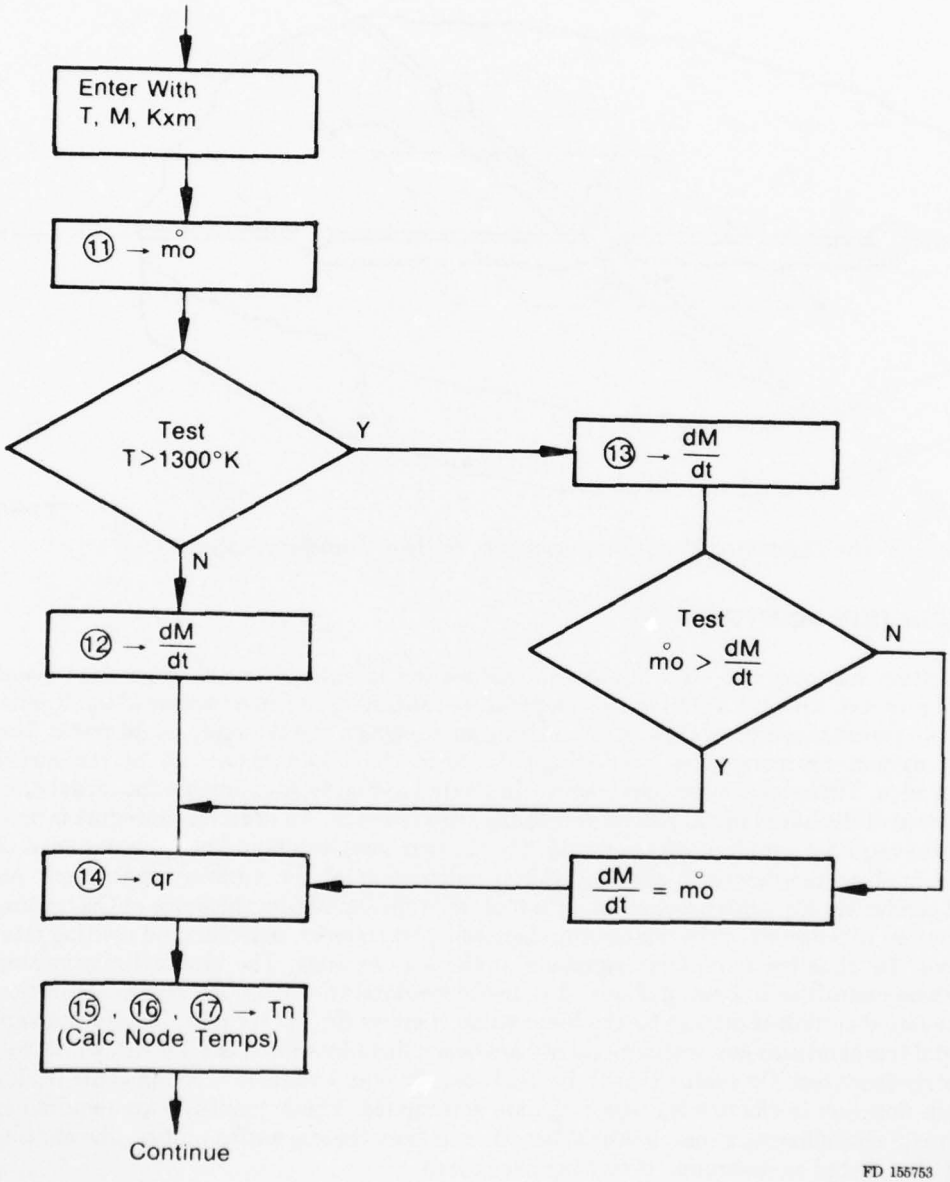

Figure A-2. Heat Balance Routine

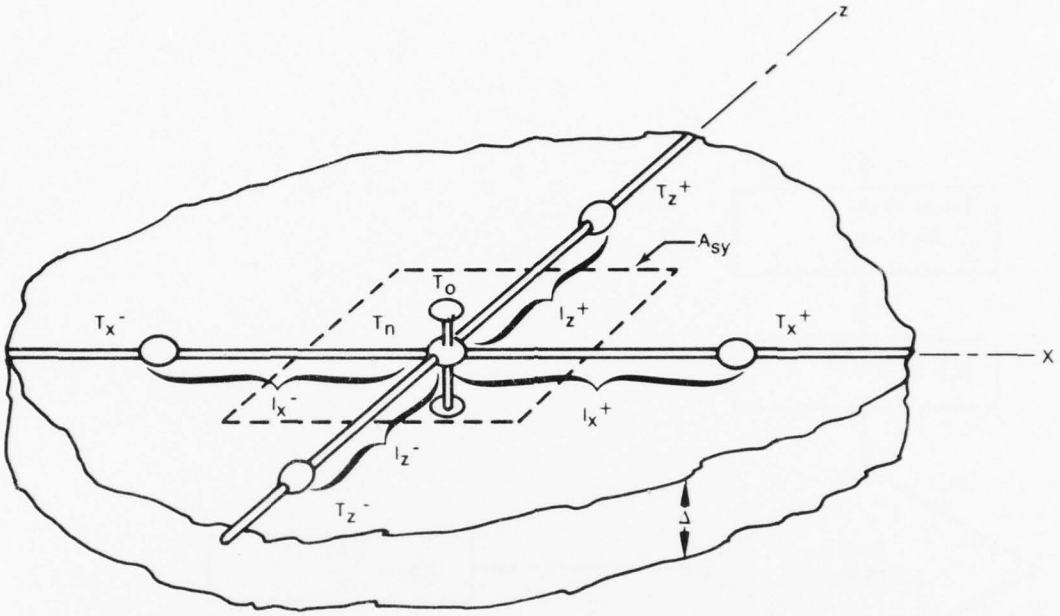

FD 145248

Figure A-3. Finite Difference Nodal Arrangement for Heat Transfer Analysis

C. STAGNATION POINT ROUTINE

If melting has occurred, the liquid analysis section is entered in the stagnation point routine, Figure A-4, with the airfoil metal temperature thickness, and environmental conditions. This routine simultaneously evaluates the melting rate, oxygen uptake rate, liquid metal film thickness, oxygen concentrations, and temperatures in the liquid metal, all at the airfoil stagnation edge. These calculated parameters, illustrated in Figure A-5, provide the initial data for calculation of the liquid metal processes over the airfoil surface. An iterative procedure is used to obtain the required simultaneous solutions. On the first pass, the liquid metal is assumed to be at the melting temperature, allowing initial calculation of the various parameters. An empirical corelation, Eq. (19), provides an initial value of the liquid film thickness at the leading edge. Equation (21) describes the relationship between heat transfer, reaction, and melting rate, and defines the direction of surface regression at the leading edge. The physical relationship between these quantities is shown in Figure A-6. In the main iteration loop, the oxygen absorption rate at the liquid surface is defined by the lower value of either Eq. (11) or (25). In the next step, liquid metal temperatures and melting velocity are determined by subroutine TEMP, which will be separately described. On completion of the iteration, the liquid metal flow components (f_o, h_o) and oxygen flow rate in the flowing liquid (g_o) are determined. These quantities are required as initial data for the following streamline analysis. On exit from the stagnation routine, the melting velocity (U) is tested to determine if melting has ceased.

D. TEMPERATURE ROUTINE

This subroutine, Figure A-7, determines the temperatures in the liquid metal film, and the melting velocity of the surface. The model assumes that the liquid metal film is composed of a solid-liquid two-phase region, and a superheated region, as shown in Figure A-8. The model is further developed on the assumption that melting is distributed throughout the two-phase region. This subroutine requires the thermodynamic properties of the alloy, i.e., liquidus and solidus temperatures as functions of absorbed oxygen, and enthalpy as a function of oxygen content and temperature.

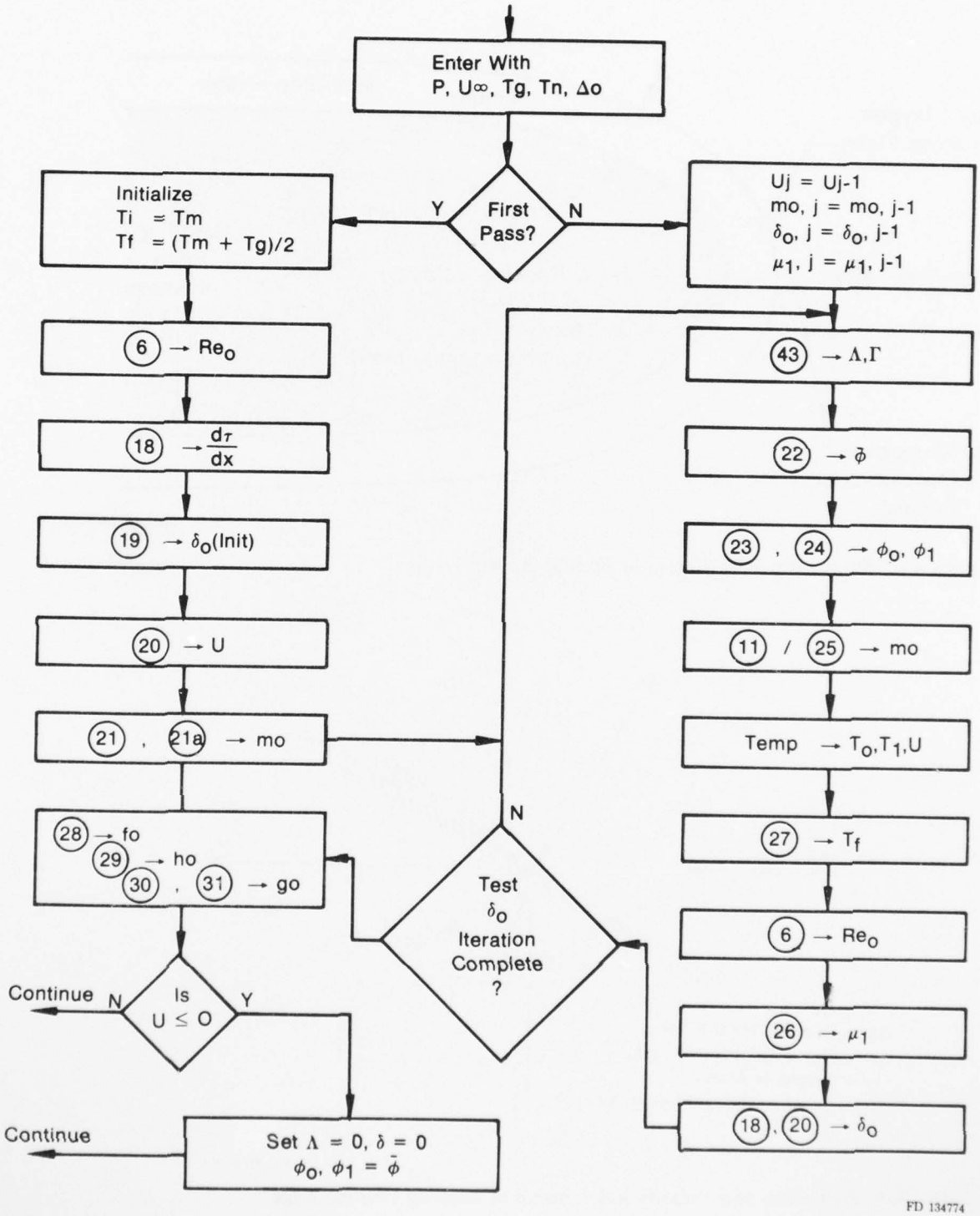

Figure A-4. Stagnation Point Routine

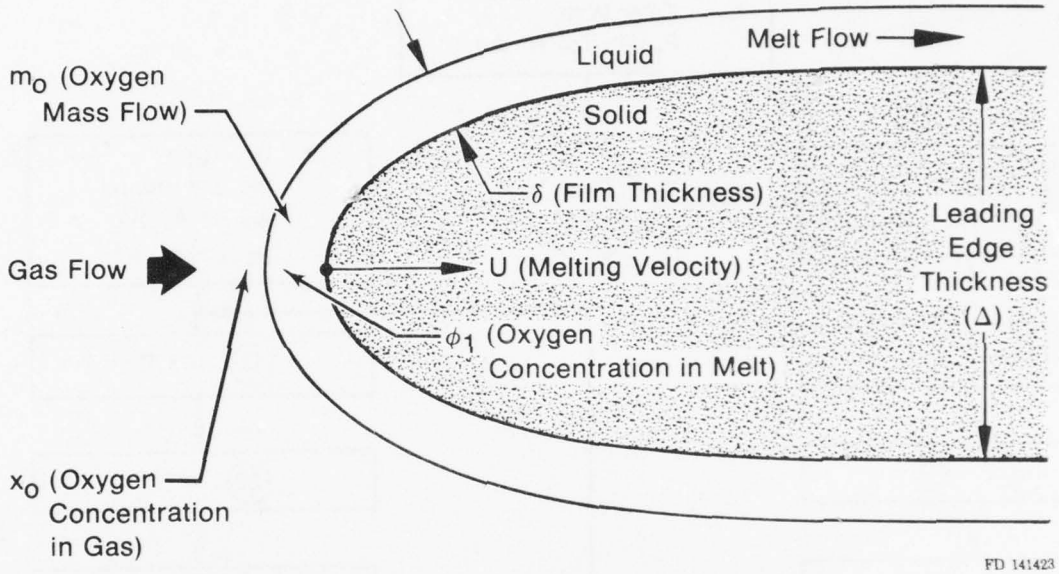

Figure A-5. Stagnation Point Region of Burning Airfoil

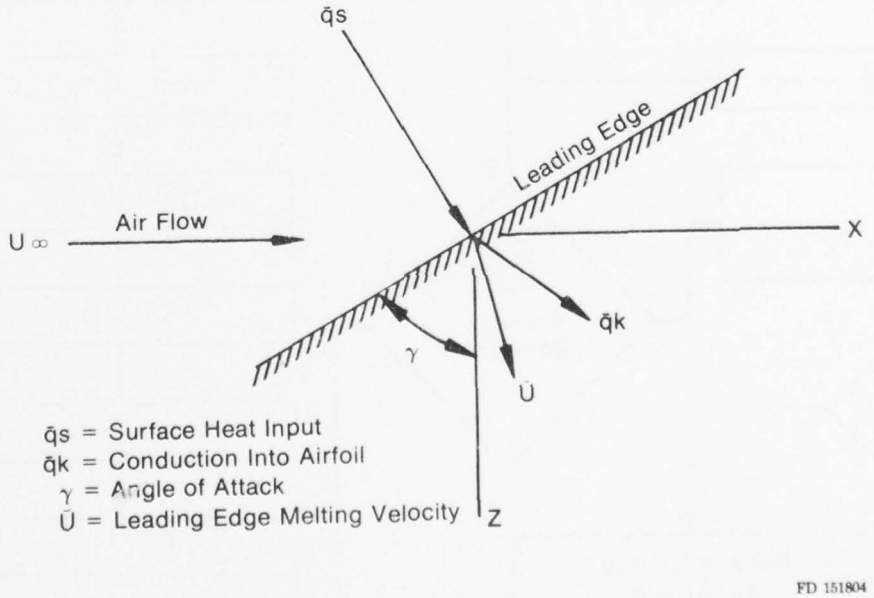

Figure A-6. Heat Flow and Velocity Relationship at Burning Leading Edge

AD-A072 529 PRATT AND WHITNEY AIRCRAFT GROUP WEST PALM BEACH FL G--ETC F/G 11/6
TITANIUM CMBUSTION RESEARCH PROGRAM AND USER'S MANUAL FOR DECK --ETC(U)
MAR 79 M R GLICKSTEIN F33615-76-C-5041

UNCLASSIFIED PWA-FR-10748 AFML -TR-79-4001 NL

2 OF 2
ADA
072529

END
DATE
FILMED
9-79
DDC

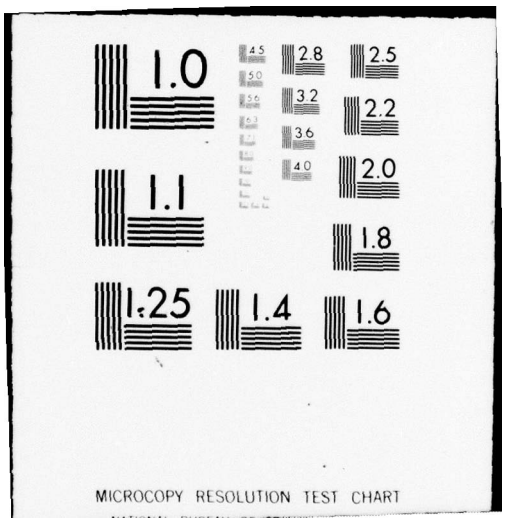
1.0
1.1
1.25
1.4
1.6
1.8
2.0
2.2
2.5
2.8
3.2
3.6
4.0
4.5
5.0
5.6
6.3
MICROCOPY RESOLUTION TEST CHART

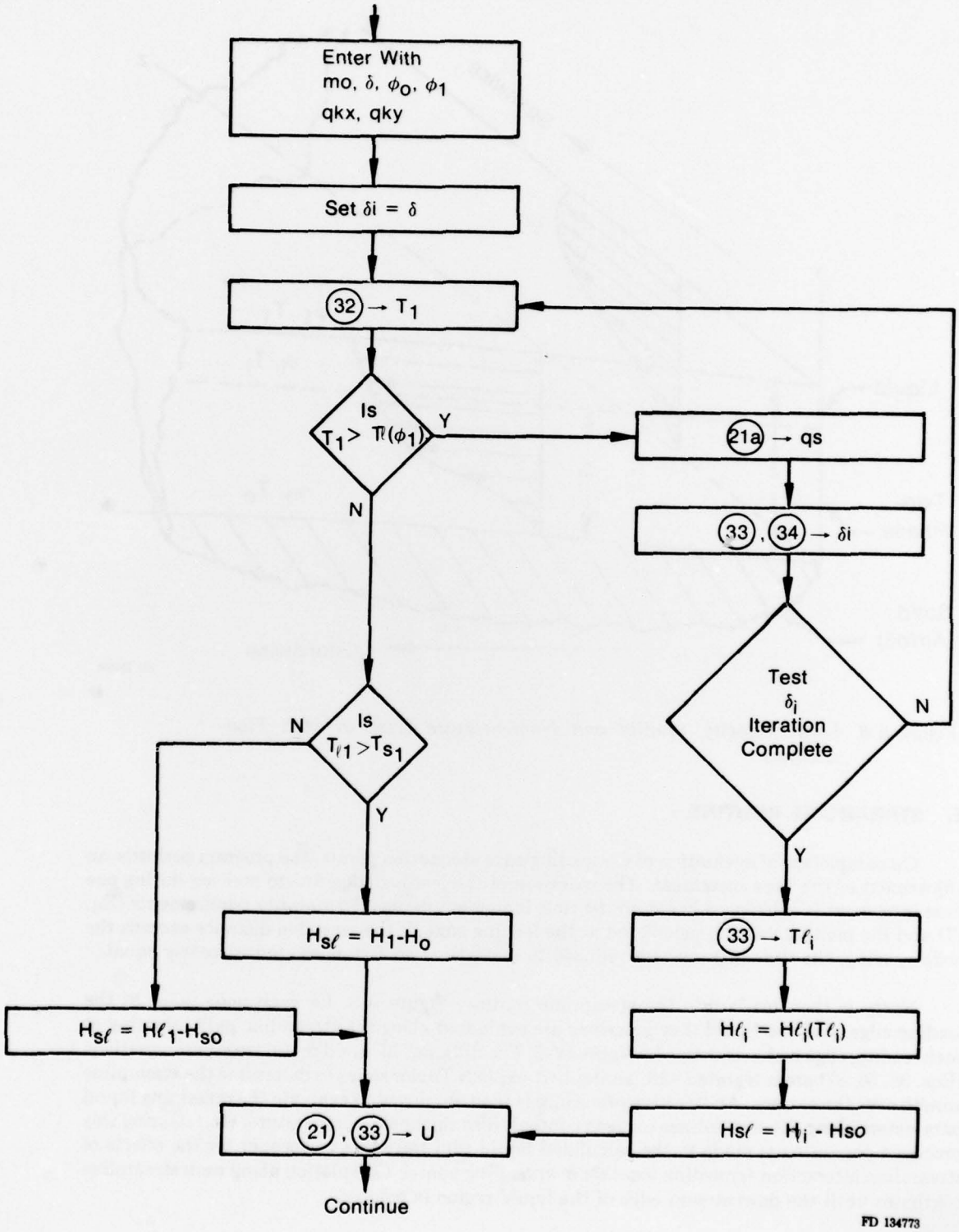

Figure A-7. TEMP Routine

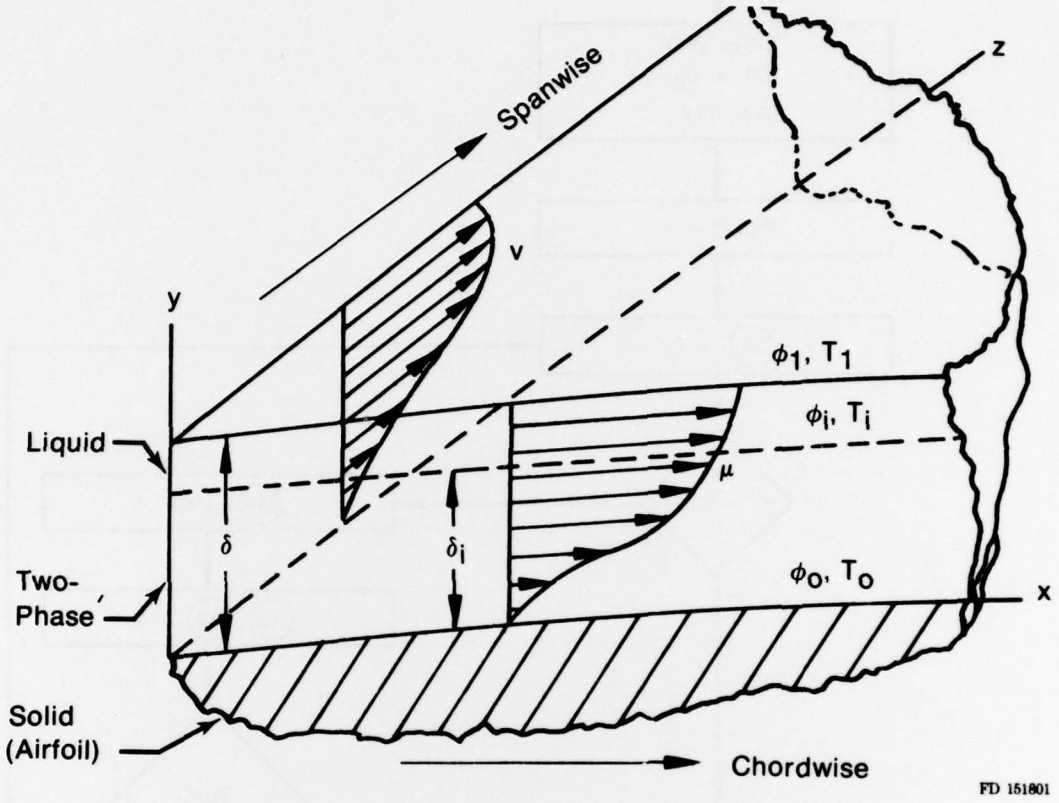

Figure A-8. Local Velocity Profiles and Nomenclature Used in Melt Flow Analysis

E. STREAMLINE ROUTINE

On completion of evaluation of the leading edge stagnation points, the program performs an adjustment of the time increment. The recession of the leading edge due to melting during one time increment is calculated based on the time increment defined by stability requirements (Eq. 17) and the melting velocity calculated at the leading edge. If the recession distance exceeds the node spacing, the time increment is reduced to make the two distances approximately equal.

Entry is then made into the streamline routine, Figure A-9, for each node point at the leading edge, and the liquid flow processes are evaluated along the streamline paths starting at each leading edge node, as shown in Figure IV-2. The differential liquid metal transport equations (Eqs. 35, 36, 37) are integrated with an implicit-explicit Taylor series to determine the streamline growth over the surface. An iterative procedure is then employed to evaluate the remaining liquid parameters along the streamlines (oxygen content, film thickness, temperature, etc.). During this process a correction is made to the calculated liquid film thickness to account for the effects of streamline interaction (crowding together or spreading apart). Calculation along each streamline continues until the downstream edge of the liquid region is reached.

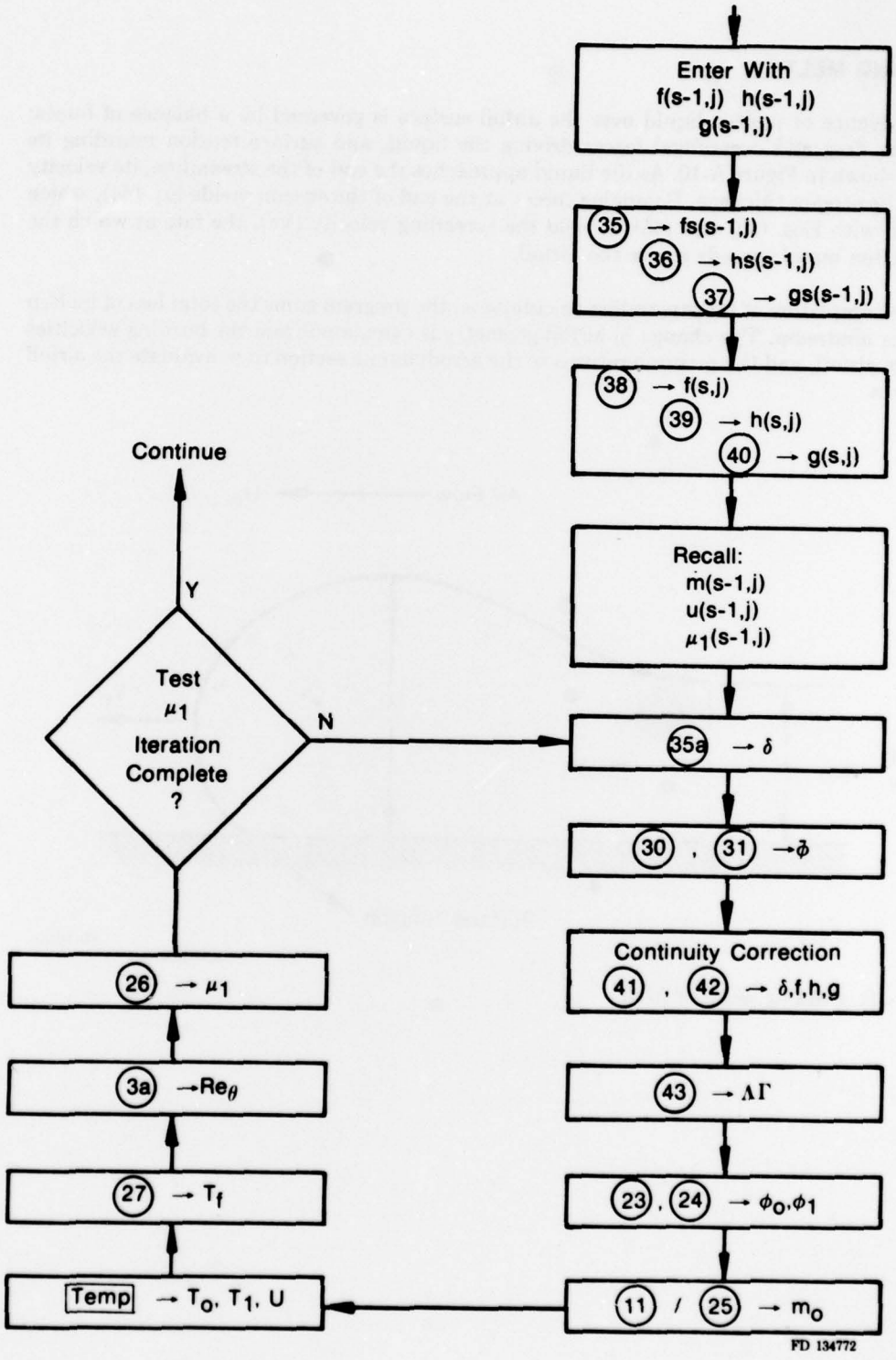

Figure A-9. Streamline Routine

F. FLOWING MELT

The advance of molten liquid over the airfoil surface is governed by a balance of forces; aerodynamic drag and centrifugal forces driving the liquid, and surface tension retarding its motion, as shown in Figure A-10. As the liquid approaches the end of the streamline, its velocity slows and the stream thickens. Balancing forces at the end of the stream yields Eq. (44), which is combined with Eqs. (30) and (45) to yield the spreading velocity (Ve), the rate at which the burning molten metal spreads across the airfoil.

At the completion of the streamline calculations, the program sums the total loss of molten metal to the airstream. The change in airfoil geometry is calculated from the burning velocities (U) over the airfoil, and the program returns to the aerodynamic section to re-evaluate the airfoil temperatures.

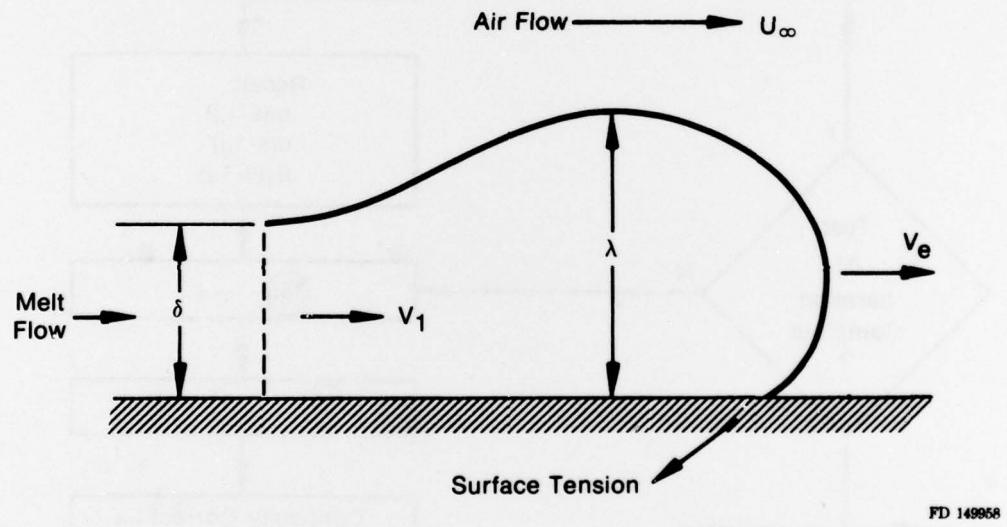

Figure A-10. Leading Edge of Melt

APPENDIX B

EQUATION LIST

$$\frac{U_\infty \theta^2}{\nu_a} = \frac{0.47}{U_\infty^5} \int_0^x U_\infty^5 \, dx \qquad \text{(Laminar Flow)} \quad (1)$$

$$\theta \left(\frac{U_\infty \theta}{\nu_a} \right)^{1/4} = U_\infty^{-4} \left[C_1 + 0.16 \int_{xt}^x U_\infty^4 \, dx \right] \qquad \text{(Turbulent Flow)} \quad (2)$$

$$Re\theta = \frac{U_\infty \theta}{\nu_a}, \quad K = \frac{\theta^2}{\nu_a} \frac{dU_\infty}{dx} \qquad (3)$$

$$C_f = \frac{\text{func (K)}}{Re\theta} \qquad \text{(Laminar)} \quad (4a)$$

$$C_f = 0.0256 \, Re\theta^{-1/4} \qquad \text{(Turbulent)} \quad (4b)$$

$$N_u\theta = \frac{PrRe\theta \sqrt{C_f/2}}{5Pr + 5 \ln (5Pr + 1) + \sqrt{2/C_f} - 14} \qquad \text{(Laminar)} \quad (5a)$$

$$N_u\theta = \frac{hc \, \theta}{k} \qquad (5b)$$

$$Nu\theta = \frac{Re\theta \, Pr^{1/3} \, C_f}{2} \qquad \text{(Turbulent)} \quad (6)$$

$$Nu_o = 1.14 \, Re_o^{1/2} \, Pr^{0.371} \qquad (7a)$$

$$Nu_o = \frac{hc \, \Delta_o}{k} \qquad (7b)$$

$$Re_o = \frac{U_\infty \, \Delta_o}{\nu_a} \qquad (7c)$$

$$f(\gamma) = [\, 0.0242 \, e^{-2(\gamma - \pi/2)} + \cos \gamma \,]^{0.62} + 0.05 \sin \gamma \qquad (8a)$$

$$0 < \gamma < \pi/2$$

$$f(\gamma) = \{[\, 0.0242 \, e^{-2(\gamma - \pi/2)} + \cos \gamma \,]^{0.62} + 0.05 \sin \gamma \,\} \, (3.5^{-0.494\eta^4}) \qquad (8b)$$

$$\pi/2 < \gamma < \pi$$

$$N_u = N_{u_{calc}} \, [1 - (1 - f(\gamma)) \, e^{-arg}] \qquad (9)$$

$$arg = -0.015 \, Re\theta \; [\text{If } arg < -180] \; arg = -180$$

$$Kxm = \frac{\rho D_{on} \, Nu_\theta}{\theta} \left(\frac{Sc}{Pr} \right)^{1/3} \qquad (10)$$

$$\dot{m}_o = Kxm \left(\frac{\chi_{o.oo} - \chi_{o.o}}{1 - \chi_{o.o}} \right) \tag{11}$$

$$\frac{dM}{dt} = \frac{3.63 \times 10^7 \, e^{-\frac{29640}{T}}}{M}, \quad T < 1300°K \tag{12}$$

$$\frac{dM}{dt} = 2.60 \times 10^8 \, e^{-\frac{10065}{T}}, \quad T \geq 1300°K \tag{13}$$

$$q_r = H_{o.o} \frac{dM}{dt} \tag{14}$$

$$\frac{\Delta}{\theta} (T_n' - T_n) = \frac{\Delta(\ell_x^+ + \ell_x^-)}{2\ell_x^+} (T_x^+ - T_n) + \frac{\Delta(\ell_x^+ + \ell_x^-)(T_x^- - T_n)}{2\ell_x^-} +$$

$$\frac{\Delta(\ell_x^+ + \ell_x^-)}{2\ell_z^+} (T_z^+ - T_n) + \frac{\Delta(\ell_x^+ + \ell_x^-)(T_z^- - T_n)}{2\ell_z^-} + \tag{15}$$

$$\frac{12 \alpha A_{sy}}{\Delta^2} (T_o - T_n) + \frac{2(1-\alpha) A_{sy}}{k} [\, h_c (T_g - T_n) - q_{rad} + Q_{RS} + q_{k/z} \,]$$

$$\frac{\Delta}{\theta} = \frac{A_{sy} \Delta}{\kappa \Delta t} = \frac{(\ell_x^+ + \ell_x^-)(\ell_z^+ + \ell_z^-) \Delta}{4 \kappa \Delta t} \tag{16}$$

$$\theta \leq \frac{1}{\frac{(\ell_x^- + \ell_x^-)(\ell_z^+ + \ell_z^-)}{2\ell_x^+ \ell_x^-} + \frac{(\ell_x^+ + \ell_x^-)(\ell_z^+ + \ell_z^-)}{2\ell_z^+ \ell_z^-} + \frac{12 \alpha A_{sy}}{\Delta^2} + \frac{2(1-\alpha) A_{sy} h_c}{k\Delta}} \tag{17}$$

$$\frac{d\tau}{dx} = \frac{\rho_s U_\infty^2}{2} [543 - 860R + 347R^2] [R - 0.3634R^{2.8}]^{1.5} \frac{Re_o^{-1/4}}{\Delta} \tag{18}$$

$$\frac{\delta_o}{\Delta_o} = 140 \, Re_o^{-1.1} + 0.02 \tag{19}$$

$$\frac{\delta^3 \beta \sin \gamma}{R\Delta} + 2 \delta^2 \frac{d\tau}{dx} \cos^2 \gamma = 12 \mu_1 U \tag{20}$$

$$\rho H_{s1} \bar{U} = \bar{q}_s - \bar{q}_k, \tag{21}$$

$$\bar{q}_s = \hat{i}_n [\dot{m}_o H_\infty + h_c (T_g - T_1) - \sigma F_r T_1^4] \tag{21a}$$

$$\bar{\phi} = \frac{\dot{m}_o}{\rho \bar{U}} \tag{22}$$

$$F_1 \phi_1^2 + [(2 + \Lambda) F_2 - \Gamma F_1] \phi_1 + \left[\left(1 + \frac{\Lambda}{2}\right)^2 (F_3 - \bar{\phi}^2) + \frac{\Gamma^2}{4} F_1 \right.$$

$$\left. - \left(1 + \frac{\Lambda}{2}\right) \Gamma F_2 \right] = 0 \tag{23}$$

$$F_1 = \left(1 + \frac{9\Lambda}{20}\right)^2 + \frac{\left[B\left(\frac{1}{2} + \frac{13\Lambda}{60}\right) - \Pi\left(1 + \frac{9\Lambda}{20}\right)\right]^2}{\left(\frac{B}{2} - \Pi\right)^2} \tag{23a}$$

$$F_2 = \frac{3\Gamma}{10}\left(1 + \frac{9\Lambda}{20}\right) + \frac{\left[B\left(\frac{1}{2} + \frac{13\Lambda}{60}\right) - \Pi\left(1 + \frac{9\Lambda}{20}\right)\right]\left(\frac{2B}{15} - \frac{3\Pi}{10}\right)\Gamma}{\left(\frac{B}{2} - \Pi\right)^2} \tag{23b}$$

$$F_3 = \frac{9\Gamma^2}{100} + \frac{\left(\frac{2B}{15} - \frac{3\Pi}{10}\right)^2 \Gamma^2}{\left(\frac{B}{2} - \Pi\right)^2} \tag{23c}$$

$$B \equiv \frac{\rho\delta\bar{R}\omega^2}{\tau}\ ,\ \Pi \equiv \frac{v_1^2}{U_\infty^2} \tag{23d}$$

$$\phi_o = \left(\frac{\phi_1 - \frac{\Gamma}{2}}{1 + \frac{\Lambda}{2}}\right) \tag{24}$$

$$\frac{\dot{m}_o}{\rho U(\phi_1 - \bar{\phi})} = 7.17\,\Lambda^{-0.8} + 0.00673\Lambda \tag{25}$$

$$\mu_1(T, \phi) = \nu_m \rho \left[\frac{T_f - T_s}{T - T_s}\right]\ ,\ T_s < T < T_f \tag{26}$$

$$T_f = \frac{1}{2}(T_g + T_1) \tag{27}$$

$$f_o = 0 \tag{28}$$

$$h_o = 0 \tag{29}$$

$$F = \sqrt{f^2 + h^2}\ , \tag{30}$$

$$g = \rho F \bar{\phi} \tag{31}$$

$$T_1 = T_o + \frac{q_s}{k}\left(\delta - \frac{\delta_1}{2}\right) - \frac{q_k\,\delta_1}{2k} \tag{32}$$

$$T_1 = T_{so} + \frac{\delta_1}{2k}(q_s - q_k) \tag{33}$$

$$\frac{\phi_1 - \phi_o}{\phi_1 - \phi_o} = \left(\frac{\delta_1}{\delta}\right)^2 \tag{34}$$

$$\frac{df}{ds} = U \cos \psi - \xi f \tag{35}$$

$$f = \frac{\tau \delta^2}{6 \mu_1} \tag{35a}$$

$$\frac{dh}{ds} = U \sin \psi - \xi h \tag{36}$$

$$h = \frac{\beta \delta^2}{12 \mu_1} - \frac{\tau_o \delta^2}{6 \mu_1} \tag{36a}$$

$$\frac{dg}{ds} = \dot{m}_o - \xi \phi_1 \rho F \tag{37}$$

$$f(s,k,i) = f(s-1,i) + \frac{\Delta S}{2} \left[f_s (s-1,i-1) + f_s(s-1,i) \right] \tag{38}$$

$$h(s,k,i) = h(s-1,i) + \frac{\Delta S}{2} \left[h_s (s-1,i-1) + h_s(s-1,i) \right] \tag{39}$$

$$g(s,k,i) = g(s-1,i) + \frac{\Delta S}{} \left[g_s (s-1,i-1) + g_s(s-1,i) \right]$$

$$g(s,k,i) = g(s-1,i) + \frac{\Delta S}{2} \left[g_s (s-1,i-1) + g_s(s-1,i) \right] \tag{40}$$

$$\frac{d\delta}{ds} = - \frac{\delta (f^2 + h^2) \frac{dW}{ds}}{W \left(2f^2 + 3h^2 + hf \frac{\tau_o}{\tau} \right)} \tag{41a}$$

$$\tau_o = C_f \frac{\rho_a v_1^2}{2} \tag{41b}$$

$$v_1 = \frac{-1 + \sqrt{1 + \frac{\rho \beta C_f \delta^2}{6 \mu_1}}}{\left(\frac{\rho C_f \delta}{2 \mu_1} \right)} \tag{41c}$$

$$\beta = \rho \bar{R} \omega^2 \tag{41d}$$

$$\Delta \delta_{corr} = [\Delta \delta]_{w = const} + \frac{d\delta}{ds} \cdot \Delta S \tag{42}$$

$$\Lambda = \frac{\delta U}{D_o} \text{ and } \Gamma = \frac{\delta \dot{m}_o}{\rho D_1} \tag{43}$$

$$\frac{C_D \rho_a U_\infty^2}{2} \lambda \cos^2 \psi + \frac{\rho F^2}{\lambda} \left(\frac{\lambda}{\delta} - 1 \right) - \zeta = 0 \tag{44}$$

$$V_e = \frac{F}{\lambda} \tag{45}$$

APPENDIX C

LIST OF SYMBOLS

Notation

A_{sy}	=	surface area of nodal mass
C_D	=	aerodynamic drag coefficient
C_F	=	coefficient of friction
D	=	oxygen diffusivity in metal
D_{on}	=	binary oxygen-nitrogen diffusion coefficient
F	=	melt flow scalar
F_r	=	radiation configuration factor
f	=	chordwise component of melt flow
g	=	oxygen convective flow in melt
h	=	radial component of melt flow
h_c	=	convective heat transfer coefficient
H	=	enthalpy of metal
$H_{o,o}$	=	heat of reaction per unit mass of oxygen
H_{sl}	=	latent heat of fusion
$\hat{i},\hat{j}$	=	unit vectors in chordwise and radial directions
$\hat{in}$	=	unit vector normal to surface
k	=	thermal conductivity
K	=	boundary layer shape factor
K_{xm}	=	mass transfer coefficient
ℓ^+_x, ℓ^-_x	=	nodal x-spacing
ℓ^+_z, ℓ^-_z	=	nodal z-spacing
M	=	mass of oxygen bonded on surface
$\dot{m}_o$	=	oxygen mass flux
n	=	direction normal to surface
$\bar{q}_s$, q_s	=	surface heat flux vector, scalar
$\bar{q}_k$, q_k	=	internal conduction vector, scalar
R	=	leading edge aspect ratio
$\hat{R}$	=	radius to mid-span of blade
S,J,I	=	streamline position, location index, and time index
s	=	distance along streamline
t	=	time
T	=	temperature in melted metal
T_g	=	gas temperature

LIST OF SYMBOLS (CONTINUED)

Notation

T_m	=	melting temperature
T_n	=	node temperature
T_x^+, T_x^-	=	temperatures of x-adjacent nodes
T_z^+, T_z^-	=	temperature of z-adjacent nodes
U	=	melting velocity of surface
U_x, U_z	=	x and z components of melting velocity
U_∞	=	free-stream air velocity
u, v	=	chordwise and radial velocity components (melt)
$\vec{V}$, V	=	liquid metal velocity vector, scalar
V_e	=	spreading velocity of liquid metal
W	=	width of streamline
X,Y,Z	=	chordwise, normal, radial coordinate system
X_e,Z_e	=	end of liquid metal region
X_t	=	laminar-turbulent transition point
α	=	fraction of nodal surface covered by melt
β	=	centrifugal body force per volume
γ	=	leading edge yaw angle
Γ	=	mass transport ratio
δ	=	liquid metal film thickness
δ_o	=	thickness of liquid at leading edge
δ_i	=	thickness of two-phase region
Δ	=	local thickness of airfoil
Δ_o	=	leading edge thickness
ζ	=	component of surface tension parallel to surface
θ	=	boundary layer momentum thickness
Θ	=	Fourier modulus
λ	=	thickness of liquid metal leading edge
Λ	=	mass transfer Peclet number
κ	=	thermal diffusivity of solid
μ	=	dynamic viscosity of liquid metal
ν	=	kinematic viscosity of liquid metal
ν_a	=	kinematic viscosity of air
ν_m	=	kinematic viscosity at liquidus temperature

LIST OF SYMBOLS (Concluded)

Notation

ξ	=	fraction of melt flow loss from surface per unit length
ρ	=	metal density
ρ_a	=	air density
σ	=	Stefan-Boltzmann constant
τ	=	aerodynamic shear stress in chordwise direction
τ_o	=	aerodynamic shear stress in radial direction
ϕ	=	local oxygen mass-fraction in liquid metal
$\bar{\phi}$	=	bulk (mean) oxygen mass-fraction in liquid metal
$x_{o,o}$	=	oxygen mol-fraction in air at surface
$x_{o,\infty}$	=	oxygen mol-fraction in air free-stream
ψ	=	streamline angle relative to chord
ω	=	rotational speed of blade
N_{u_θ}	=	Nusselt number for heat transfer
P_r	=	Prandtl number
Re_θ	=	Reynolds number based on momentum thickness
Sc	=	Schmidt number
St	=	Stanton number for mass transport

Subscripts

$_i$	=	interface of liquid and two-phase regions
$_s$	=	solid
$_l$	=	liquid
$_o$	=	liquid-solid interface
$_1$	=	liquid metal-air interface

APPENDIX D

REFERENCES

1. "Final Report of Titanium Combustion Research Program," 31 December 1978, Contract F33615-76-C-5041, Pratt & Whitney Aircraft Group, GPD (FR-10748).

☆U.S.Government Printing Office: 1979 — 657-002/05